INVESTIGATION OF MICROSTRUCTURE AND MECHANICAL BEHAVIOR OF NOVEL POWDER-EXTRUDED AL-CE-MG ALLOYS

A Dissertation Presented for the

Doctor of Philosophy

Degree

The University of Tennessee, Knoxville

Mairym Vázquez

August 2023

DEDICATION

This work is dedicated to Cárolyn Pantoja and Peiyong Chen, for their love, support and understanding.

M.V.

ACKNOWLEDGEMENTS

Thanks to my graduation committee Members: Dr. Hahn Choo, Dr. David J. Keffer, Dr. Eric Lass, and Dr. O. Marcelo Suárez from the University of Puerto Rico Mayagüez.

My laboratory colleagues and friends Max Neveau, Michael Thompson, Emma Counce, Elizabeth Heon, Dr. John Bohling, Dr. Peiyong Chen, and Dr. Hunter Henderson of Lawrence Livermore National Laboratory (LLNL) and everyone, that in one way or another, helped and worked on this project.

Special thanks to Dr. Orlando Ríos for the conceptualization of this research. Also, to David Weiss of Eck Industries, Inc, for providing material and insight for this project. I would like to acknowledge the contribution of Dr. Emily Moore, from LLNL, to the thermodynamic modeling for this research. Also, from LLNL, Joshua Hammons is acknowledged for his work on SAXS and particle distribution analysis. This research was supported by the Critical Materials Institute (CMI), an Energy Innovation Hub funded by the U.S. Department of Energy (DOE).

ABSTRACT

Pursuing advanced structural materials with enhanced performance, reduced weight, and lower costs is a constant endeavor in the aerospace and automotive industries. Conventional structural alloys, such as cast irons, carbon steels, and titanium alloys, have strength, weight, and cost limitations. Aluminum-based alloys, known for their lightweight and high strength, have gained popularity in these industries. This dissertation focuses on investigating microstructure and mechanical behavior of novel powder-extruded Al-Ce-Mg alloys as potential candidates for high-performance structural materials.

This research explores using powder extrusion, a well-established forging methodology in the steel industry, to produce Al-Ce-Mg alloys with improved properties and aims to understand the influence of process conditions on microstructure development, evaluate the different phases present in the alloy under various heat treatment conditions, and analyze their influence on mechanical behavior.

The proposed Al-Ce-Mg alloy offers several advantages, including thermodynamic stability at elevated temperatures and refined microstructure through rapid solidification. By studying the alloys' microstructure and mechanical properties, this research contributes to the development of advanced manufacturing methods with improved material properties.

The study showed that the powder-extruded Al-8Ce-10Mg wt. % alloy exhibits high ultimate tensile strength of 687 MPa, compared to conventional high-magnesium Al-5083 alloys series with the UTS of 270-385 MPa. After heat treatments, the alloy gains back elongation from 1 % to 9 % while retaining 79 % of the UTS, a high-strength material compared to conventional aluminum alloys. Insights gained from this research can potentially lead to the production of high-strength aluminum-based alloys that outperform conventional Al-based alloys, some irons, and titanium-based alloys, potentially impacting various manufacturing applications.

TABLE OF CONTENTS

LIST OF TABLES

LIST OF FIGURES

CHAPTER 1 INTRODUCTION

1.1 Motivation

Seeking novel advanced structural materials is always a critical issue in aerospace and automotive industry. One of the goals is to design and develop structural materials with improved performance, lower weight, and lower costs. Conventional structural alloys including cast irons, carbon steels, magnesium (Mg) alloys, titanium (Ti) alloys, aluminum (Al) alloys, and conventional carbon steels etc. are strong but not light [**1**]. Magnesium alloys are widely used in automobiles applications due to their light weight, but the strength (in the range of 180 to 440 MPa) may not be satisfactory [**2**, **3**]. Titanium alloys have high strength and toughness, but they are expensive [**4**]. Aluminum-based alloys have garnered widespread popularity as preferred materials in the automotive and aerospace industries. This is due to the allure of aluminum as an engineering material, being lightweight yet capable of achieving high strength levels through effective heat treatment techniques. There are several designations for commercially available Al-based alloys. The 5000 series is the designation for the Al alloyed mostly with Mg, which in general possesses a good corrosion protection. The addition of Mg increases the strength with a small decrease in ductility, due to high solubility of Mg in Al that can create a supersaturated solid solution [**5**].

Cerium (Ce) is the most abundant rare earth (RE) comprising 37 % of all RE elements present in Earth's crust. Due to the abundance of Ce and its small-scale applications, effort has been made to find application of Ce in larger scale. Alloying Ce with Al had been one of the major research developments for finding structural materials with high cerium content [**6**, **7**]. Aluminum-cerium alloys can be used in high-temperature applications due to a thermodynamically stable $Al_{11}Ce_3$ phase that forms during solidification and the slow diffusion kinetics of Ce in this phase [**8**, **9**]. Also, the very low solubility of Ce in Al (about 10^{-4} wt. % at 600 °C) gives the material a high thermal stability compared to commercially available precipitation-hardened Al alloys [**9**, **10**]. Therefore, Al-Ce alloys for high-temperature applications could represent an appealing alternative to commercially available

Al-based alloys, by facilitating the design of aerospace structures and transportation parts such as higher-efficiency internal combustion engines.

In recent research on Al structural materials there is a trend on Additive Manufacturing (AM) as a fabrication methodology for structural materials including, but not limited to, Laser Powder Bed Fusion (LPBF), wire arc AM, and sheet lamination [**11**-**19**]. These methods can produce nanostructured materials due to non-equilibrium solidification, however, they have their limitations such as component size, production speed, surface defects (such as cracking and porosity), shape accuracy, evaporation of elements and process optimization [**20**, **21**].

Al-Ce binary alloys are reported to be highly castable, corrosion resistant, and to possess high thermal stability [**22**]. Studies have demonstrated that the entire family of Al-Ce alloys, encompassing both ternary and quaternary compositions, exhibits remarkable retention of yield strength, even at elevated temperatures, when compared to conventional Al alloys. This characteristic makes these alloys highly suitable for high-temperature applications [**10**, **19**]. Al-Ce-Mg alloys that consist of 6-16 wt. % of Ce and Mg have demonstrated impressive thermal stability at high-temperature applications. Also, heat treatment does not affect the mechanical properties of these alloys [**9**]. As a result, the novel Al-Ce-Mg alloys hold significant promises for addressing the limitations associated with conventional Al alloys [**8**].

On the other hand, powder extrusion is a well-established forging methodology for the steel industry. Efforts have been made to study the application of powder extrusion for some new Al-based alloys, and to tailor the heat treatment conditions [**23**]. In powder extrusion, powders are consolidated by applying high pressure and extruded into rod or tube shapes. The consolidation or compaction can be performed at room temperature or at elevated temperatures (i.e., hot extrusion). Generally, raising the compressing pressure and the pressing time produce higher degrees of consolidation [**24**]. If done at enough compression ratio, the compression and shear forces that build during extrusion suffice to consolidate the powders, without sintering after extrusion. Extrusion ratio to consolidate powders without sintering is not define by a specific number (because it is also dependent of material, working temperature, and size of powder particles), and can be establish experimentally.

After the deformation caused by the cold extrusion process, heat treatment is an important step to release internal stress that return the material's ductility without losing much strength [**25**].

1.2 Objectives

The major objective of this research is to study the microstructure and mechanical properties of ternary Al-8Ce-10Mg wt. % alloy prepared by powder extrusion. The specific goals are to:

- achieve consolidation of Al-8Ce-10Mg alloyed powder with the method of powder extrusion at 300 °C working temperature, without the need of sintering,
- perform a series of post-consolidation heat treatments on Al-8Ce-10Mg samples at different conditions: 350 °C, 400 °C, 425 °C and 432 °C for 4.5 hrs, to find the optimal heat treatment condition for this material,
- study the effect of various heat treatment conditions on the microstructure of the Al-8Ce-10Mg alloy to determine the different phases present,
- investigate the effect of the heat treatment on the mechanical properties of the Al-8Ce-10Mg alloy prepared by the powder extrusion.

Some of the technical merits of the current research on the powder extruded Al-Ce-Mg alloy as a potential structural alloy include the followings:

- production of refined, homogeneous nano-structured Al-Ce-Mg alloy due to the rapid solidification during the atomization of alloy powders,
- establishing an optimum powder extrusion condition with a high-extrusion ratio that produces a near-net-shape, fully-dense component without the need of post-consolidation sintering,
- production of components with low porosity and minimal defects, in a fast production time with forging equipment readily available in the metallurgy

industry. This is a more viable and effective process than conventional powder extrusion requiring sintering.

A major goal, of the present research is to render insights into the potential use of powder extrusion processing to produce high-strength aluminum-cerium-magnesium alloys with improved mechanical properties, which could have practical applications in various industries, including the substitution of commonly used Al-based alloys, Fe, and Ti-based alloys.

CHAPTER 2 LITERATURE REVIEW

2.1 Aluminum Alloys

Aluminum alloys are lightweight and have a high strength-to-weight ratio, making them an attractive material for many industries, including aerospace, automotive, and construction. Innovations in aluminum alloys can lead to even lighter and stronger materials with improved performance properties, such as increased corrosion resistance, enhanced thermal and electrical conductivity, and higher wear resistance. These advances can expand the range of applications for aluminum alloys in various industries. The design of new aluminum alloys can also lead to cost reduction. Aluminum alloys are already a relatively sustainable material, as they are highly recyclable when impurities are not high. An example of non-recyclable Al alloys, is when it contains high amounts of Fe or Si; these systems create phases detrimental to the material's mechanical performance [**26**].

Numerous commercially accessible aluminum alloys exhibit varying tensile strength and elongation values, influenced by factors like composition, processing methodology, and heat treatment conditions. Some examples of ambient temperature UTS and tensile elongation values for commonly used high-strength aluminum alloys are: 6061-T6 (UTS 290 MPa, elongation 8 %), 7075-T6 (UTS 570 MPa, elongation 15 %), 2024-T3 (UTS 501 MPa, elongation 10.4 %), 5083-H116 (UTS 323 MPa, elongation 16 %) [**27**-**30**]. The UTS of commercially available Al-based alloys ranges from 100 to 700 MPa, and even when the term "high-strength" alloy is subjective, in literature there is a general agreement of defining it as an Al alloy with a UTS higher than 250 MPa.

There are several Al-based alloys commonly used for high temperature applications: 4032-T6 (UTS 400 - 490 MPa, elongation 5 -10 %) used for pistons , 2618-T6 (UTS 410 - 470 MPa, elongation 5 - 8 %) used for turbines, and 356-T6 (UTS 230 - 280 MPa, elongation 3 - 7 %) used for engine blocks [**9**]. On a later section, we will compare these alloys with casted Al-8Ce-10Mg wt. % before and after HIP.

2.2 Cerium

The United States of America has included rare earth minerals, such as Ce, on the critical mineral lists to ensure an adequate supply for future private and military requirements. This recognition promises well for the sustainability and viability of rare earth alloys [**31**]. Nowadays, the supply of Ce is limited and finding a mass application for cerium could reduce the reliance on other countries for the material, improving the for industries that rely on Ce-based products.

Cerium is an RE element that has many important uses in various industries. However, it is also a relatively expensive material, which limits its widespread use. If a bulk application for cerium is found, it could increase the demand for the material, which could lead to better the economies in production of the RE industry, reducing the cost of cerium-based products. Currently, Ce is categorized as a byproduct of the rare earth industry, where 70 % yield Ce and La when only Nd, Pr, Dy, and Sm are used and yield about 20 % of the mining process [**7**, **32**]. The majority of Ce and La goes to land fields with further costs. Profiting from the Ce obtained in the rare earth mining industry, will lower the cost of Nd, Pr Dy and Sm. This could lead to developing new products, technologies, and industries. Cerium has important environmental applications, such as catalytic converters that reduce harmful cars emissions. Finding a bulk application for cerium could help reduce environmental impact by aiding these applications.

2.3 Effects of Ce on Al Alloys

Al-Ce binary phase diagram has been reviewed, and the consensus is that the eutectic point is at approximately 10 wt. % Ce (**Figure 1**) [**8**, **33-35**]. Adding Ce to aluminum alloys can significantly impact their mechanical properties and improve castability by increasing melt fluidity [**22**]. Cerium is used commercially to prevent corrosion (typically at a concentration of around 1 % Ce) [**9**]. Current research has shown that adding Ce to Al up to 2.4 wt. % prevents corrosion growth as a function of Ce amount. By impeding grain boundary motion, the inclusion of Ce in Al-Cu alloys serves as a diffusion barrier.

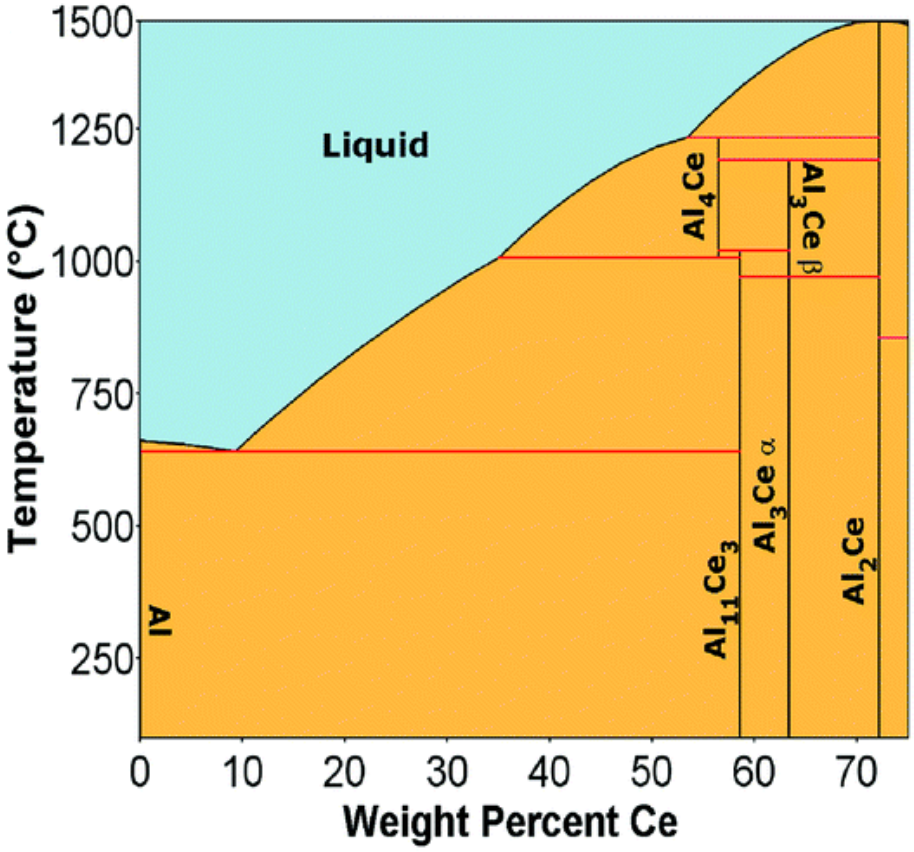

Figure 1. Partial Al-Ce phase diagram in wt. % [8].

Ce can also act as a grain refiner in Al alloys, which means that it can improve the uniformity and distribution of the grains within the material, resulting on a refined microstructure on the aluminum alloy, which can lead to enhanced mechanical properties such as improved tensile strength, yield strength, and elongation. In an aforementioned waste Al products containing high Fe, it has been reported that the addition of Ce into Al alloys counteracts the detrimental impact of Fe, leading to the refinement of the grains and ultimately resulting in enhanced strength [**36**].

Al-Ce alloys have recently come to the attention of researchers because it has been found that even low of Ce can form intermetallic compounds with Al, such as $Al_{11}Ce_3$, which can improve the thermal stability, mechanical properties, high-temperature performance, and strength [**8**] (**Figure 2**). This has also been reported when Ce is added to aluminum in compositions from 6 wt. % to the eutectic point of around 10 wt. % [**9**]. Rapid cooling manufacturing process, like laser manufacturing creates refined $Al_{11}Ce_3$ phases that enhance the microstructure compared with casted Al-Ce [**19**].

Extruded Al-Ce alloy samples (extrusion ratio of 3:1) registered a 400 MPa tensile strength with a yield strength of 340 MPa [**10**]. Weiss et. al. stated that even though close to the eutectic Al-Ce alloys exhibited favorable casting characteristics, their mechanical properties at room temperature were insufficient for some commercial applications and they did not demonstrate an improvement on tensile properties after exposure to the T6 HT cycle (538 °C for 1.5 hrs, quenching, then 154 °C for 3 hrs) [**37**].

2.4 Al-Ce-Mg Alloys

In binary Al-Ce alloys, the $Al_{11}Ce_3$ intermetallic does not provide significant strengthening at room temperature. To attain desirable strength levels under such conditions, incorporating other alloying elements such as Mg, Zn, Cu, Si, or other compatible options is necessary to fortify the aluminum matrix. Ternary Al-Ce-Mg alloys are a type of advanced aluminum alloy that is gaining attention for their unique properties and potential applications where both Ce and Mg strengthen Al alloys.

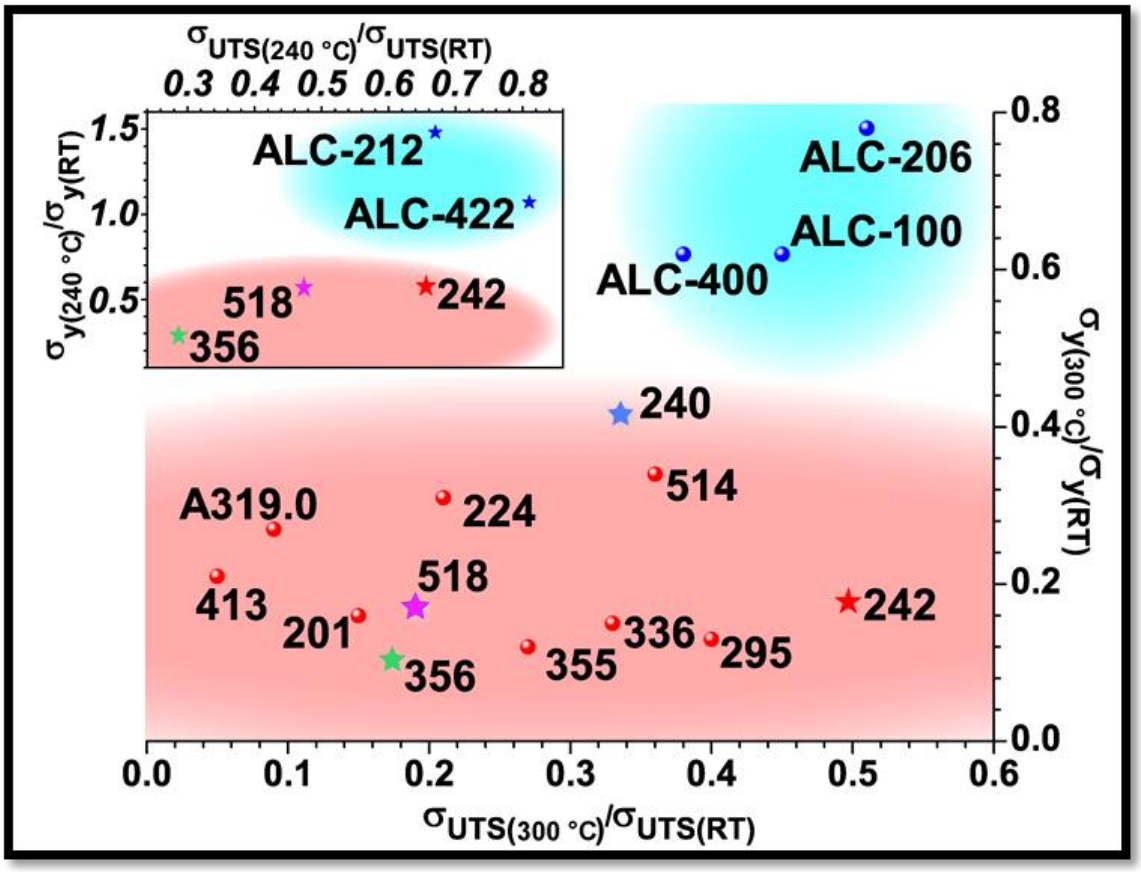

Figure 2. Yield strength ratio (300 °C / RT) vs. UTS ratio (300 °C / RT). Inset shows Al-Ce based alloys yield strength ratio (240 °C / RT) vs. UTS ratio (240 °C / RT) [8].

Magnesium acts as a solid solution-strengthening element when added to Al-Ce and improves the material's processing characteristics while reducing its density [**9**, **38**]. This strengthening mechanism is attributed to the size and elastic modulus differences between the two elements, increasing the initial yield stress [**39**].

Al-Ce-Mg alloys present refined microstructure when casted, and because of slower cooling rates the $Al_{140}Mg_{89}$ β phase has been found (**Figure 3**). Al-Ce-Mg alloys presents a nanostructured network (as an example in **Figure 4**) when parts are produced by LPBF-AM, as a result high strength, improved hardness, and less solidification cracking are attained [**17**, **18**]. This nanostructure develops from the rapid solidification of processes like LPBF-AM and powder atomization, which can enhance mechanical properties compared to casting. After heat treatment (300 °C for 218 hours), LPBF-AM Al-8Ce-10Mg samples reported a UTS of ~431 MPa, a significant improvement compared with as-casted material [**18**]. In the Al-Ce binary case, rapid cooling methodologies reduce the spacing of lamellae $Al_{11}Ce_3$ resulting in a nanostructured material.

Up to a concentration of 10 wt. % Mg, increasing the amount of magnesium in ternary Al-Ce-Mg alloys led to a rise in yield strength without any significant decline in castability [**37**]. Also, Al-Ce-Mg presents great mechanical properties at high temperatures [**7**, **40**] (**Figure 5**). Initial extrusion experiments have been conducted using an Al-10Mg-8Ce wt. % alloy. The material was manufactured at billet temperatures of 300 °C (ratios 5.75:1 and 52:1). Results show that with an increase in the extrusion ratio, the tensile strength remained steady. In contrast, the elongation increased and the yield strength decreased [**9**].

Metastable τ phase ($Al_{13}CeMg_6$) has been reported on Al-8Ce-10Mg wt. % alloy made under non-equilibrium solidification conditions [**41**]. It is known that this compound is not stable at low temperature, and decompose between 320 °C and 400 °C [**42**]. The phase is considered a metastable phase and is susceptible to thermal coarsening [**41**, **43**]. Interestingly, Lane et al. [**44**] did not report the presence of τ phase (powder extrusion, ratio 52:1, preheated 420 °C); Mg was only found in the Al-rich solid solution matrix.

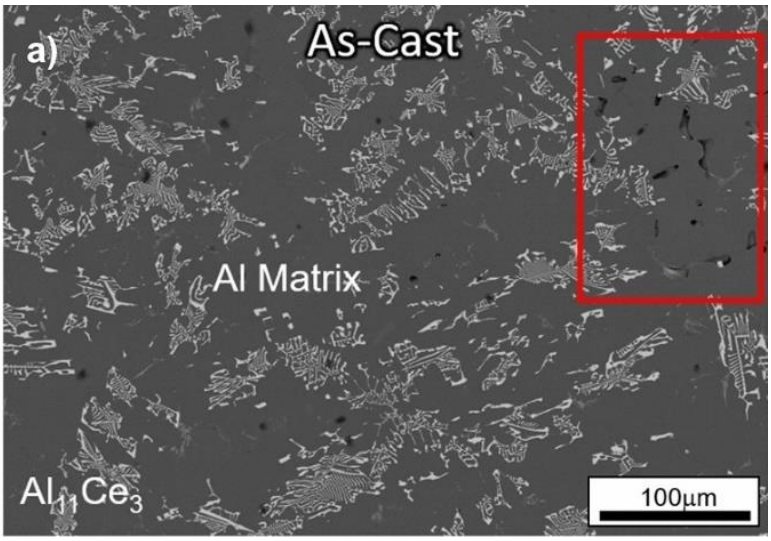

Figure 3. SEM micrograph cast sample of Al-8Ce-10 Mg showing Al-La/Ce intermetallics in an Al matrix [7].

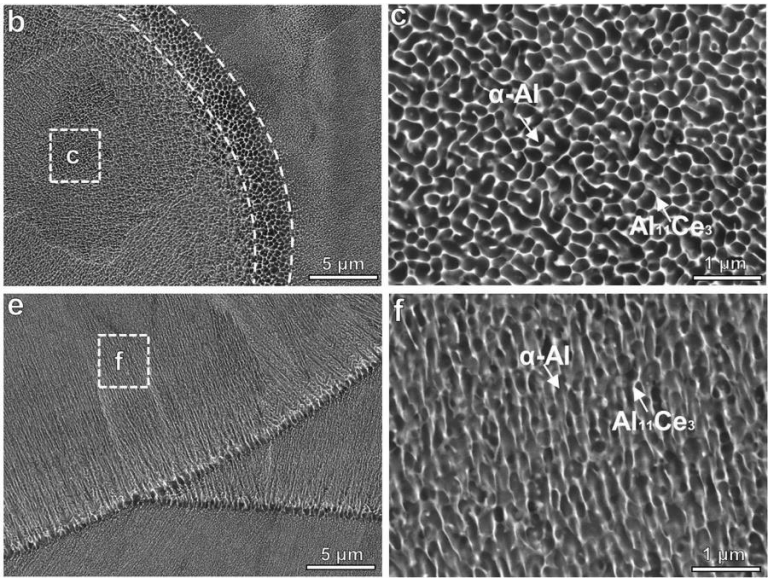

Figure 4. Backscattered electron image analysis of Al-9.5Ce-0.6Mg wt. % alloy showed nano-network of interconnected aluminum cells surrounded by $Al_{11}Ce_3$ intermetallics, the nanostructure is produce by rapid solidification [17].

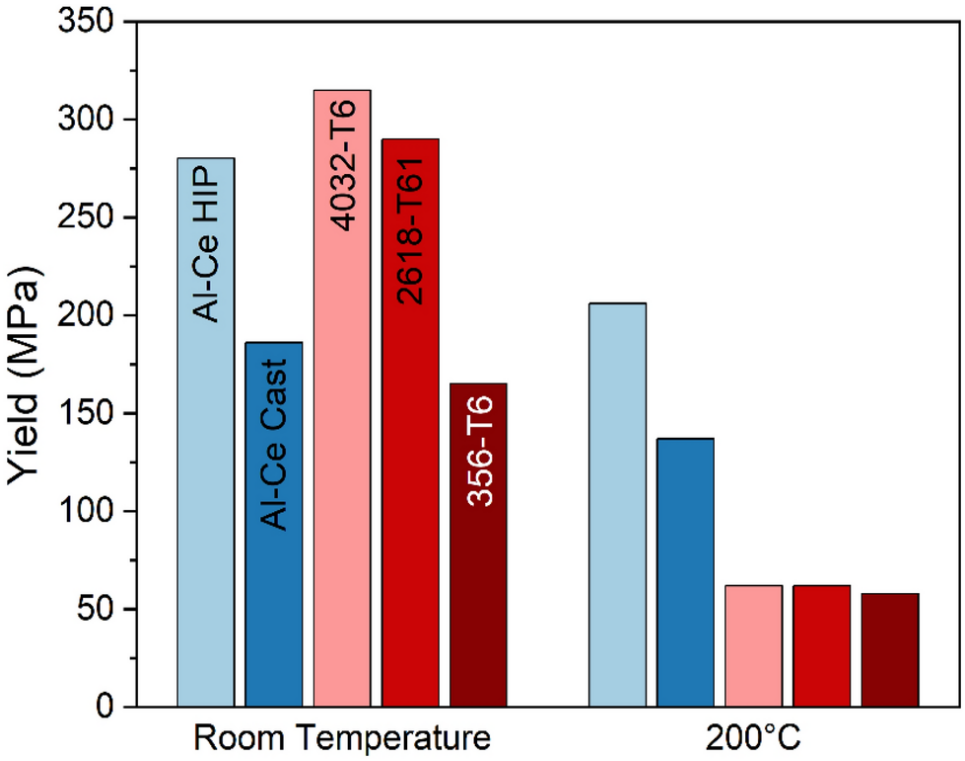

Figure 5. Tensile test at ambient temperature and at 200 °C before and after HIP (520 °C for 2 hrs and isostatic pressure of 100 MPa) of casted Al-8Ce-10Mg wt. % compared with the commonly used Al-based alloys [7].

The remarkable strength retention of Al-Ce-Mg following thermal treatment can be attributed to the immobility of Ce throughout the Al matrix, which effectively prevents coarsening [**18**, **45**]. Additionally, it has been confirmed that Al-Ce-Mg alloy exhibits improved mechanical properties compared to Al-Ce, thanks to the inclusion of Mg. This element effectively increases the threshold for dislocation saturation within the Al-Ce intermetallic phase, enabling it to withstand a greater load before transferring it to the Al-FCC matrix (**Figure 6**) [**8**].

A summary and comparison of tensile properties of binary Al-Ce alloys and Al-8Ce-10Mg wt. % via different production methodologies is shown in **Table 1**.

2.5 Fabrication Methods and Their Effects on Microstructure and Properties

2.5.1 Alloy Powder Production Via Atomization

Powder atomization is a process used to produce fine metal powders from a melted alloy. In this process, a stream of molten metal is forced through a small orifice or nozzle, and then rapidly cooled by a gas or liquid to form small droplets. These droplets solidify into fine metal particles that can be used in various applications.

The powder atomization process can be accomplished using several methods, including gas atomization, water atomization, and plasma atomization. Gas atomization is the most used method, in which an inert gas, such as argon, is used to atomize the molten metal.

Powder atomization can produce powders with a wide range of particle sizes, from a few microns to several millimeters. The size of the resulting powder particles can be selected by sifting the powder with the desired size range parameters. The fine particle size and uniform distribution of the powders produced by powder atomization can result in improved mechanical properties, such as increased strength and elongation.

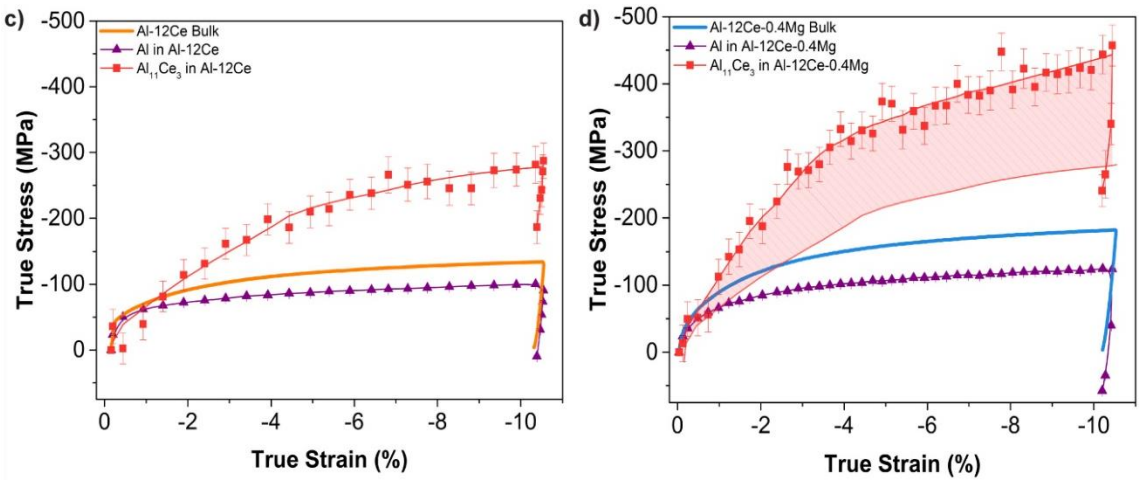

Figure 6. Stress vs Strain curves (compression test). Example of load sharing of phases in Al-12Ce and Al-12Ce-0.4Mg. Adding Mg increases the amount of the load that the $Al_{11}Ce_3$ intermetallic phase can support before redistribution the load to the Al matrix [8].

Table 1. Tensile properties of binary Al-Ce and Al-8Ce-10Mg wt. %

Composition	Processing	Heat Treatment Condition	Tensile test temp	Elong. (%)	Yield strength (MPa)	Tensile strength (MPa)	Ref.
Al-16Ce	cast	T6 (538 °C, 90 min quenched 154 °C, 3 hrs)	RT	3.5	78	118	[**37**]
Al-12Ce	cast	T6	RT	26.5	48	132	[**37**]
Al-10Ce	cast	T6	RT	24	46	129	[**37**]
Al-9Ce	cast		RT	17 ± 1	75 ± 2	135 ± 3	[**46**]
Al-8Ce	cast	T6	RT	26.6	59	122	[**37**]
Al-6Ce	cast	T6	RT	33.5	33	103	[**37**]
Al-16Ce	cast		RT	2.5	68	144	[**9**]
Al-12Ce	cast		RT	13.5	58	163	[**9**]
Al-10Ce	cast		RT	8	50	152	[**9**]
Al-8Ce	cast		RT	19	40	148	[**9**]
Al-6Ce	cast		RT	25	30	103	[**9**]
Al-10Mg-8Ce	cast	260 °C, 336 hrs	RT	1	137	159	[**9**]
Al-10Mg-8Ce	cast	260 °C, 336 hrs	260 °C	5	97	336	[**9**]
Al-10Mg-8Ce	cast	260 °C, 0.5 hrs	260 °C	4	131	137	[**9**]
Al-10Mg-8Ce	cast	315 °C, 0.5 hrs	315 °C	20	55	97	[**9**]
Al-10Mg-8Ce	cast	315 °C, 216 hrs	315 °C	13.8	56	94	[**9**]
Al-10Mg-8Ce	cast	315 °C, 216 hrs	RT	1	159	172	[**9**]
Al-10Mg-8Ce	cast	400 °C,120 hrs	RT	1.5	191	218	[**9**]
Al-10Mg-8Ce	cast	500 °C, 500 hrs	RT	3	185	252	[**9**]
Al-10Mg-8Ce	cast		RT	1	186	228	[**9**]
Al-10Mg-8Ce	cast	T4	RT	2	200	248	[**9**]
Al-10Mg-8Ce	cast	HIP	RT	2	207	262	[**9**]
Al-10Mg-8Ce	extrusion 5:1		RT	5.8	342	375	[**9**]
Al-10Mg-8Ce	extrusion 52:1		RT	12	274	364	[**9**]
Al-10Mg-8Ce	permanent mold		RT	1	186	228	[**9**]
Al-10Mg-8Ce	extrusion 52:1		RT	16.67	149	304	[**44**]
Al-10Mg-8Ce	LPBF-AM		RT	2 - 3		429 - 491	[**18**]
Al-10Mg-8Ce	LPBF-AM	300 °C, 218 hrs	RT			393 - 461	[**18**]
Al-10Ce	LPBF-AM		RT	10.8	222.1	319.3	[**16**]

When atomizing a melt, alloys almost instantly solidify into powder particles. This rapid solidification can create a nanostructured powder because solidification occurred at non-thermal equilibrium. The very fine microstructure (very small grain boundaries, small intermetallic precipitates, etc.) will generate a material with improved mechanical performance, such as strength, yield strength, and hardness. This phenomenon is described by the empirical expression known as the Hall-Petch relationship: as the average grain size diminishes within a material, its strength increases due to the obstructive influence of grain boundaries on dislocation slip.

2.5.2 Consolidation Via Powder Extrusion

Powder extrusion is one of many advanced manufacturing processes in which a powder material is forced through a die to create a specific shape. Powder extrusion is an important manufacturing process in various industries, including pharmaceuticals, food, ceramics, and metalworking. Powder extrusion allows us to produce materials with a specific particle size and shape, which is crucial in many industries. The process can also improve the properties of materials. For instance, raising the compressing pressure and the pressing time produce higher degrees of consolidation [**24**], sometimes without secondary processing steps, such as sintering on the desired characteristics and application. Powder extrusion can improve manufacturing efficiency by enabling continuous production of materials with consistent quality.

Powder extrusion can be a cost-effective way to produce complex parts with high precision, as it often requires fewer materials and has less waste than other manufacturing processes.

2.5.3 Post Consolidation Heat Treatment

Heat treatment after powder extrusion is an essential step in producing high-quality metal components. Final grain size, yield strength, UTS, and elongation depends on heat treatment (annealing) temperature and time. As stated before, during the powder extrusion process, the metal undergoes significant plastic deformation, which can develop residual stresses in the material. Heat treatment can relieve these stresses and improve the

mechanical properties of the metal. It can also be used to control the microstructure of the metal. Heat treatment after powder extrusion is an important step in the production of high-quality metal components. Manufacturers can produce components with the desired properties and performance characteristics by carefully selecting the right heat treatment process.

Microstructure evolution can also be characterized quantitatively by analyzing the micrographs using various image analysis techniques (such as ImageJ), such as grain size and distribution, and phase identification [**47**]. These quantitative measurements can be used to model and predict the material's behavior and correlate the results with other technics, such as SAXS for quantifying grain size and distribution.

CHAPTER 3 EXPERIMENTAL PROCEDURE

3.1 Materials and Processing

3.1.1 Atomized Al-8Ce-10Mg Alloy Powder

A batch of molten Al-8Ce-10Mg (wt. %) was gas-atomized in an inert atmosphere, producing an alloyed Al-8Ce-10Mg wt. % powder (Eck Industries, Inc., Manitowoc, WI, USA). The powder was not sieved, and the range of particle distribution was tested. Inductively Coupled Plasma Optical Emission Spectrometry (ICP-OES) test was conducted to measure the elemental composition of the material at the ORNL Industrial Hygiene Analytical Laboratory, TN. There are two major reasons for conducting this test. First, the loss (by evaporation) of Mg in the alloying process needs to be quantified [**48**]. Second, the presence of 0.2 % Ti in Al-8Ce-10Mg wt. % atomized powder creates a brittle phase detrimental to the elongation of the material [**49**] (**Figure 7**). It was our objective to have a maximum Ti level of 0.04 %. The result of the material chemistry is in **Table 2** and comply with the elemental compositions that we intend to study.

3.1.2 Powder Extrusion

The as-received Al-8Ce-10Mg wt. % pre-alloyed powder (1300 g) was placed in an argon backfilled aluminum-6061 can (63.5 mm O.D.) as a sheath material. The cans were preheated in an induction furnace at 300 °C for 30 minutes. Extrusion was carried out under this working temperature to avoid significant strain hardening. At this condition, the energy required to deform the material is lower and protect the equipment from unnecessary high-strain conditions. The cans were fed to a horizontal direct extrusion machine. A ram applied pressure to the canned powder, pushing it through a 12.7 mm die and forming it into a solid bar. The extrusion ratio of 25:1 produced approximately 3.65 m length of run out in each extrusion. The ram speed was controlled at a constant 1460 cm/min. It is worth noting that no sintering treatment was performed after the extrusion expecting full consolidation of the powder particles without post-extrusion high-temperature fusion.

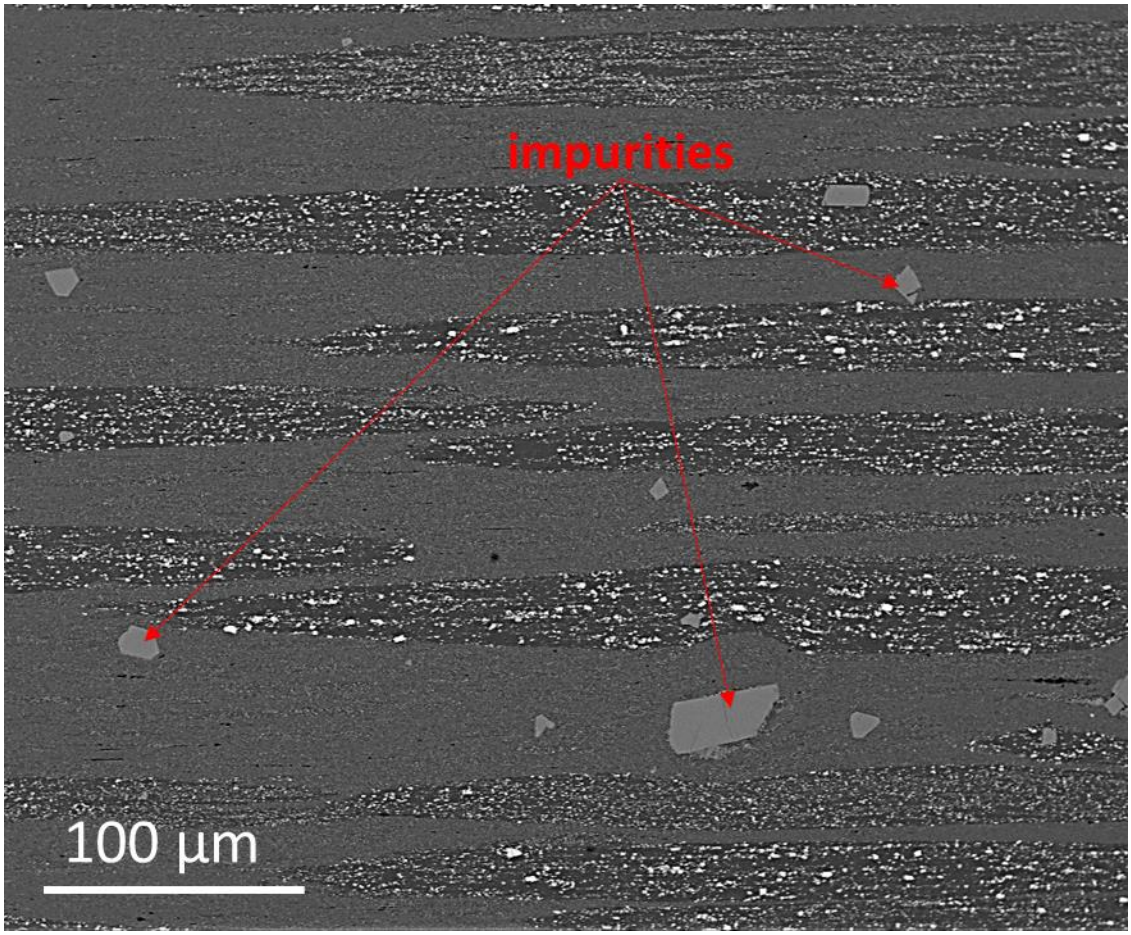

Figure 7. SEM image of powder extruded Al-8Ce-10Mg wt. % containing Ti impurities [49].

Table 2. Result of Inductively Coupled Plasma Optical Emission Spectrometry (ICP-OES) on Al-8Ce-10Mg atomized powder.

Element	wt. %
Aluminum	81.93
Cerium	7.64
Magnesium	9.93
Titanium	0.027
Copper	0.029
Iron	0.17
Manganese	0.12
Nickel	< 0.01
Zinc	0.068

3.2 Thermodynamic Modelling

To simulate the phase evolution at different temperatures, ThermoCal/ CALPHAD was used to calculate the ternary phase diagram for Al-8Ce-10Mg wt. %. The solidification path and the phases present in an equilibrium phase transformation were described. Also, calculated isothermal sections for the composition at 100 °C, 400 °C, and 500 °C were modelled. An empirical approach based on direct measurement rendered information for the thermodynamic modelling because the low diffusivity of Ce on Al often results in non-equilibrium phase compositions. Meaning that the model parameters were derived using an optimization method designed to accurately replicate the experimentally determined phase equilibria and thermodynamic properties with those calculated ones [**50**, **51**].

3.3 Microstructural Analysis

3.3.1 Microscopy

Micrographs provide important information about the size, shape, and arrangement of the various constituents of a material at the microscale. By examining a series of micrographs taken before and after heat treatment, one can observe how the intermetallic particles of the material change (in terms of morphology, size, and distribution) with heat treatment temperature, and in that way, gain insight into the mechanisms driving microstructural evolution.

For all microscopic imaging techniques, samples were polished to a finished surface of 0.5 µm using a diamond paste. Samples were not etched since, after several attempts, only the intermetallic was attacked by the etching and it did not reveal grain boundaries or any new features due to the very fine microstructure. For optical microscopy and SEM images, both transverse and longitudinal cross sections were prepared as defined in **Figure 8**, since the microstructure features are very different depending on if they are being examined parallel or perpendicular to extrusion direction.

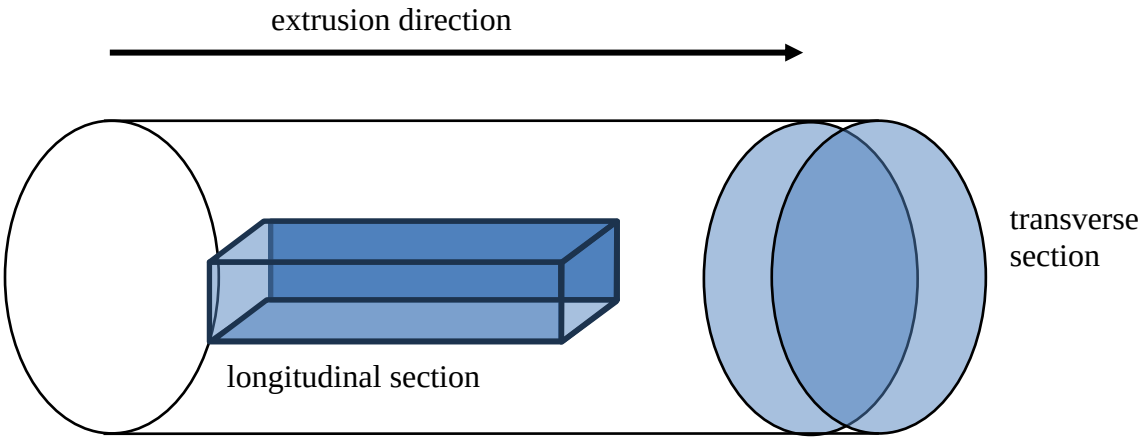

Figure 8. Schematic of an extruded sample.

To understand the microstructure changes after heat treatments, a series of SEM images were taken of before and after all heat treatment conditions on a Zeiss Evo at IAMM Microscopy Center UTK, to verify if coarsening of the intermetallic occur at any heat treatment condition. Analysis of SEM micrographs with Image J software were done to characterize microstructure evolution of particle size with heat treatment and to eventually be compared to the results obtained from SAXS/USAXS intermetallic particle size and distribution analysis.

3.3.2 X-Ray Diffraction (XRD)

XRD was conducted at IAMM at UTK on polished samples, cut parallel to the extrusion direction, from the extruded bars before and after heat treatment (**Figure 8**). We are interested in quantifying the amount of Mg (at. %) in the Al solid solution, since after heat treatment the Mg in the τ phase ($Al_{13}CeMg_6$) can dissolve into the Al phase. For this, we are using the $\{111\}_\alpha$ and $\{200\}_\alpha$ peaks shift to obtain the lattice parameter changes that can be correlated with the addition of Mg to the Al_α structure. The amount of Mg (at. %) in the Al phase was reported. Al $\{111\}_\alpha$ and $\{200\}_\alpha$ peaks diffract at 38.47° and 44.72° respectively for Cu K-α with wavelength of λ = 1.5418 Å [**52**]. XRD measurements were performed in an angle range of 2θ = 25 to 48° at intervals of 0.02°.

3.3.3 Ultra-Small Angle X-ray Scattering (USAXS)

USAXS methods are ideal for investigating the evolution of the microstructure in terms of intermetallic particle size and its distribution after thermal processing. The USAXS data was collected on Xeuss 3.0 Bonse-Hart using monochromatic 8 keV X-rays and a slit-length of 0.23 $Å^{-1}$ and beam size of 4 mm x 4 mm (~ 2 mm x 2 mm FWHM). Desmeared SAXS data was also collected from a Pilatus 3R detector and slit-smeared so that it could be merged with the USAXS data using the Irena package for Igor Pro [**53**].Notably, no anisotropic scattering was observed in these 2D images, which allows us to treat the scattering populations as statistically isotropic. The combined slit-smeared data was calibrated using a calibration factor obtained from the desmeared, 1D intensity from a glassy carbon standard [**54**]. With the thickness of each sample known (0.07 mm to 0.09 mm), the

slit-smeared data was placed on an absolute intensity scale [**55**]. The error associated with the thickness measurement is +/- 0.01 mm based on the caliper accuracy.

3.3.4 Density

Applying the Archimedes principle, the density of all samples was determined utilizing the Sartorius density determination kit (Sartorius YDK03, Germany). During the measurements, the kit was configured with distilled water, and close attention was paid to the continuous monitoring of the water's temperature.

3.4 Post Extrusion Heat Treatment Conditions

After the powder extrusion, heat treatments were conducted for 4.5 hours at different temperatures of 350, 400, 425, and 432 °C (**Table 3**). The samples were then rapidly quenched in water to retain microstructure.

3.5 Mechanical Properties Characterization

3.5.1 Microhardness

Micro-indentation test was performed using a KLA IMicro nanoindenter at UTK for all heat-treated samples. Vickers hardness were obtained from this experimentation. For each measurement, a mapping area was selected for the equipment to perform a series of hardness tests using a 5 x 5 matrix, for a total of 25 indentations. A maximum depth of 3000 nm and a maximum load of 800 mN were used, meaning that the indentation was completed when reaching either of the said parameters. The indentation strain rate was set to 0.2 s^{-1} and the target frequency to 110 Hz. Each measurement location in the matrix was 75 µm apart to avoid the plastic-deformation-affected zone of a nearby indentation. All tests were performed at room temperature.

Table 3. Post extrusion heat treatment conditions.

Sample designation	Heat Treatment	
	Temp (°C)	time(hrs.)
as-extruded	as extruded	
350 °C - 4.5 hrs	350	4.5
400 °C - 4.5 hrs	400	4.5
425 °C - 4.5 hrs	425	4.5
432 °C - 4.5 hrs	432	4.5

3.5.2 Ambient Temperature Tensile Testing

Tensile testing was conducted to evaluate the mechanical behavior of the extruded samples before and after different heat treatments. From the extruded bars, cylindrical samples were machined for tension test according to ASTM E8-E8M [**56**]. When preparing the specimens, caution was taken to dispose of the outside Al-6061 can, that served as a shielding material. Tensile tests were conducted in an Instron 5566 Universal Testing Machine (at UTK) at room temperature using an extensometer for sample elongation data. Note that controlled crosshead speed was used, at a rate of 0.008 mm/s, as recommended for alloys with regions of discontinuous yielding.

Fracture surface analysis was performed for the as-extruded and 432 °C - 4.5 hrs samples after the room-temperature tensile testing. The images allow for surface topography characterization to determine the failure mechanisms (e.g., brittle fracture, ductile fracture, etc.) by identifying crack initiation sites and crack grow behavior.

CHAPTER 4 RESULTS AND DISCUSSION

4.1 Process Optimization

To assess the optimal temperature for the powder extrusion, several trials were conducted. The pre-test heating temperatures before extrusion (i.e., work temperatures) where selected to be RT, 200 °C and 300 °C. After the tensile testing results of the as-extruded samples prepared using these three work temperature conditions, it was found that the UTS of these samples did not have a significant difference. However, the process control data recorded during the extrusion, namely distance vs pressure data, demonstrated that with the working temperature at 300 °C the breakthrough pressure was significantly lower than the others work temperatures (**Figure 9**). Because the controlled parameter for extrusion in our experiment is the ram speed, the extrusion machine formed the sample at the desired rate regardless of the pressure t it applied to reach the speed parameter. Therefore, we chose to conduct the powder extrusion by preheating the cans at 300 °C. This lower breakthrough pressure protects the equipment from unnecessary strain during manufacturing where ram speed is controlled.

It is worth noting that the 432 °C - 4.5 hrs heat treatment condition is not an arbitrary choice. This heat treatment was derived from a standard heat treatment for the non-cerium containing alloy 520. That is the only commercial casting alloy that contains 10 wt. % Mg. The as-cast alloy contained pools of Mg in the microstructure, therefore is typically homogenized at 432 °C for 18 hours. For as-cast Al-8Ce-10Mg wt. %, one found that this heat treatment condition resulted in the same microstructural and mechanical properties as when using the standard stepped heat treatment typically used for the A206 alloy [**57**]. Thus, we choose this same temperature as part of our heat treatment conditions at a time exposure of 4.5 hours.

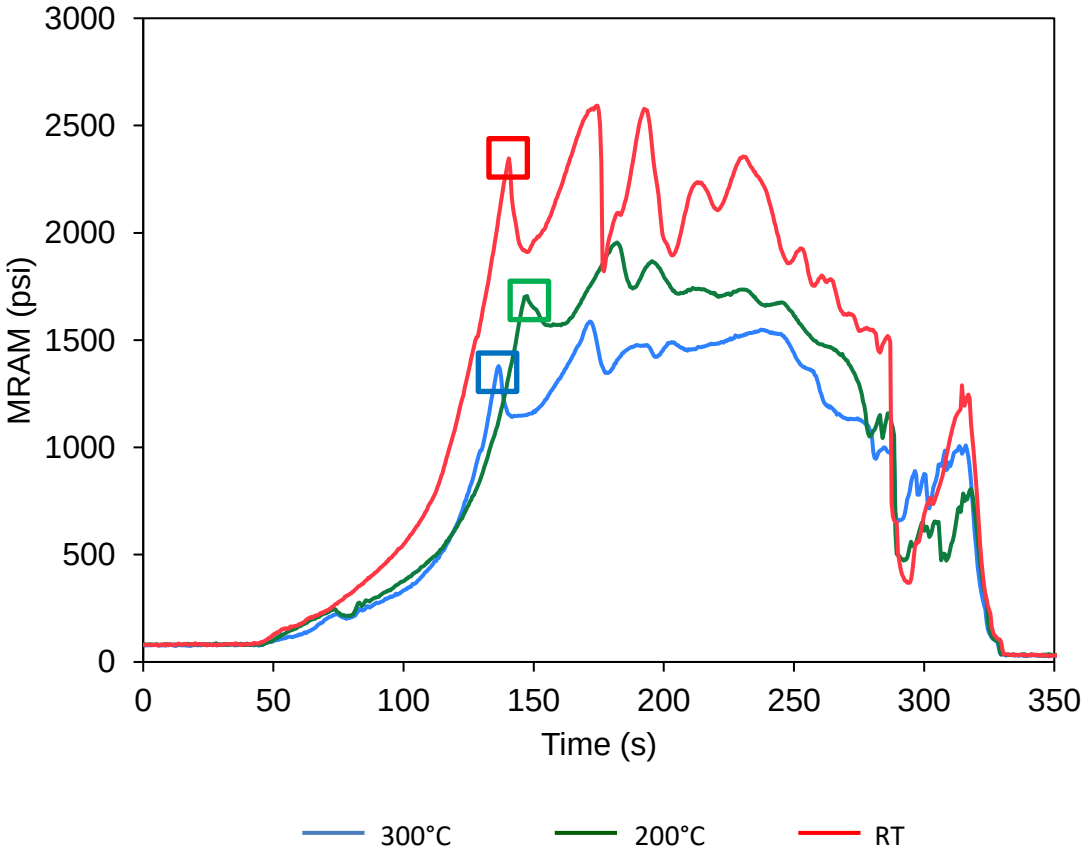

Figure 9. Example of breakthrough pressure vs. time data collected from trial tests with different working temperatures of room temperature, 200 °C, and 300 °C.

4.2 Thermodynamical Modeling

Thermodynamic modeling of the composition Al-8Ce-10Mg wt. % was done using the proprietary database and approach described by Moore, Emily E., et al. [**51**]. **Figure 10** shows the Al-Ce-Mg ternary phase transformation diagram at 100 °C. At the composition of interest for this research the phases presents are Alα, $Al_{11}Ce_3$ and $Al_{140}Mg_{89}$ (β) phase. At 400 °C the calculated isothermal section at the Al-8Ce-10Mg wt. % composition, the β phase is not present, while Alα, $Al_{11}Ce_3$ and $Al_{13}CeMg_6$ (τ) phases are present **Figure 11**. Same as in 400 °C at 500 °C the calculated isothermal section at the alloy composition has the Alα, $Al_{11}Ce_3$ and τ phases present (**Figure 12**).

Thermodynamic calculations of amount of phase fraction of composition Al-8Ce-10Mg wt. % is showed in **Figure 13-a**. For the solidification pathway, $Al_{11}Ce_3$ starts forming from the melt at 732 °C, followed by Al at 593 °C. The alloy is solidified at 501 °C, corresponding to the maximum concentration of the Alα and $Al_{11}Ce_3$ phases. After, solidification solid state diffusion under equilibrium would lead to τ and β phases form from magnesium diffusion. $Al_{13}CeMg_6$ τ phase maximum corresponds to 207 °C, same temperature of total dissolution on to $Al_{11}Ce_3$ and β phases. This also agrees with literature that reports $Al_{13}CeMg_6$ τ forms at 492 °C and have a decomposition temperature between 320 °C and 400 °C [**42**].

In **Figure 13-b-c-d** calculation of elemental amount in at. % per phase in function of temperature are plotted. In **Figure 13-b** all Al is in liquid state until 593 °C is reached, this is when Al starts to solidify in the Al phase. The amount of Al in the Al phase decreases until total solidification at 501 °C, after this there is a constant increase of Al % in the Alα phase and the maximum amount of 100 at. % is at 0 °C. The Al atomic percentage on the $Al_{11}Ce_3$ phase is constant at ~78.6 since its formation at 732 °C. It also has a constant amount of Al ~61.14 at. % on the β phase from the formation at 207 °C. At 501 °C τ phase has a constant amount of Al at 65 at. %, up to the dissolution of the phase at 207 °C. Even when the plot shows a diminution in Al at. % amount and later increase (at 501 °C) , is clear that the Al phase is not getting depleted of Al, otherwise we will see other phases gaining Al. In fact, the Al_{α} phase is gaining Mg at 593 °C as showed in **Figure 13-c**, meaning that

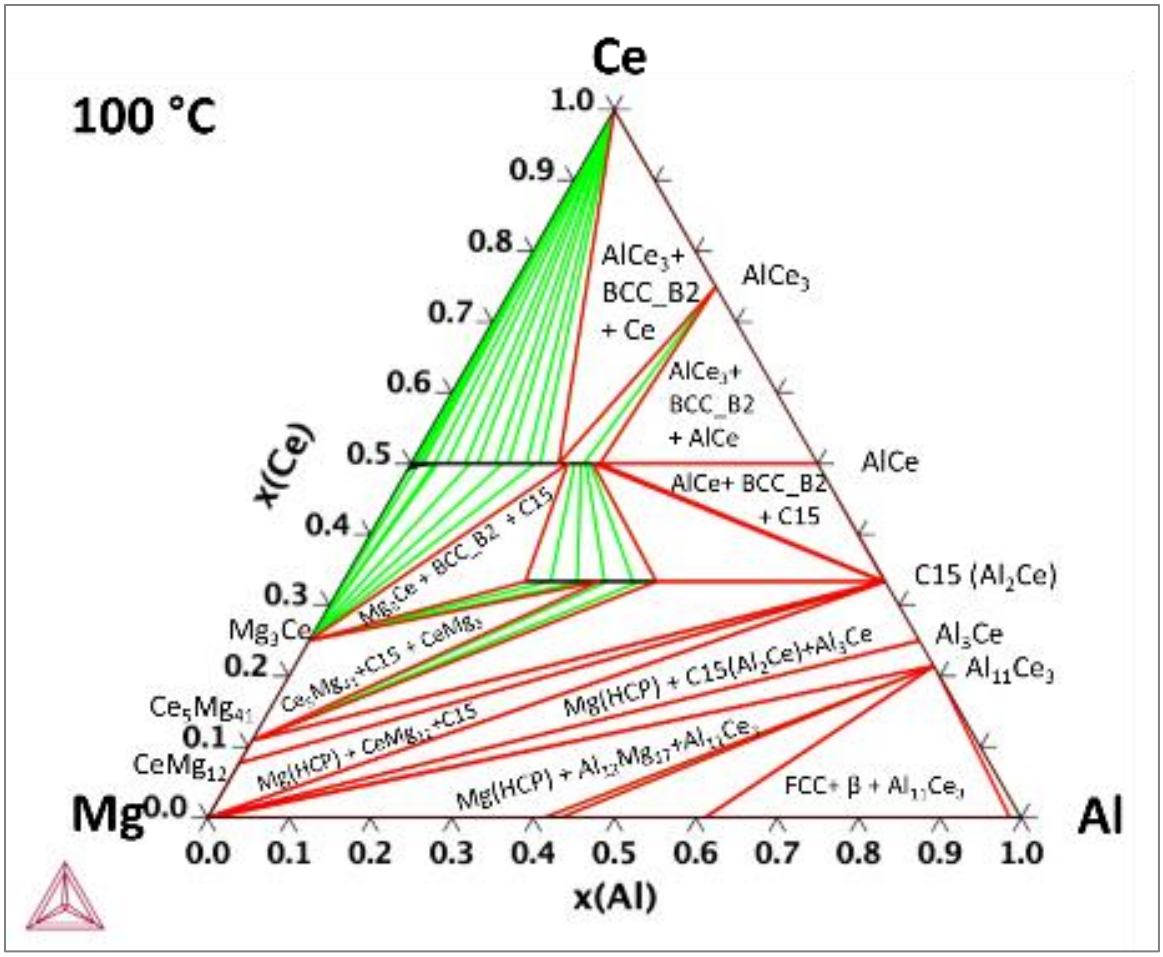

Figure 10. Calculated isothermal section of Al-Ce-Mg at 100 °C.

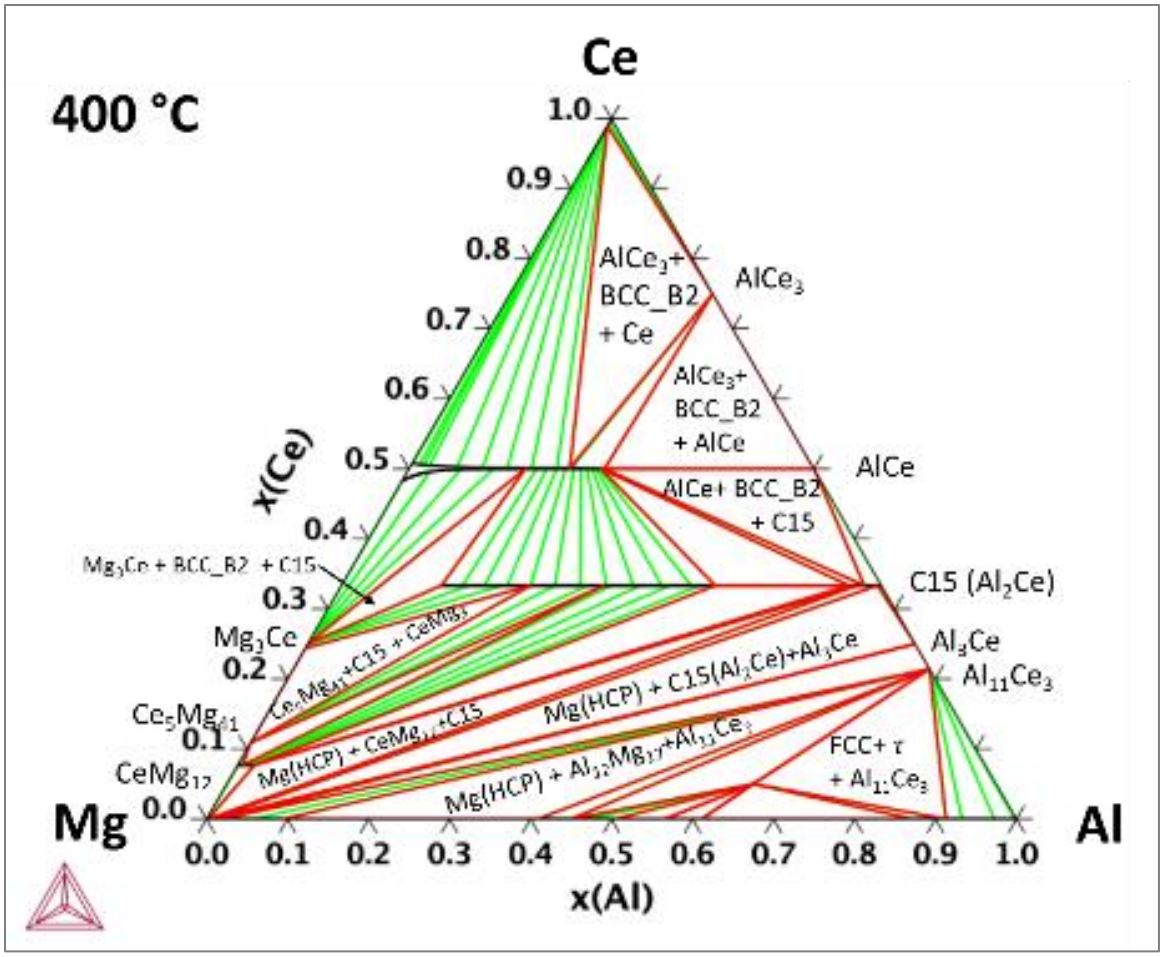

Figure 11. Calculated isothermal section of Al-Ce-Mg at 400 °C.

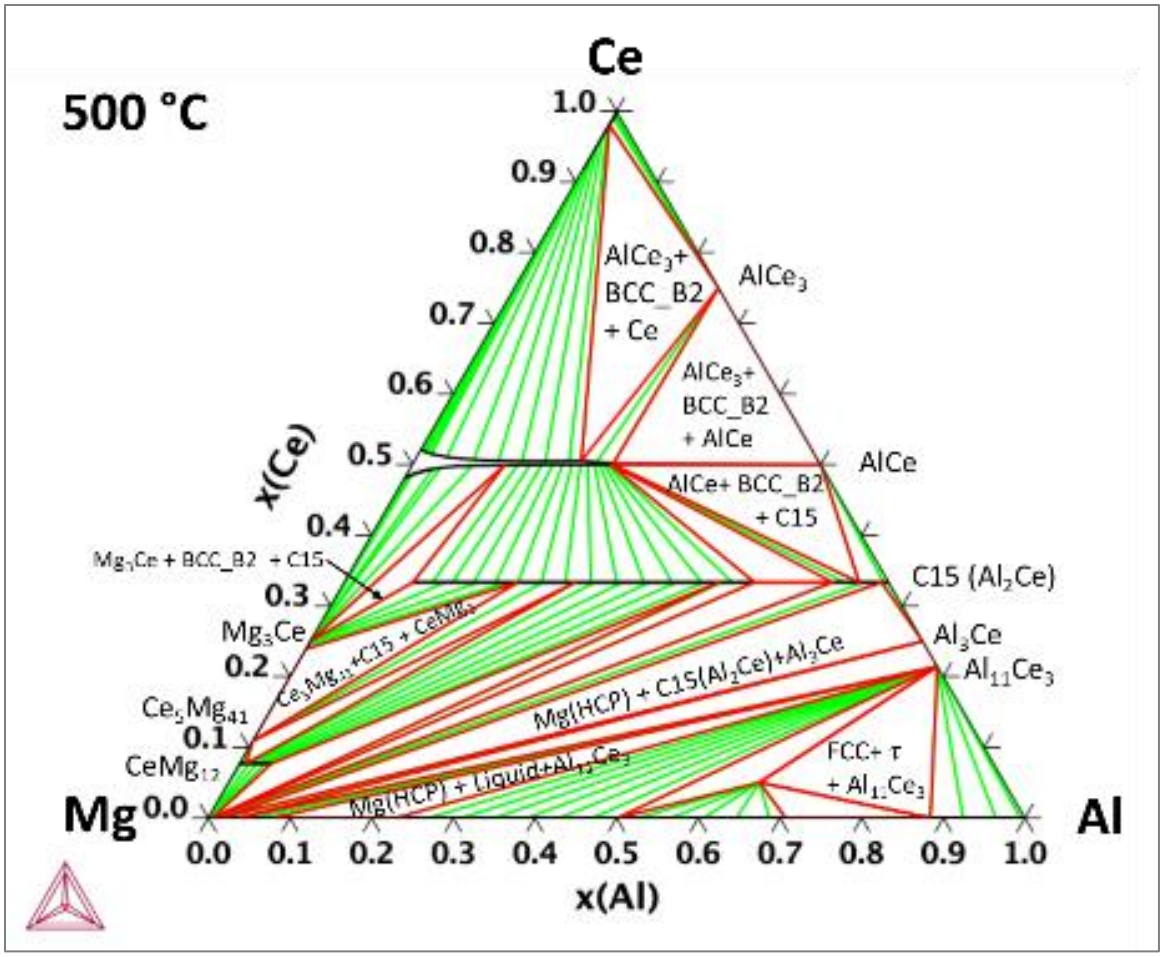

Figure 12. Calculated isothermal section of Al-Ce-Mg at 500 °C.

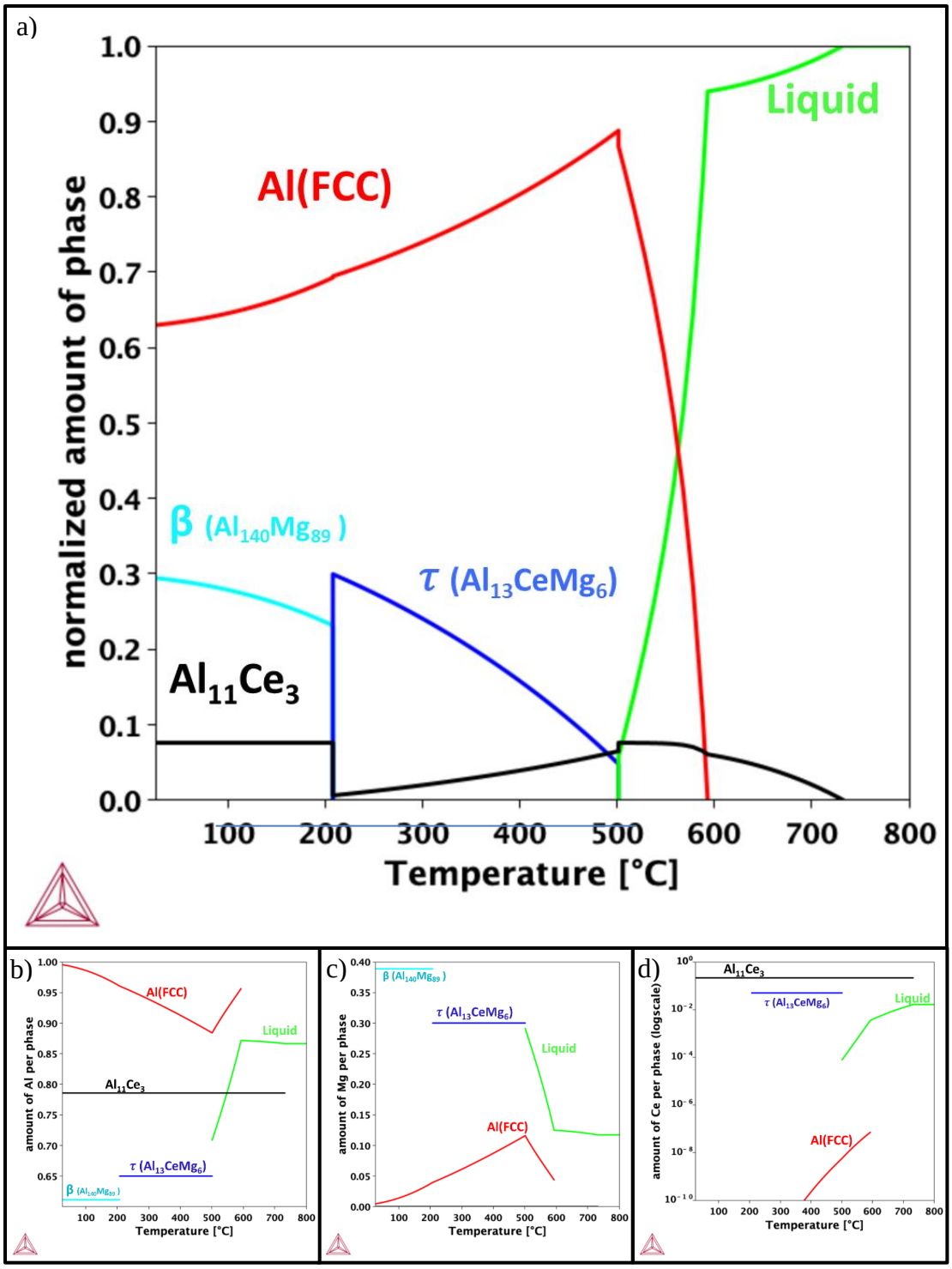

Figure 13. Thermodynamics calculations of Al-8Ce-10Mg a) Phase fraction calculations (wt. %). b), c), and d) Amount of element (Al, Mg, and Ce respectively) per phase in function of temperature.

there is a change in Mg to Al ratio on the Al_{α} phase. The maximum amount of Mg in solid solution in the Al_{α} phase occurs at 501 °C where the formation of the τ phase take place. Calculation of at. % of Ce is plotted in log scale **Figure 13-d**. In $Al_{11}Ce_3$ from 732 °C the amount of Ce is constant (~21.43 at. %) down to 0 °C. The amount of Ce in the τ phase is 5 at. %. On the Al phase the amount of Ce is extremely low, where the maximum amount of Ce in solid solution is less than 10^{-7} at. % at 593 °C thus the reason to plot in a log scale, this amount is minimal and entirely negligible. This shows the almost zero diffusion of Ce in Al as states before.

Because we made powder by atomization, rapid cooling creates a solidification that occurs at non-thermal equilibrium. In consequence, phases that are present after a slower cooling rate process may be present. This is the case of the metastable $Al_{13}CeMg_6$ phase. Metastability refers to a phase or state that exists outside its thermodynamic stability range but can persist for a certain period due to kinetic barriers. In the case of $Al_{13}CeMg_6$, it may form under non-equilibrium conditions such as rapid solidification.

4.2.1 Summary of Thermodynamical Modeling

Calculations predicted Calculations predicted four equilibrium phases in the alloy during cooling from the liquid phase, namely, Al_{α}, $Al_{11}Ce_3$, $Al_{140}Mg_{89}$ β, and $Al_{13}CeMg_6$ τ. Also, the calculation showed that the $Al_{13}CeMg_6$ τ and $Al_{140}Mg_{89}$ β phases do not coexist, and the presence of one or the other depends on the solidification of the material, i.e., equilibrium (β) or non-equilibrium (τ) solidification at room temperature. We expect to find τ phase and not β in the as-extruded samples, because of the non-equilibrium rapid solidification of the powder during the gas atomization process and subsequent warm extrusion process. This is also consistent with the literature reporting on Al-Ce-Mg parts made by additive manufacturing where non-equilibrium rapid solidification during the processing produces τ phase instead of the β phase [**58**]. The potential for coarsening of the τ phase at elevated temperatures could be detrimental to the high-temperature mechanical performance. We used these thermodynamic calculations to design a heat treatment experiment with the goal of lowering the τ phase content, while creating more Al_{α} and

thermally stable $Al_{11}Ce_3$ phases, using the results presented in **Figure 13** where the τ phase percentage lowers with temperature exposure from 201 °C to 501 °C.

Subsequently, we first confirm the phases present using a series of measurements. And then, microstructure analysis results will be presented to further verify the microstructure and morphology of the intermetallic phases. The expectations of these next experimental tasks include the following.

- Because of non-equilibrium solidification from the rapid cooling during the powder processing and the subsequent warm extrusion, the grain growth was suppressed, and a nanostructured material was created.
- Based on the thermodynamic calculations and the fact that the alloy powder was formed under non-equilibrium solidification condition, XRD will corroborate that the phases present are Al_α, $Al_{11}Ce_3$, and $Al_{13}CeMg_6$ τ, whereas the β phase will not be present.
- Based on the thermodynamic calculations, we designed a heat treatment experiment (described in section **3.4**) to reduce the amount of τ phase and create more Alα and $Al_{11}Ce_3$ phases.

4.3 X-Ray Diffraction (XRD)

XRD patterns were collected for as-extruded and all heat treatment conditions. Starting with the as-extruded condition (black line) (**Figure 14**), we identified that the phases present are Al_α, $Al_{11}Ce_3$, and the τ phase $Al_{13}CeMg_6$, this was predicted by the thermodynamical calculations, corroborating rapid and non-equilibrium solidification. β phase is not present, because of rapid cooling. The presence of $Al_{13}CeMg_6$ τ phase eliminates the possibility of finding β phase because by thermodynamics these phases do not coexist. $Al_{13}CeMg_6$ τ phase is known to crystallize in space group P63/mmc with the structure type of $MgNi_2$ with lattice parameters of a = 0.5525(9) and b = 1.7866(2) nm. $Al_{13}CeMg_6$ τ phase is present in large fraction in the as-extruded samples, as shown in **Figure 15-c** at peaks in 31.21° $\{105\}_\tau$ and 32.38° $\{110\}_\tau$ for the $Al_{13}CeMg_6$ τ phase [**42**].

In identifying the Al_α peaks, to account for Mg in the Al_α solid solution we used the stoichiometry of a phase (like $Al_{3.7}Mg_{0.3}$) that has low Mg in solid solution with Al.

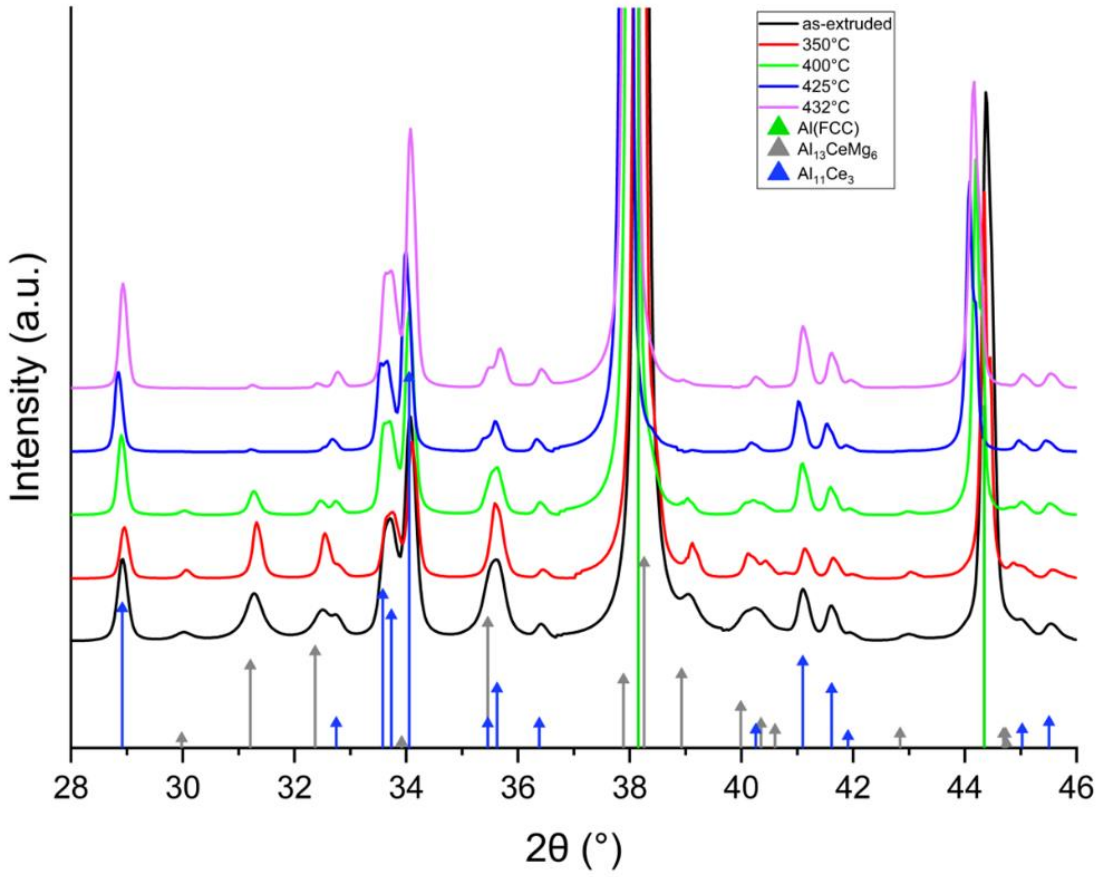

Figure 14. Example of XRD pattern of as-extruded and heat-treated conditions. Three phases were identified: Al, $Al_{11}Ce_3$, and $Al_{13}CeMg_6$.

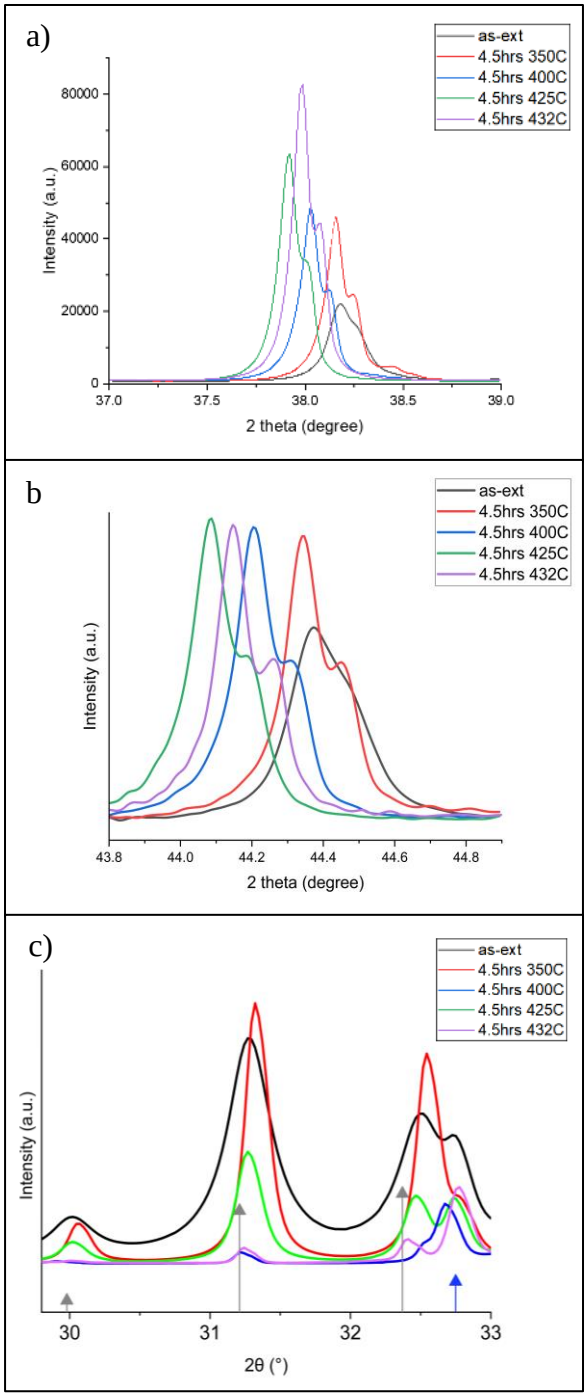

Figure 15. Diffraction pattern of a) Al $\{111\}_{\alpha}$ peak from 37°- 39° (111 peaks correspond to diffraction with Cu K-α_1, and shoulder peaks to Cu K-α_2), b) and $\{200\}_{\alpha}$ peak from 43.8°- 44.9°, and c) detail of pattern around 30°- 33° of $\{105\}_{\tau}$ and $\{110\}_{\tau}$ peaks.

Even though we cannot precisely quantify the amount of Mg in solution with Al, the used stoichiometry is more realistic than using the stoichiometry of pure Al to identify the peaks. The presence of Mg in the Al increases the lattice parameter, compared to pure Al. This causes the Al $\{111\}_\alpha$ and $\{200\}_\alpha$ peaks to shift to lower 2-theta values.

First, after the heat treatment, the Al_α solid solution has a larger lattice parameter (and shifts to lower 2-theta values). Al_α peaks $\{111\}_\alpha$ and $\{200\}_\alpha$ in the samples consistently shift to lower 2-theta values with the increase in heat-treatment temperature. However, for the samples heat treated at 432 °C for 4.5 hrs there is an evident shift back to a higher 2-theta value between the samples heat-treated at 400 °C and 425 °C (**Figure 15-a-b**). Secondly, τ phase amount decreases gradually after the heat treatments at higher temperatures, while $Al_{11}Ce_3$ and Al_α phases increase. **Figure 15-c** is a representative example of the trend of τ phase decreasing after heat treatment. These angles of diffraction were chosen for visual representation of τ peaks behavior after heat treatment because there is not much overlapping with peaks from other phases.

The observation of τ lowering with heat treatment temperature increment is in a good agreement with the thermodynamic calculation results presented in **Figure 13.** This is due to the dissolution of τ $Al_{13}CeMg_6 \rightarrow Al_{11}Ce_3 + Al_\alpha$.To better quantify the amount of Mg that goes in Al phase (from the dissolution of τ) we used the methodology described in the next paragraphs.

According to published experimental data (at. % Mg vs lattice parameter) there is a linear relation between the Al solid solution lattice parameter and the amount of Mg dissolved in that phase [**59**]. We utilized the available data of lattice parameter variation measurement as a function of dissolved Mg, plotted the data and obtained a linear fit of the data (**Figure 16**). As a result, we obtained the linear formula $y = 2245.69\,x - 909.10$ where *x* is the lattice parameter in nm and *y* is the atomic percentage of Mg in solution. The diffraction pattern of each heat treatment condition was used, specifically 2-theta diffraction angle of the $\{111\}_\alpha$ and $\{200\}_\alpha$ peaks, to get theta, d-spacing (*d*) in nm, and lattice parameter (*a*) in nm by the formula $a = \sqrt{h+k+l} \times d$. Because XRD data was collected from each sample at least twice, the average of at. % Mg in the as-extruded sample was used as a base amount or starting point. Then the average of at. % Mg of each heat-treated condition was

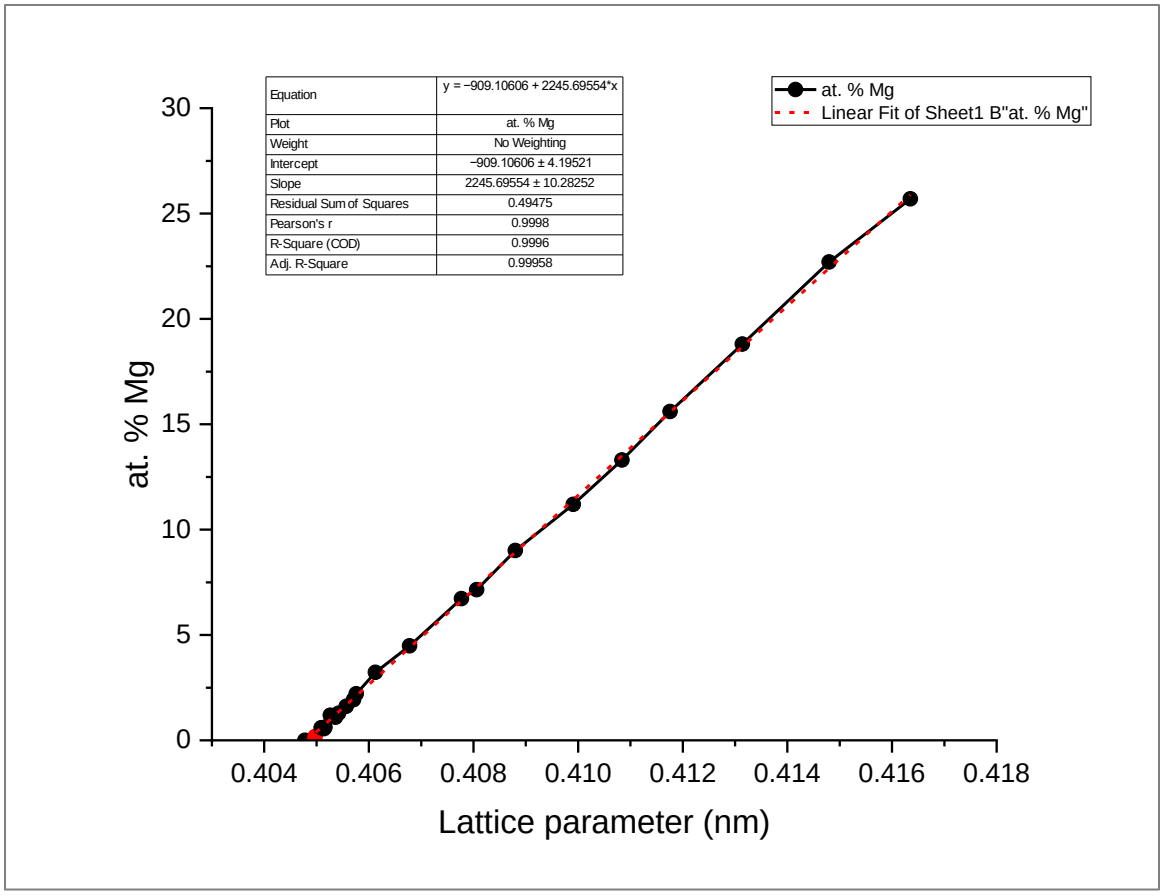

Figure 16. Lattice parameter of Al phase as a function of atomic percentage of Mg in solid solution. The lattice parameter data is from [59].

used to get a difference or relative change of at. % Mg in the Al_{α} structure. It is important to point out that even when we cannot give an absolute value of systematic changes of Mg in solid solution in the as-extruded condition, by using the current approach we could estimate the amount of Mg dissolved in Al after the different heat treatment processes. The calculation estimation is summarized in **Table 4**. There is a trend in increased at. % of Mg in the Al_{α} phase with the increase in the heat treatment temperature. For the 432 °C case there is an increase of lattice parameter compared with the base amount (as-extruded) however , the increase is less than the heat treatment condition at 425 °C. The lattice parameter increase with thermal exposure is due to the amount of Mg going into the Al solid is solution, as a result from the dissolution of τ phase with temperature increase.

4.3.1 Summary of X-Ray Diffraction

From the XRD studies, we experimentally confirmed that the three phases in the as-extruded sample are $Al_{13}CeMg_6$, $Al_{11}Ce_3$, and Al_{α}. The working temperature during the extrusion and subsequent cooling did not remove the $Al_{13}CeMg_6$ phase, because at 300 °C the phase has not reached the dissolution temperature stated before. In contrast, through the XRD, we confirmed that the temperatures selected for the heat treatments (in the range where the dissolution of τ was predicted by thermodynamics calculation) lowered the amount of τ phase with the increase in the heat treatment temperature, producing higher amounts of $Al_{11}Ce_3$ and Al_{α} phases.

Dissolution of $Al_{13}CeMg_6$ in to $Al_{11}Ce_3$ and Al_{α} is consistent with the literature. Sisco et.al. found than on Al-10.91Ce-7.54Mg and Al-14.5Ce-9.22Mg (wt. %) after hot isostatic pressing (HIP), $Al_{13}CeMg_6$ peaks XRD pattern reduce intensity, and suggested that the phase is a metastable one in the solidification structure [**58**]. The presence of the metastable τ phase in the as-extruded samples confirms rapid cooling of the original powder, therefore, when analyzing the microstructure, we would expect:

- a nanostructure
- very limited dissolution of Ce in Al after heat treatment, and the thermally stable $Al_{11}Ce_3$ phase will prevent coarsening, allowing to preserve the nanostructure.

Table 4.Calculation of the changes in atomic percentage of Mg in solution in the Al lattice.

	Al {111} Peak					Al {200} Peak						
	2-theta (deg)	**theta (deg)**	**d spacing (nm)**	**lattice (nm)**	**Mg at.%**	**2- theta (deg)**	**theta (deg)**	**d spacing (nm)**	**lattice (nm)**	**Mg at.%**	**average Mg at.%**	**ΔMg at.%**
AS-EXT	**38.1848**	19.09	0.24	0.41	*6.90*	**44.3728**	22.19	0.20	0.41	*7.07*	6.96	*base amount*
	38.1845	19.09	0.24	0.41	*6.91*	**44.3791**	22.19	0.20	0.41	*6.95*		
4.5HRS 350C	**38.1588**	19.08	0.24	0.41	*7.50*	**44.3468**	22.17	0.20	0.41	*7.58*	*7.53*	***0.57***
	38.1601	19.08	0.24	0.41	*7.47*	**44.3475**	22.17	0.20	0.41	*7.57*		
4.5HRS 400C	**38.0288**	19.01	0.24	0.41	*10.52*	**44.2168**	22.11	0.20	0.41	*10.14*	*10.33*	***3.37***
	38.0277	19.01	0.24	0.41	*10.55*	**44.2179**	22.11	0.20	0.41	*10.12*		
4.5HRS 425C	**37.9248**	18.96	0.24	0.41	*12.95*	**44.0868**	22.04	0.21	0.41	*12.72*	*12.59*	***5.63***
	37.9356	18.97	0.24	0.41	*12.70*	**44.1239**	22.06	0.21	0.41	*11.98*		
4.5HRS 432C	**37.9800**	18.99	0.24	0.41	*11.66*	**44.1453**	22.07	0.20	0.41	*11.56*	*11.45*	***4.49***
	37.9753	18.99	0.24	0.41	*11.77*	**44.1465**	22.07	0.20	0.41	*11.53*		
	38.0016	19.00	0.24	0.41	*11.16*	**44.1728**	22.09	0.20	0.41	*11.01*		

4.4 Microstructural Analysis of Alloy Powders and Extruded Samples

4.4.1 As-Received Alloy Powder

The as-received powder exhibits some porosity and a dendritic microstructure (light gray) without forming blocky $Al_{11}Ce_3$ phases, due to the rapid cooling (**Figure 17**). A further examination using SEM, revealed that the dendritic and cell morphology was Al matrix (dark gray marked **a**). There is a nano-scale intermetallic network composed of $Al_{11}Ce_3$ (bright phase marked **b**) and $Al_{13}CeMg_6$ (light gray marked **c**) (**Figure 18**).

To verify where the elements are present in the microstructure, we did EDS mapping. This was very challenging to do because of the very small features of the microstructure and the resolution of the SEM. **Figure 19** displays the results of SEM/EDS mapping. Is evident from the figure (labeled **Al**) that all the three phases contain Al. EDS confirmed that the dendrites consist of only Al_{α}, and the intermetallic network contains both Ce and Mg. In the composition image, at the inset square, is easy to appreciate the three phases in the material: Al in the dark gray zone, $Al_{11}Ce_3$ in the brightest part, and the $Al_{13}CeMg_6$ phase in the light gray area (**Figure 20**). The $Al_{13}CeMg_6$ phase can be distinguished from the bright phase ($Al_{11}Ce_3$) in the intermetallic and as shown in the figure (labeled **Mg**), does not contain Mg.

It was learned from EDS mapping that Ce containing phases will appear bright in an SEM image, a phase with high Ce content looks brighter than a phase with lower content of Ce. We have only two phases containing Ce, one of them ($Al_{11}Ce_3$) has significantly more at. % amount of Ce than the other ($Al_{13}CeMg_6$). With this knowledge we used ImageJ software to qualitatively analyze the average area fraction of each phase. With this approach we estimated an area percentage of about 8 % of the very bright phase of high Ce content (presumably $Al_{11}Ce_3$), ~20 % of bright phase with less Cerium content (presumably $Al_{13}CeMg_6$), and ~72 % of Al matrix. ImageJ software approximation to phases percentage is showed in **Figure 21**. The result is also summarized in **Table 5**.

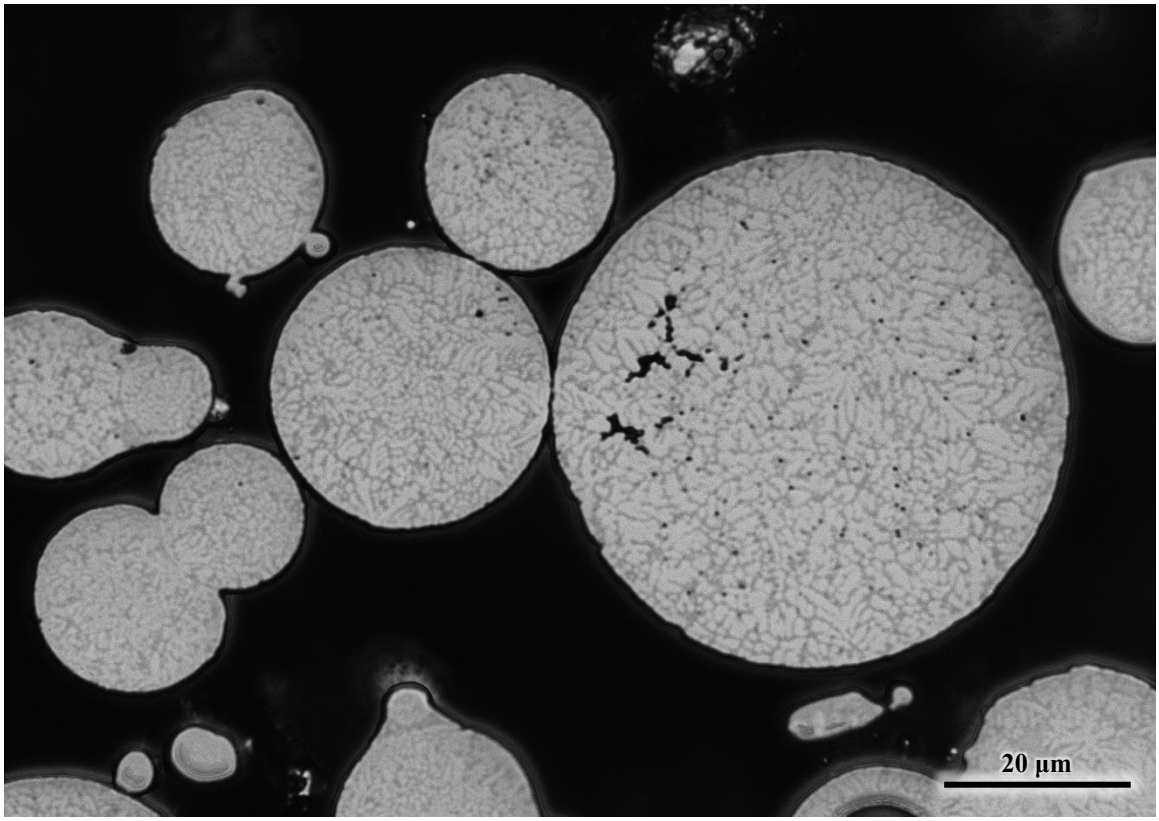

Figure 17. Optical micrograph of the cross section of the as-received Al-8Ce-10Mg wt. % powder particles before extrusion.

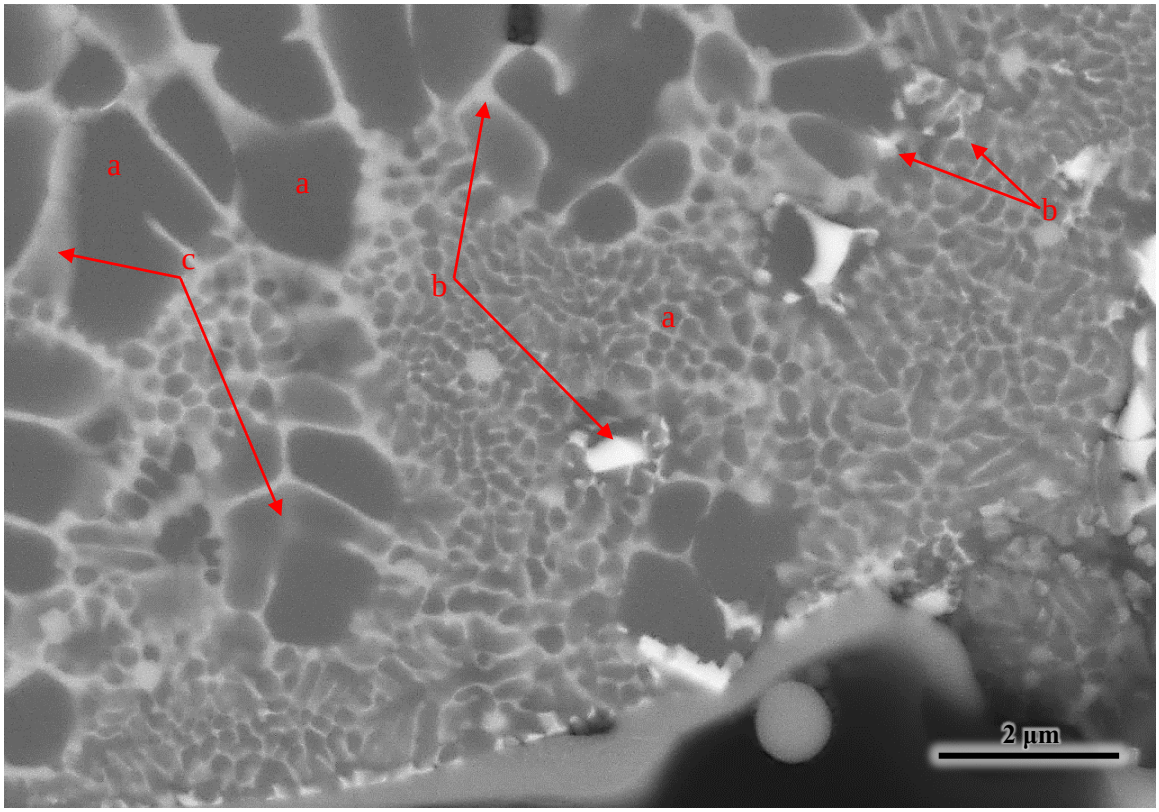

Figure 18. SEM image of the as-received powder before the extrusion, detail of the nanonetwork that surrounds the Al matrix dendrites and cells are shown.

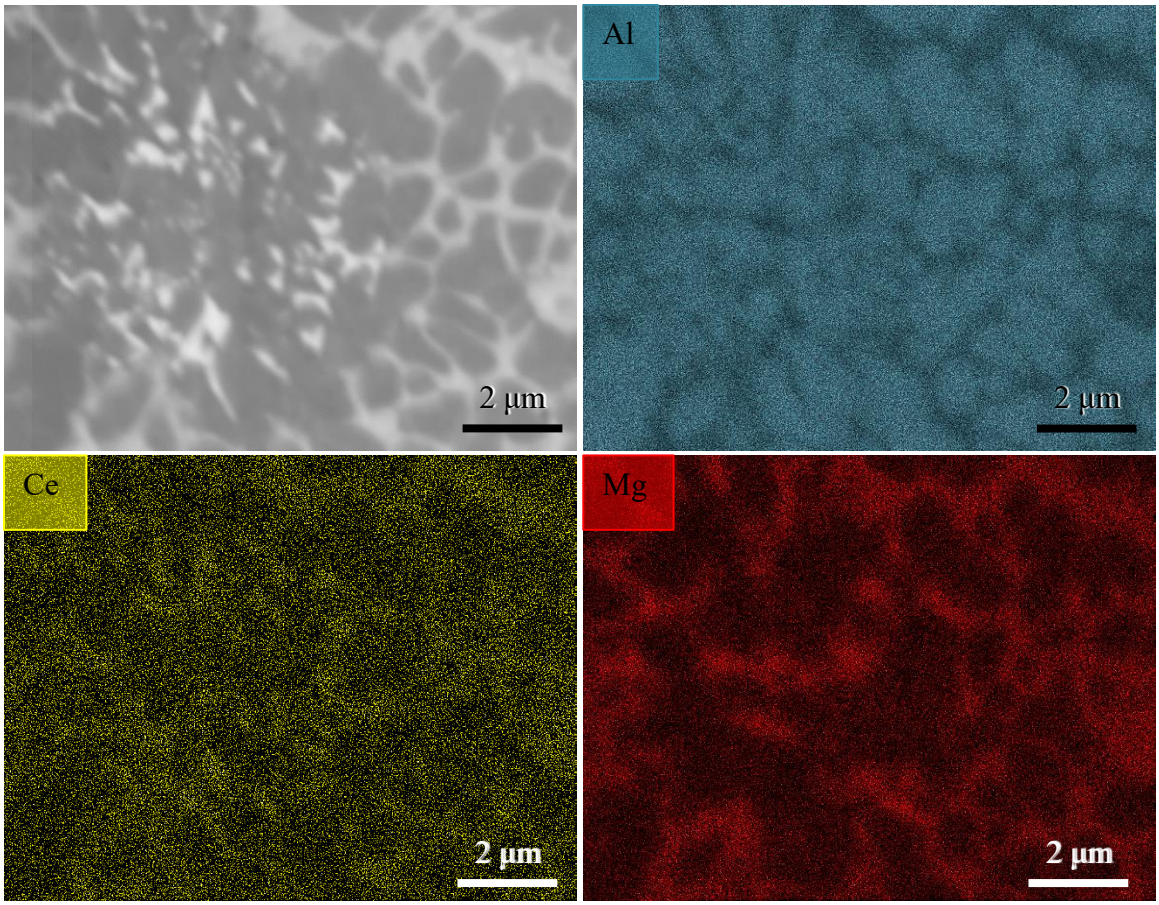

Figure 19. SEM/EDS elemental mapping of powder before extrusion, three elements are present: Al, Ce, and Mg.

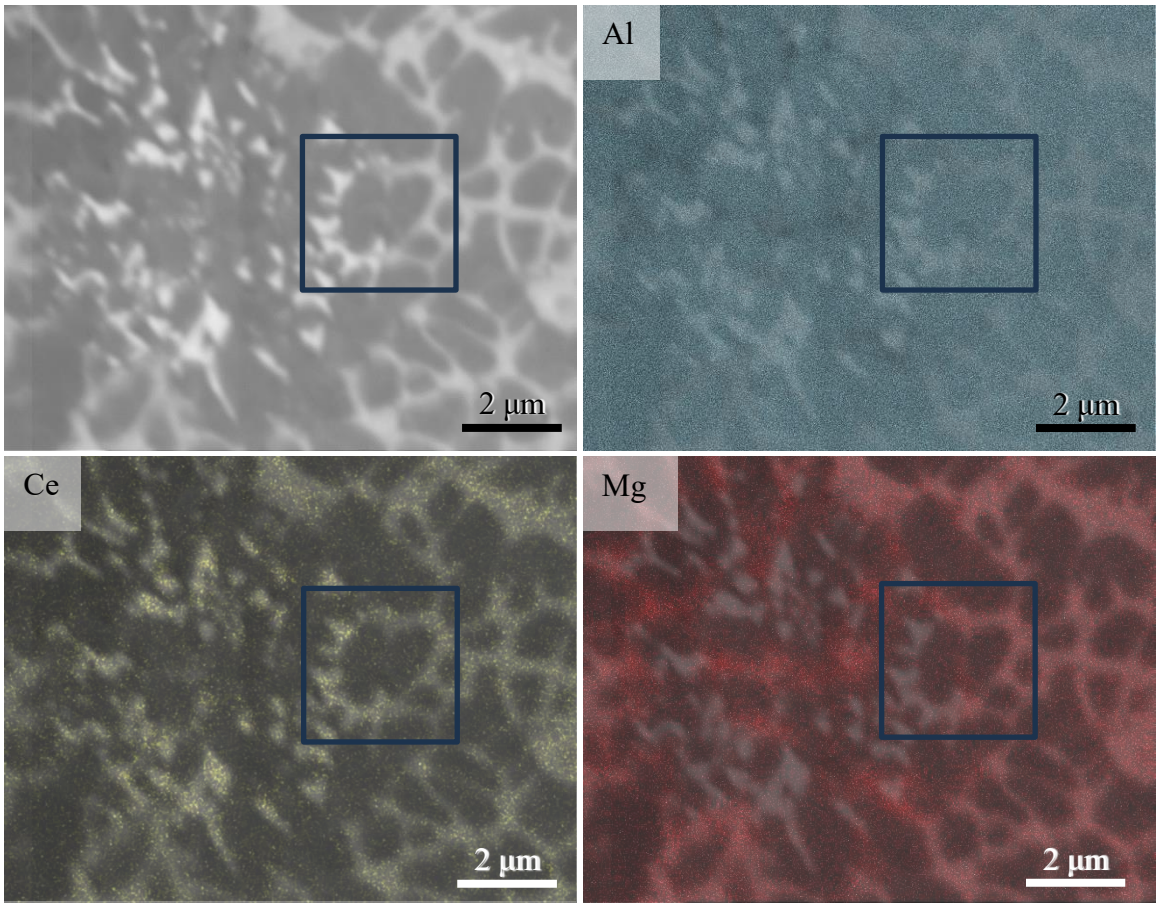

Figure 20. SEM/EDS elemental mapping of powder before extrusion. Composition image three elements are present: Al, Ce, and Mg.

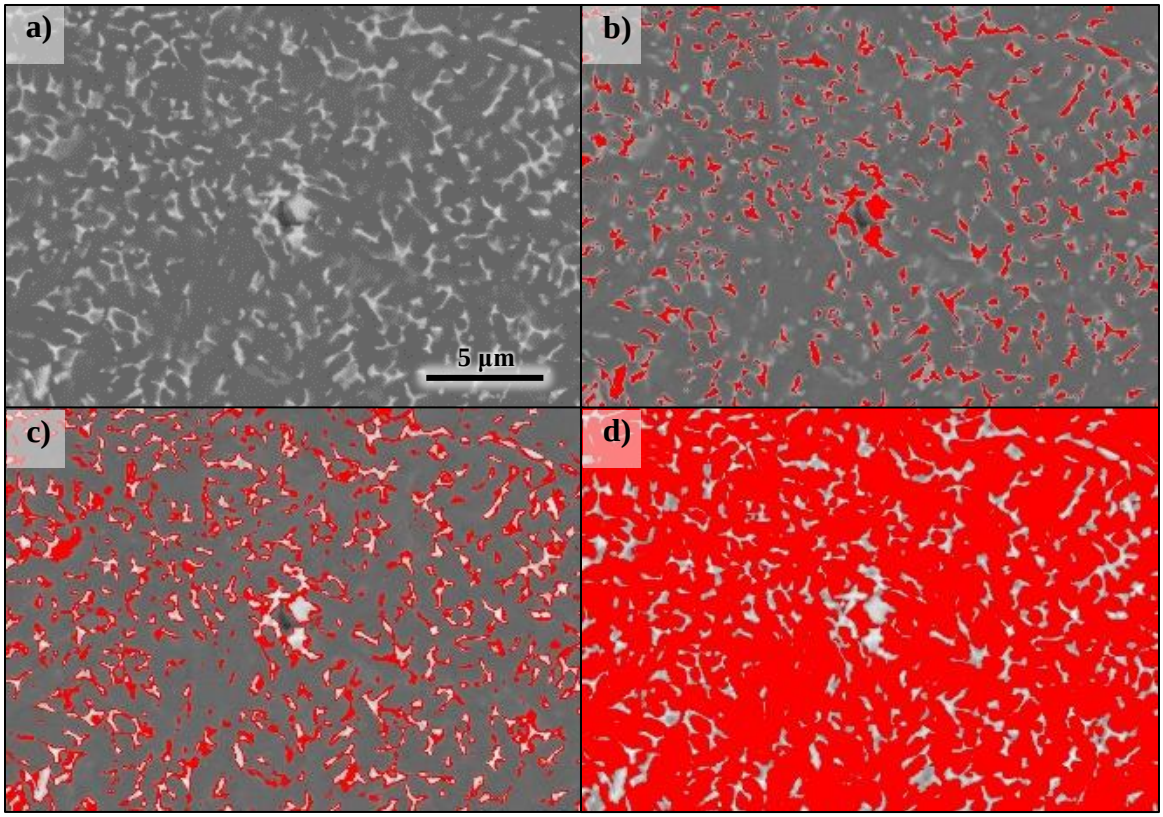

Figure 21. SEM image of a) as-received powder. ImageJ analysis of the SEM image b) Very bright phases (high Ce content) c) bright phase (less Ce content) d) Al matrix.

Table 5. Summary results of average area phase fraction analyzed via ImageJ of as-received powder.

	Al	**$Al_{11}Ce_3$**	**$Al_{13}CeMg_6$**
Aver. area phase fraction	71.79	8.58	19.62
s.e.	1.760	0.236	1.638

Compared with thermodynamic calculations of phase fraction in Al-8Ce-10Mg (wt. %) the phase fraction percentage amount estimated by ImageJ are not consistent with a phases amount at any temperature. For example, in thermodynamic calculations 20 % of τ phase is present at ~ 350 °C, 8 % of $Al_{11}Ce_3$ is the maximum percentage of this phase and is present between 501 °C to ~565 °C, and Al phase at 72 % is present at ~265 °C. The only consistent result between this image analysis approach and thermodynamic calculations is that all the phase fraction amounts are present during non-equilibrium solidification, like rapid cooling during powder atomization. This approach does not seem to be very accurate, parameters of image resolution and choosing of threshold to define a phase in the image, give a lot of uncertainty to this test, in particular this case where three phases are present.

4.4.2 Extruded Samples

After the extrusion, the fine microstructure, like the powder before extrusion, is still present. **Figure 22** shows a high Ce-containing phase (lightest gray marked **a**) with features as small as 20 nm. Low porosity is present in the as-extruded samples (**Figure 23**), with barely distinguishable intermetallics particles, and there is a formation of blocky $Al_{11}Ce_3$ as shown in **Figure 23-a**.

We selected for optical imaging the heat treatment condition with highest temperature and longest time exposure (i.e., 432 °C - 4.5 hrs) to highlight the effect of post-extrusion heat treatment on the overall microstructure (**Figure 24**). Some blocky $Al_{11}Ce_3$ phases are present in the fine morphology in **Figure 24-b**. The optical micrographs show higher porosity compared to the as-extruded condition.

The blocky $Al_{11}Ce_3$ phase was identified not only by its characteristic morphology, but also by SEM/EDS mapping, where it confirms that this phase only contains Al and Ce (**Figure 25**). Since the blocky$Al_{11}Ce_3$ phase was not present in the powder before extrusion, these few formations of blocky $Al_{11}Ce_3$ can be due to high pressure and temperature during extrusion, and the high affinity of Ce to Al and to react within itself. This combination of factors can create a driving force for nucleation sites and formation of blocky $Al_{11}Ce_3$.

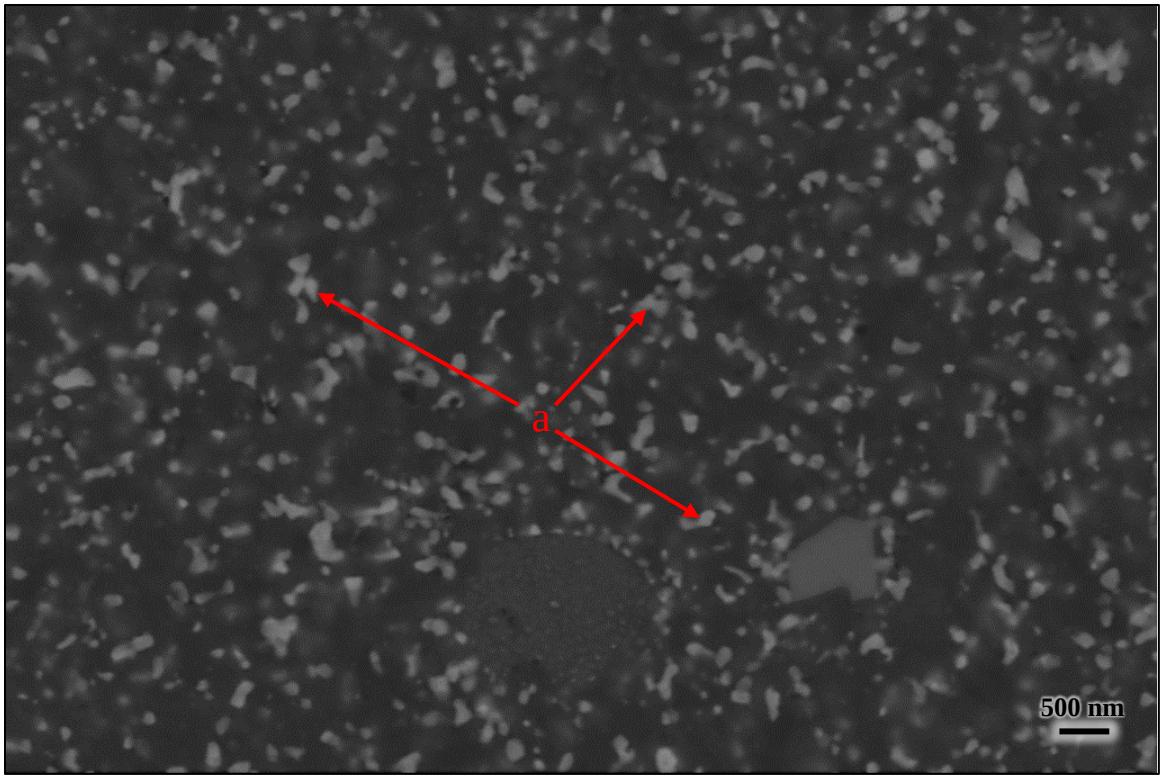

Figure 22. SEM image of an as-extruded sample (perpendicular to the extrusion direction).

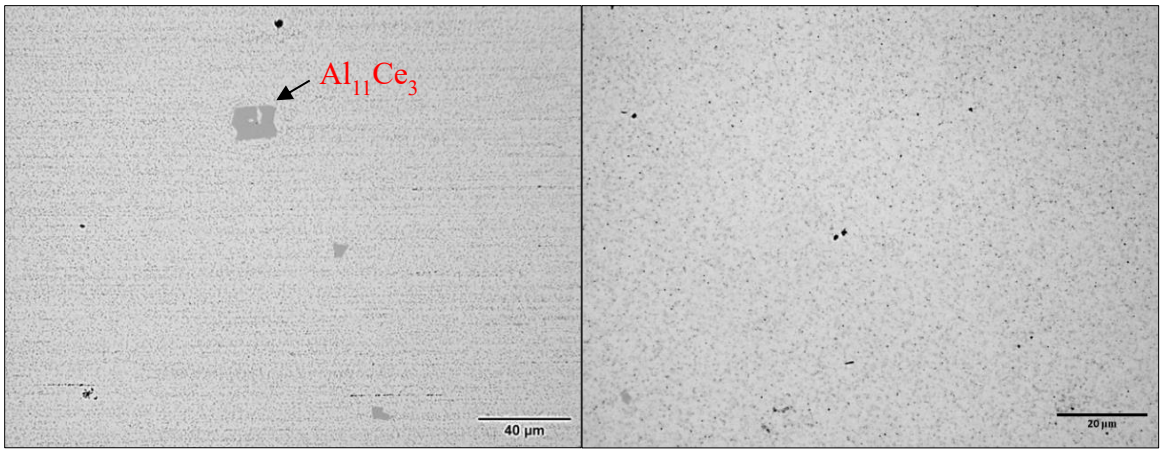

Figure 23. Optical micrograph of as-extruded sample: (a) longitudinal cross section and (b) transverse cross section

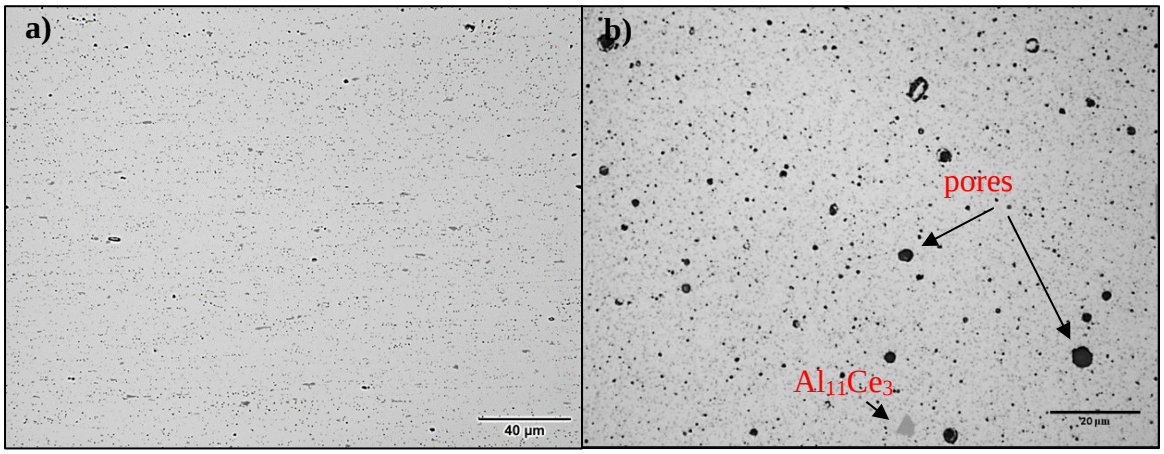

Figure 24. Optical micrograph of sample heat treated for 432 °C - 4.5 hrs: a) longitudinal cross section and b) transverse cross section.

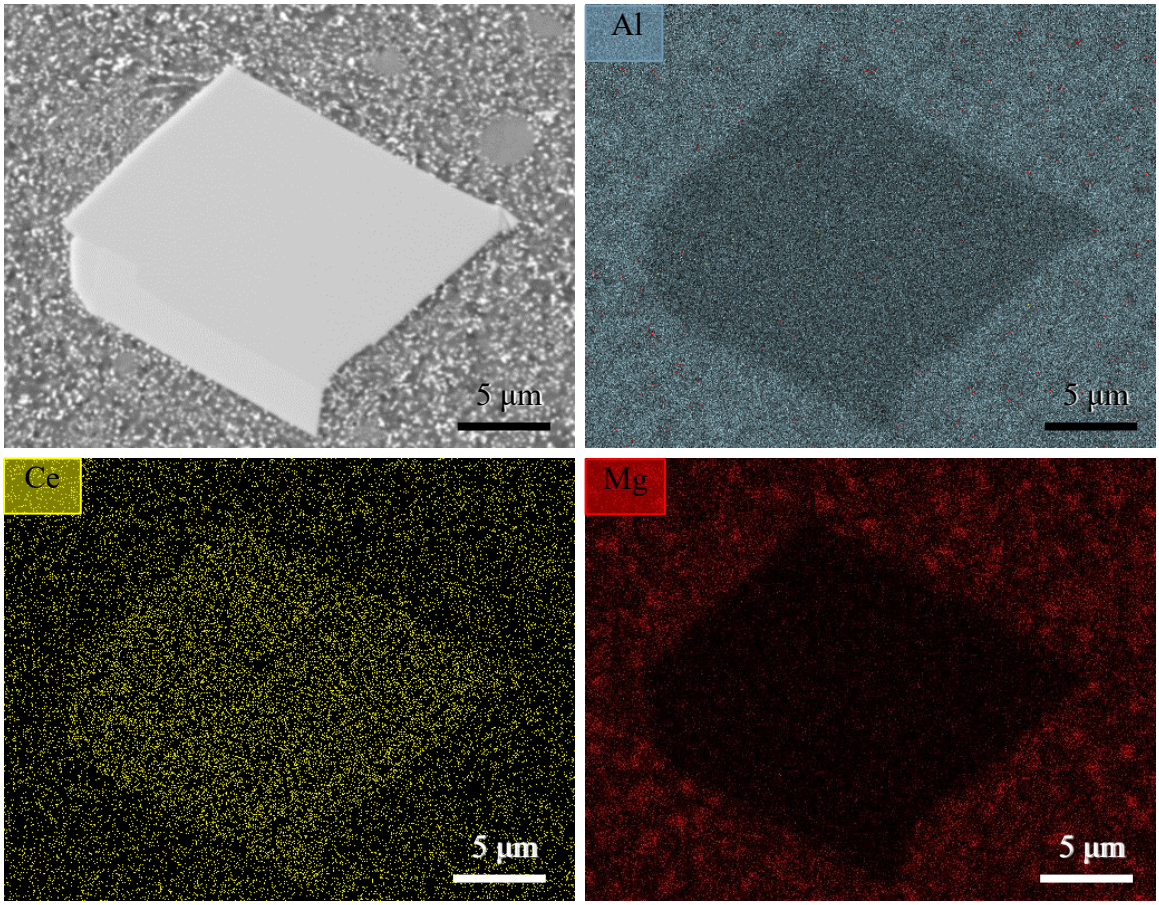

Figure 25. SEM/EDS map as-extruded. The $Al_{11}Ce_3$ phase was identified by its characteristic morphology and mapping shows only Al and Ce are present.

The increased porosity is due to the loss of volatile elements oxygen and magnesium during the heat treatment [**60**, **61**]. The percentage reduction of these elements in the alloy after heat treatments is a very well documented phenomenon [**62**]. For Mg and O, thermal exposure creates high vapor pressure that removes the elements from the alloy. It was previously reported that the temperature where Mg starts to diffuse out of Al alloys is 215 °C [**63**]. The loss of Mg at surface level is due to a near-surface reaction and in consequence Mg levels decrease. The heat-treated sample shown in **Figure 24-b** also indicates some intermetallic particle coarsening compared to **Figure 23-b**.

Figure 26 shows SEM images of the as-extruded and 432 °C - 4.5 hrs samples in the bulk with formation of blocky $Al_{11}Ce_3$ and porosity after heat treatment is also observed.

Higher magnification of SEM images shows the original shape of some larger powder particles in the as-extruded specimen (transverse direction) **(Figure 27-a)**. The evolution of the intermetallic particle size after heat treatment is evident on the 432 °C - 4.5 hrs (**Figure 27-b**). We used the ImageJ software to qualitatively determine changes in intermetallic particle average size and distribution after heat treatment. There is a trend of coarsening of the microstructure with heat treatment temperature increase, as can be observed in **Figure 28** and quantified (intermetallic size and distribution) in **Figure 29**. Results are summarized in **Table 6**.

These qualitative measurements, using ImageJ, can be used to model and predict the material's behavior and correlating the results with other technics, such as SAXS for quantifying intermetallic particle size and distribution. This SEM image analysis results will be later compared to the TEM imaging and to USAXS results, for a more comprehensive analysis for the particle size and distribution.

TEM allowed investigating the presence of nanoparticles in the heat-treated sample 432 °C - 4.5 hrs. We used bright field images and found nano-scaled intermetallic particles in the sample; the particle size ranges from 5 nm to 50 nm (**Figure 30-a-b**). These features cannot be detected by the SEM (resolution of ~2 μm) and is clear that particles at these nano-scale particles are not the original powder (micron scaled), but precipitates of the intermetallic particles. **Figure 30-c** shows some grain boundaries that where not detected by SEM images showed in this section.

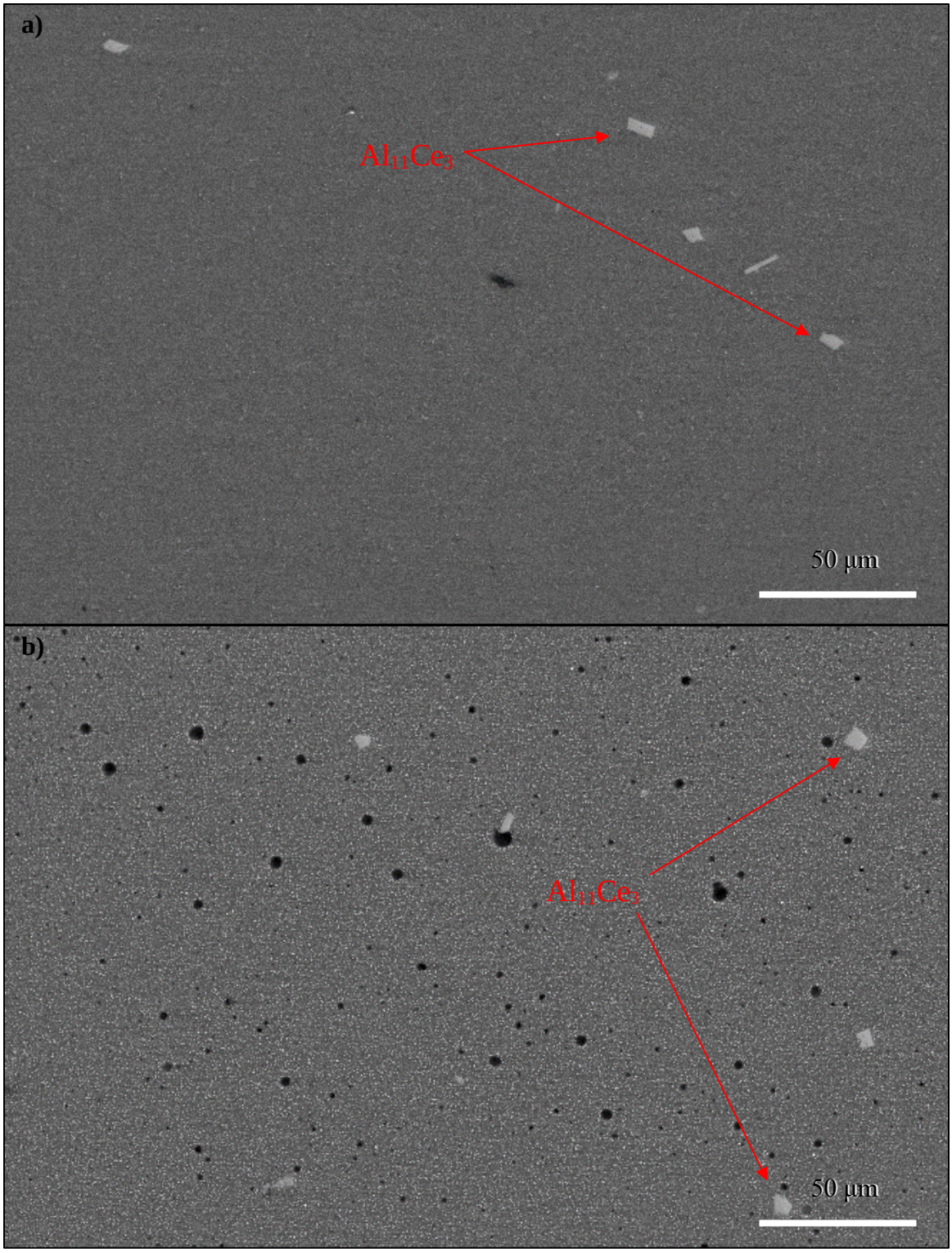

Figure 26. SEM micrograph (transverse cross-section) of a) as-extruded and b) 432 °C - 4.5 hrs.

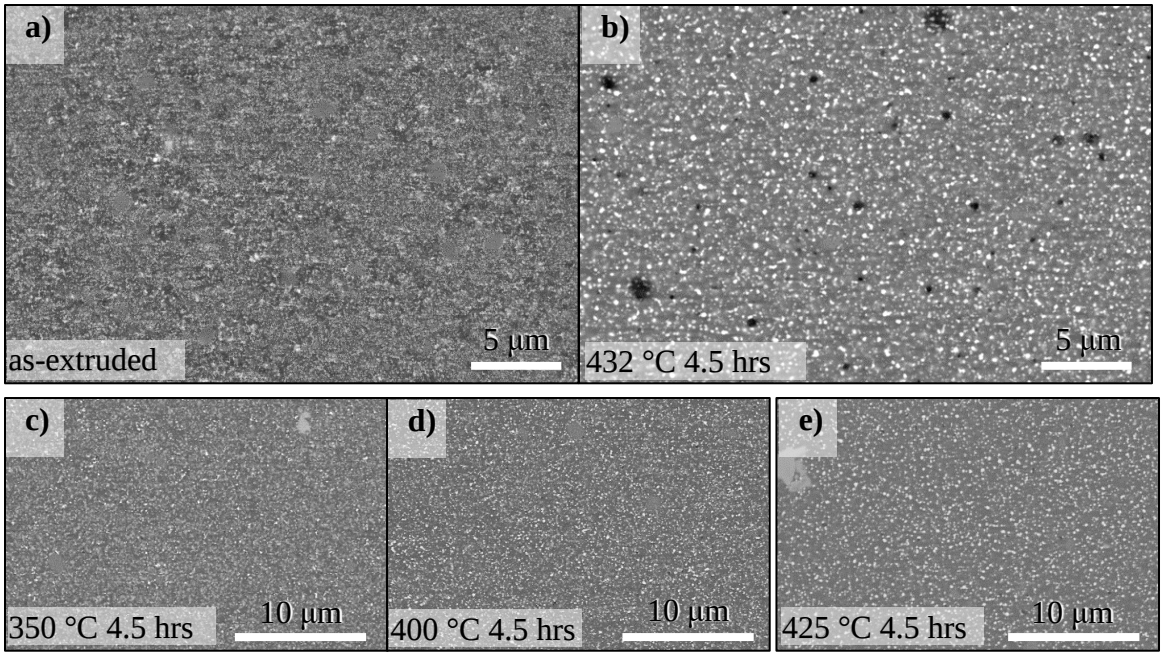

Figure 27. SEM images showing the microstructure evolution with heat treatments of a) as-extruded, b) 432 °C - 4.5 hrs, c) 350 °C - 4.5 hrs, d) 400 °C - 4.5 hrs, and e) 425 °C - 4.5 hrs.

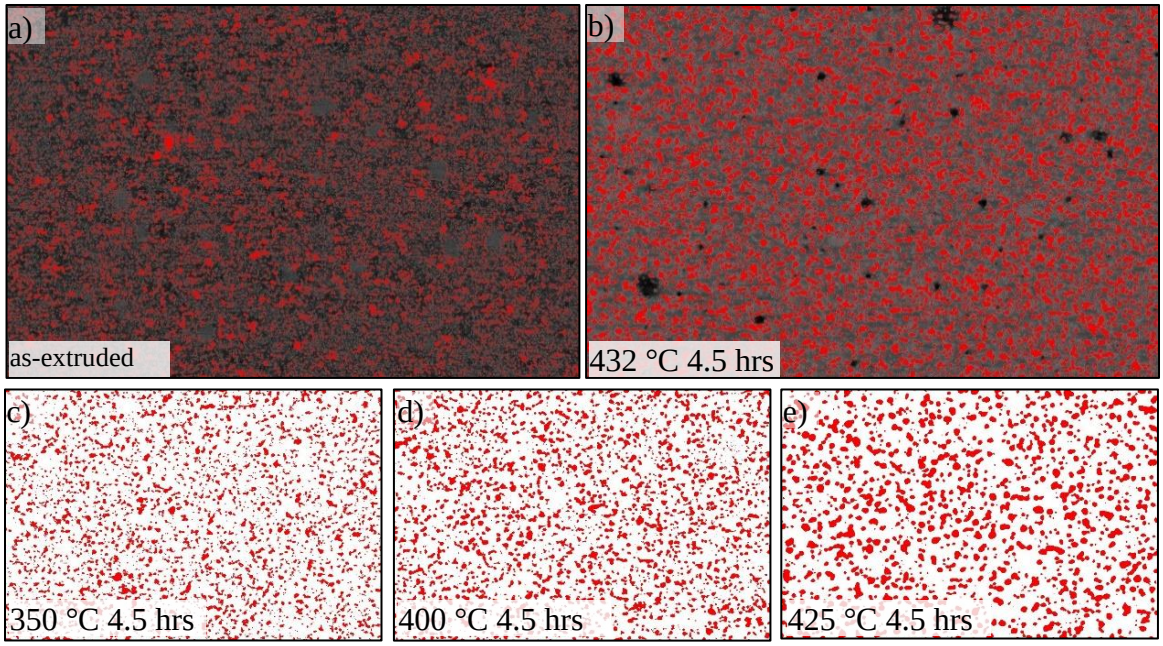

Figure 28. Effect of heat treatment on the size (area) of the intermetallic phase analyzed with ImageJ.

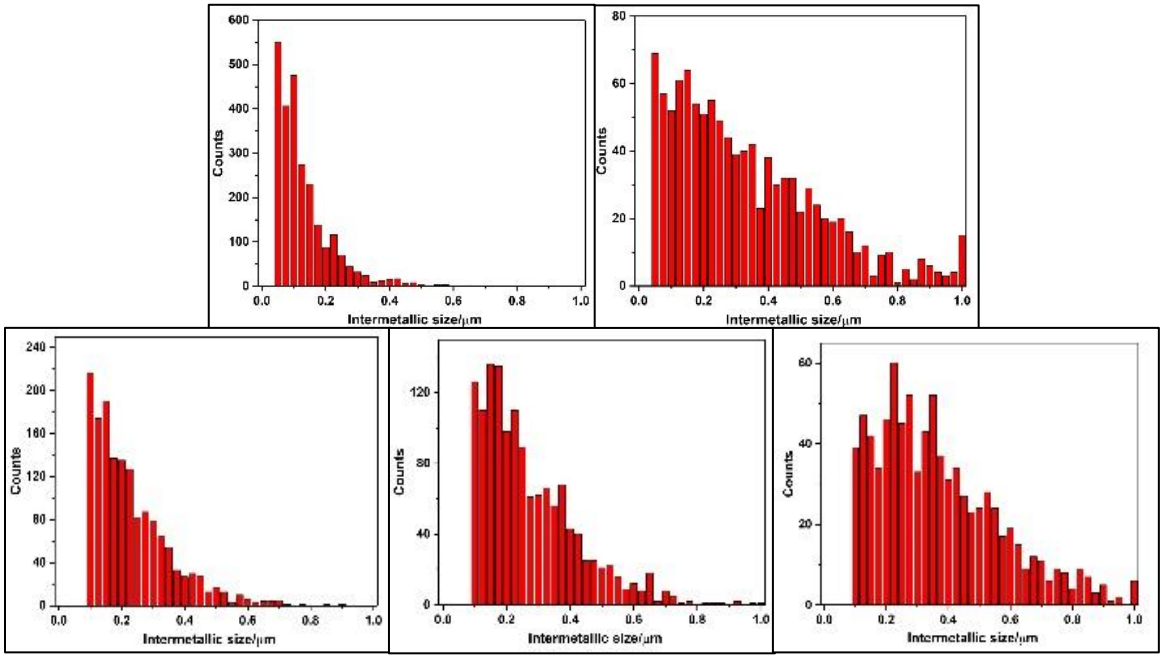

Figure 29. Intermetallic phase size (area) distribution analyzed with ImageJ.

Table 6. Effect of heat treatment on intermetallic particle size and distribution.

Samples	Average diameter (nm)	Distribution (nm)
as-extruded	97	38-521
350 °C - 4.5 hrs	202	97-714
400 °C - 4.5 hrs	276	101-817
425 °C - 4.5 hrs	383	105-998
432 °C - 4.5 hrs	362	48-1000

4.4.3 Summary of Microstructural Analysis

Optical microscopy confirmed that the as-received powder has fine microstructure. The fine scale microstructures were a consequence of rapid solidification. Optical microscopy also showed a fine-scale microstructure after the extrusion. Also, pores were observed on the polished surface of the samples after the heat treatment at 432 °C potentially due to the loss of Mg. SEM/EDS mapping indicated that the phases present in the material are Al solid solution, $Al_{11}Ce_3$, and $Al_{13}CeMg_6$ consistent with the thermodynamic calculation and the XRD. SEM/EDS showed that the larger phases observed after the extrusion could be $Al_{11}Ce_3$.

In the following section, we investigated the intermetallic particle size and distribution and its evolution as a function of the heat treatment temperature using USAXS. We expected that the very low solubility of Ce in Al matrix and the phase stability of $Al_{11}Ce_3$ would significantly hinder the particle coarsening.

4.5 USAXS

The USAXS data modelling was guided by SEM imaged of the as-extruded sample (**Figure 31**), which reveals some powder particles ~ 2 μm (yellow dotted lines) as well as finer, meso-scale phases and even smaller nano-scale phases on the order of 10 nm. The micron-sized powder particles are expected to scatter at the lowest q-ranges around 10^{-4} $Å^{-1}$, and are not going to be taken into account for the purposes of doing an assessment of intermetallic particles size distribution after heat treatment, because they are the grain boundary some original powder particles. Only the meso-scale and nanoscale intermetallic particles present in the optical, SEM, and TEM images are going to be used for the quantification of the evolution of intermetallic particles size after heat treatment.

To a first approximation, these phases are treated as simple spheres to understand how the precipitates evolve with temperature. In reality, they are not perfectly symmetric and have some anisotropy, which will broaden the Guinier region and smooth the Bessel function oscillations in the Porod region. This Guinier broadening is accounted for in the model by broadening of the size distribution. In this study, the meso-scale and nanoscale phases are important, in terms of mechanical performance especially after thermal exposure,

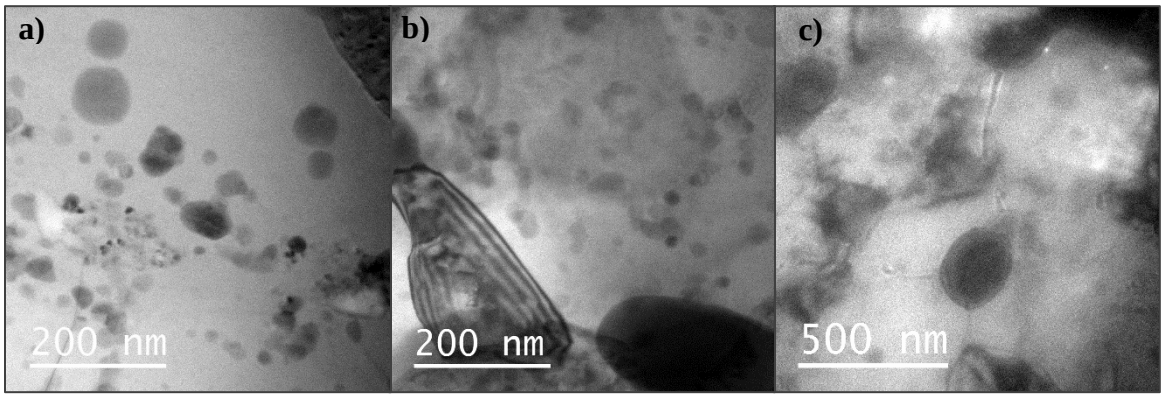

Figure 30. TEM bright field and dark field of 432 °C - 4.5 hrs.

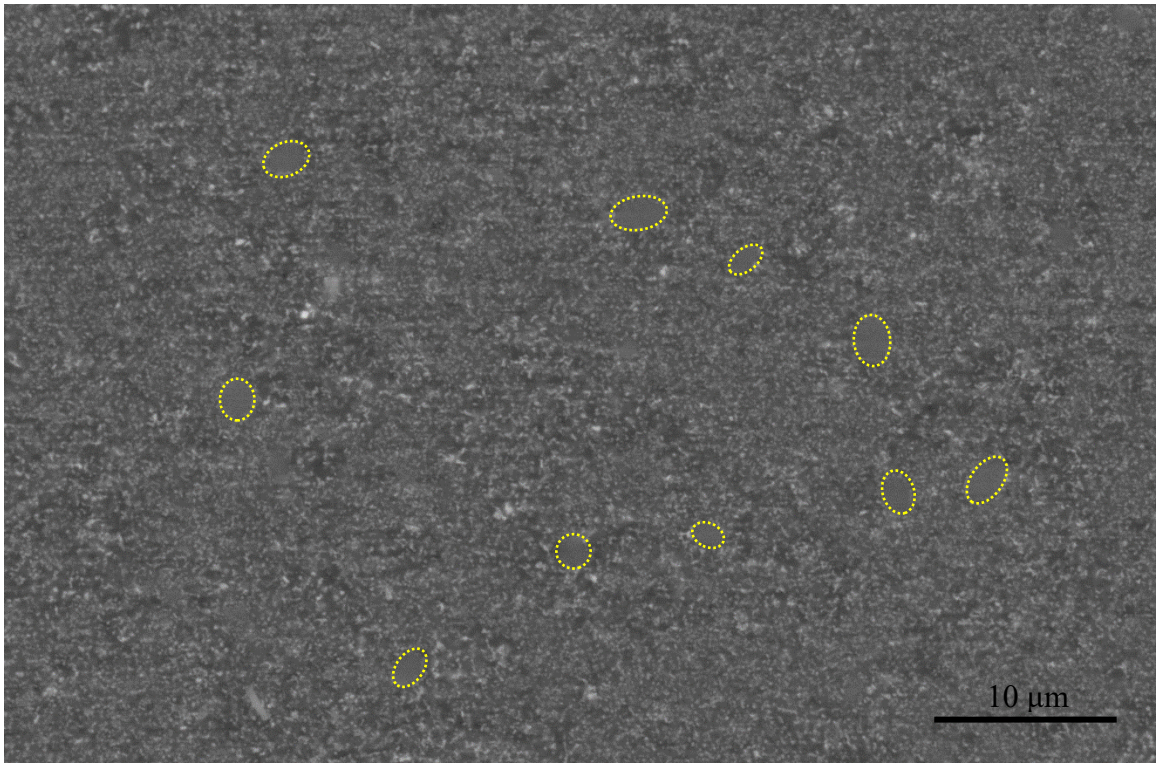

Figure 31. SEM image of an as-extruded sample showing micron-sized powder particles in yellow dashed lines and smaller, meso-scale phases.

while the larger powder particles are not. Therefore, a bi-modal size distribution of spherical phases is used here to extract both the full-size distributions, as well as the mean sizes of each mode by using the following equations:

$$I_{smr}(q) = \int_0^{q_{slit}} I_{model}(q)dq \quad \textbf{Eq. 1}$$

$$\boldsymbol{I_{model}(q) = I_D(q, \bar{R}_1, \sigma_1, v_1) + I_D(q, \bar{R}_2, \sigma_2, v_2) Bq^{-4} + b} \quad \textbf{Eq. 2}$$

$$I_D(q, \bar{R}, \sigma, v) = v[\Delta\rho]^2 \sum P_v(R, \bar{R}, \sigma)[F(q,R)]^2 V(R)\Delta R \quad \textbf{Eq. 3}$$

Where the first three terms in **Eq. 2** represent the nano, meso and micron-scale phases in the sample, respectively. As no clear Guinier region from the micron-scale phases can be observed, the Porod scattering from these phases fits the data by varying only the Porod scaling factor, *B*. Each of the nano and mesoscale populations are modeled as a Guassian probability size distribution, *Pv*, which is described by a mean and standard deviation. The size distribution, *Pv*, is a volume distribution multiplied by the square of the formfactor for a sphere of radius, *R*, and its volume, *V*. In **Eq. 3**, the intensity is scaled by the volume fraction, v, and contrast-squared, $\Delta\rho$, of the respected phase. To extract meaningful values for v_1 and v_2, the scattering contrast for $Al_{11}Ce_3$ in Al was calculated using the Irena package and used in **Eq. 3**. Finally, the model was slit-smeared in **Eq. 1**, using q_{slit} = 0.23 Å^{-1}, to fit the data. A total of 8 parameters were fit to the USAXS data in the q-range: 0.0004 Å^{-1} < q < 0.2 Å^{-1}, using the Irena package for Igor pro.

The modeling results are shown in **Figure 32** and **Figure 33**. **Figure 32-a** shows log-log plots of I_{smr} vs q for the as-extruded and heat-treated samples. The size distributions obtained from the model fitting of **Eq. 1** are shown in **Figure 32-b**, the diameter range highlights the change in the meso-scale phases. **Figure 33-a** shows log-log plots of I_{smr} vs q. The mean radius for meso-scale size distribution, obtained from the model fitting of **Eq. 1**, are shown in **Figure 33-a**.

Nanostructured materials are susceptible to thermally induced grain coarsening. There is a relation between increase in microhardness because of intermetallic particle size decreasing [**64**]. In this research by using USAXS we determined an intermetallic particle coarsening

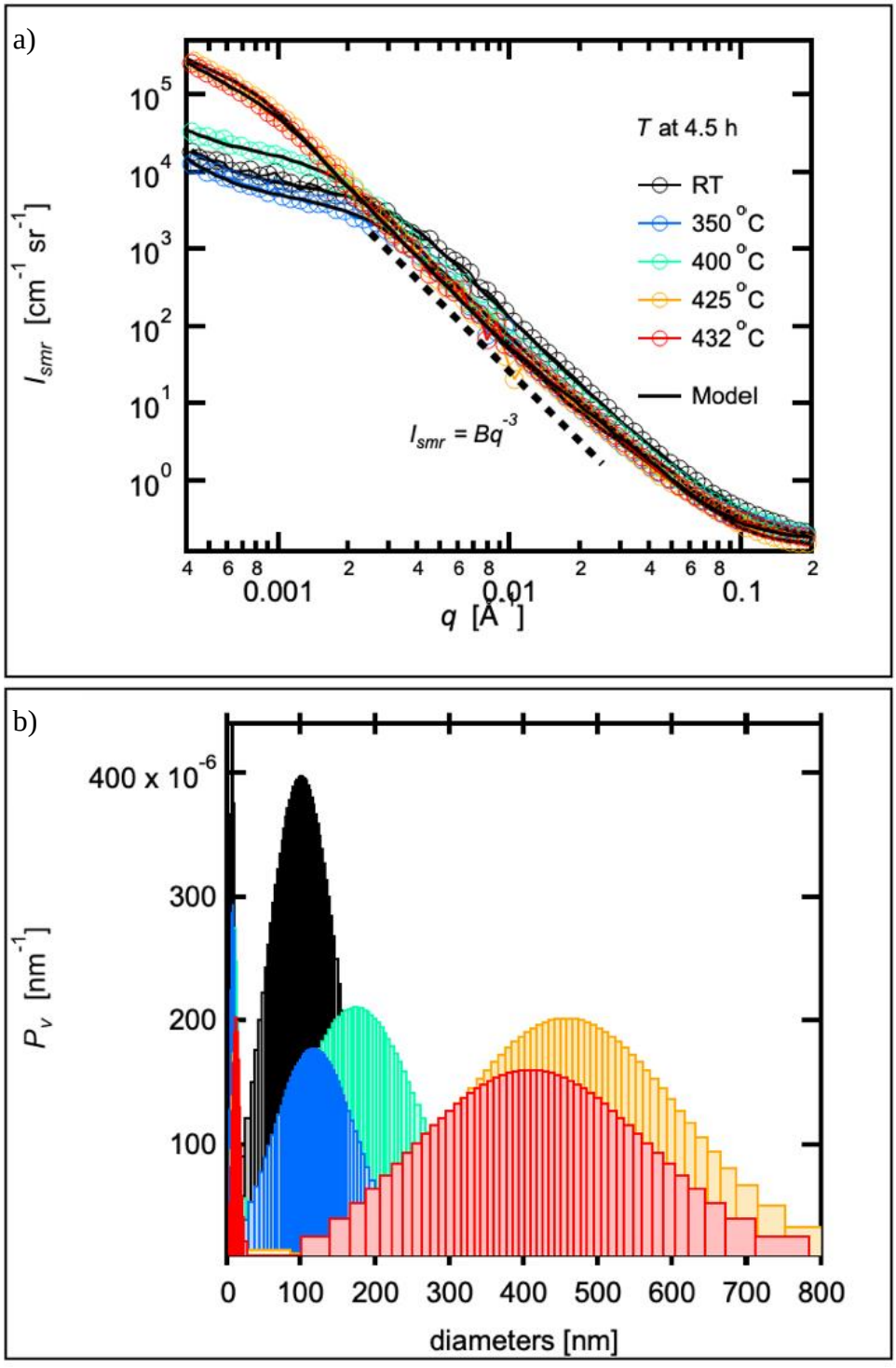

Figure 32. a) Log-log plots of I_{smr} vs q. b) particle size distributions

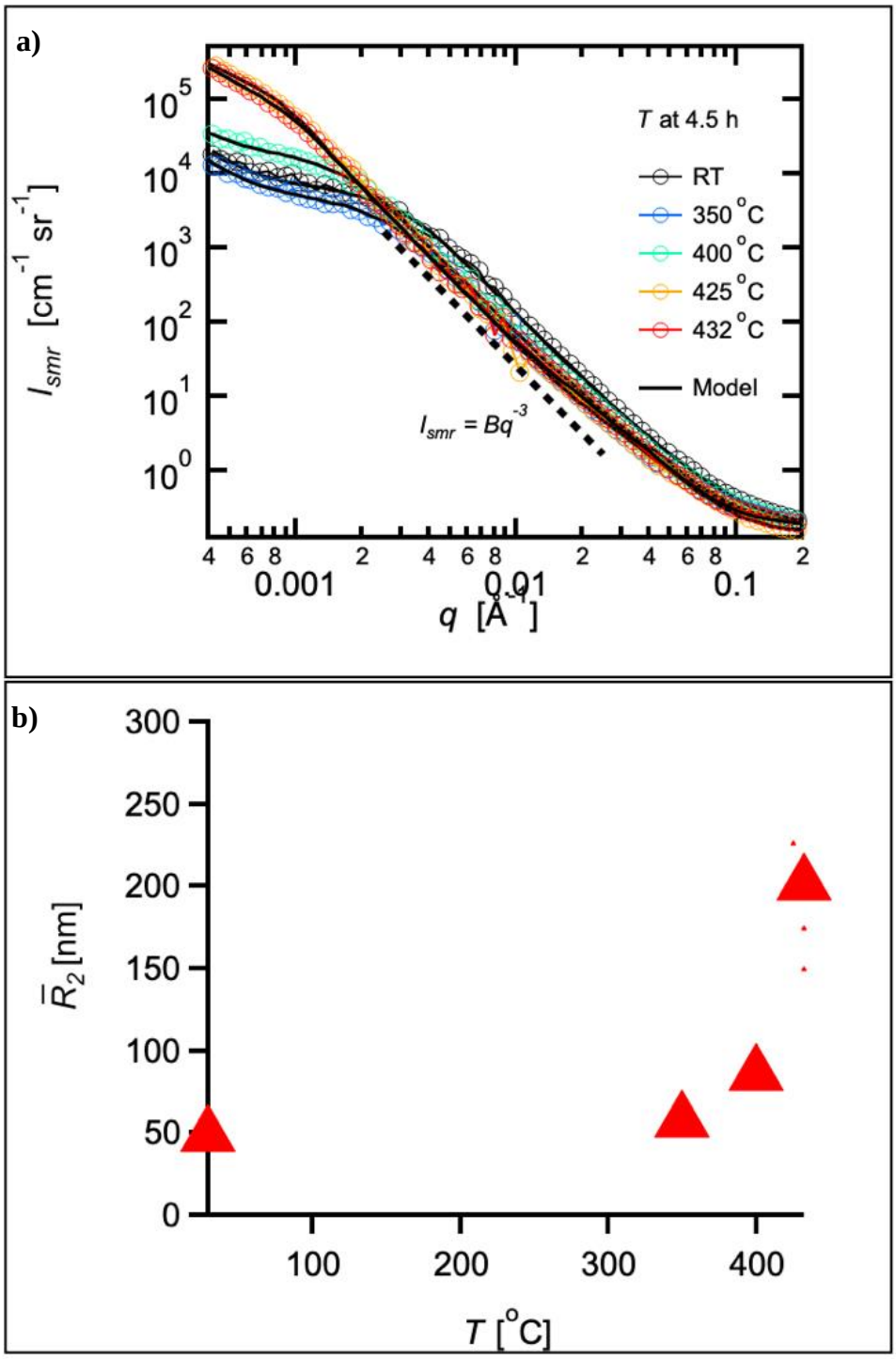

Figure 33. a) Log-log plots of I_{smr} vs q. b) Mean radius for meso-scale size distribution.

increase with temperature and time exposure. The average particle size of as-extruded samples was found to be ~101 nm and the heat treatment condition that presented the largest average size particle was 425 °C - 4.5 hrs, about 462 nm (**Table 7**). This coarsening is not at all significant compared to other nanoscaled materials. It has been reported on Al-3Mg (wt. %), after thermal exposure of 1 hour at 300 °C intermetallic particle size coarsens from 90 nm to 10 μm - 15 μm range, an in consequence there was a reduction in hardness from ~184 to ~56 HV scale [**65**].

4.5.1 Summary USAXS

The SAX analysis results are comparative to the average size and distribution obtained from the ImageJ analysis of the micrographs, in the sense that particles of nanoscaled size and the evolution of the particles size with temperature could be identified by Image J as well as USAXS (**Figure 34**). In the next section, the microhardness test results will be presented, and the results will be correlated to the intermetallic particle coarsening data from the USAXS. It is expected that the microstructural coarsening will be correlated to the decrease in microhardness, but we also expect minimal loss of microhardness.

4.6 Mechanical Properties

4.6.1 Microhardness

The equipment utilized for micro-indentation tests has the capabilities of doing fast speed nano-indentation test in an array, and the results could be utilized to create a harness map of the surface of the material. In our research we tried, unsuccessfully, to create a hardness map that could be correlated to the phases present. This was due to the ultra-fine features of the samples, and the hardness map obtained was a very even one because most indentation results of hardness are very close in value. The insight of these results is that the surface hardness of the material at the micro level is mostly due to the fine microstructure.

Microindentation test was performed at a total of twenty-five tests per sample. Not all tests were successful, therefore for some samples, less than twenty-five test results (load vs depth) were used to calculate hardness in the Vickers's scale. On **Figure 35,** all the 25 tests

Table 7. USAXS results summary of intermetallic particle average size and distribution.

Samples	Average (nm)	Distribution (nm)
as-extruded	101	17-184
350 °C - 4.5 hrs	117	3-231
400 °C - 4.5 hrs	176	1-351
425 °C - 4.5 hrs	462	1-800
432 °C - 4.5 hrs	413	10-790

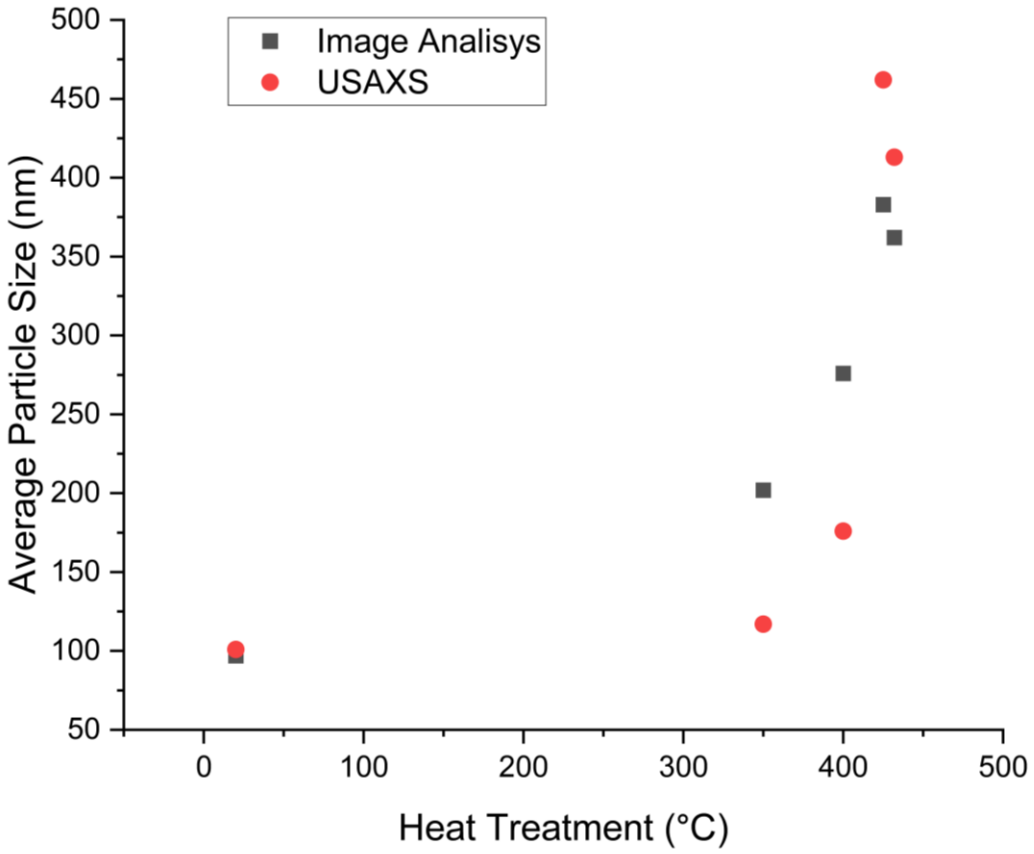

Figure 34. Average intermetallic particle size as a function of the heat treatment temperature.

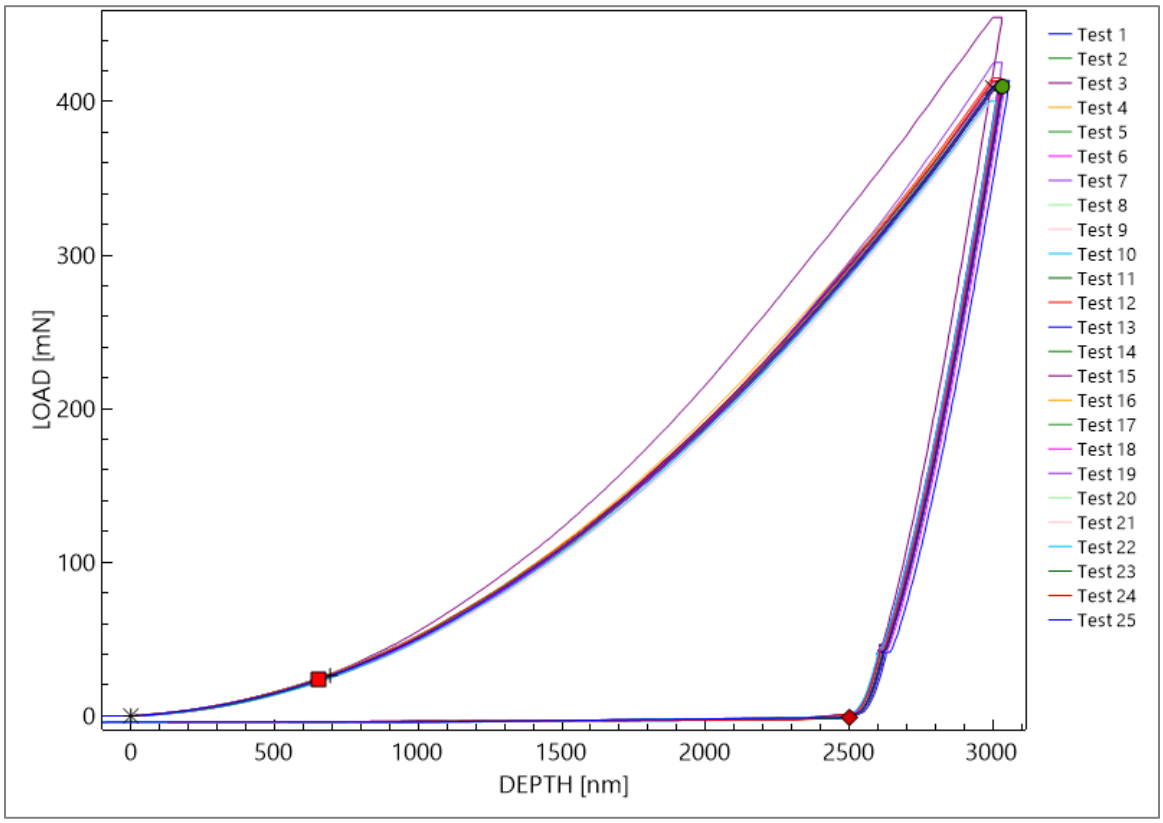

Figure 35. Microhardness test as-extruded.

of the as-extruded sample were successful, and the applied force did not went beyond 460 mN. This sample shows the highest hardness value at 237 (8.5) HV of the entire set. On **Figure 36** is the set of tests for the 350 °C - 4.5 hrs condition. All 25 tests were successful, and the average harness value was calculated as 228 (7.3) HV. For the 400 °C - 4.5 hrs, 23 tests are recorded, and the largest load applied was about 350 mN, the calculated harness value was 207 (6.3) HV (**Figure 37)**. Interestingly, for the 425 °C - 4.5 hrs condition only 12 tests were successfully performed, and the applied force did not went over 370 mN (**Figure 38**). The loss of hardness after heat treatment was not significant compared to 400 °C, at 208 (6.6) HV. For the 432 °C - 4.5 hrs sample all 25 tests were recorded and the maximum applied force was about 360 mN with a test with an applied force allow as 280 mN, and the hardness value was calculated as 200 (11.9) **(Figure 39**).

There is a clear trend of losing HV value with temperature exposure. The results show a downward pattern in hardness with heat treatment temperature, and that hardness is constant with depth. This result confirms that the hardness feature is not due to superficial incident (like oxidation), but a sample feature. The summary of hardness values is plotted in **Figure 40**.

The effects of heat treatment temperature on microhardness and intermetallic particle size are evident in **Figure 41**. There is a trend of losing harness value and coarsening of the intermetallics with temperature exposure. This loss of hardness is not significant, after heat treatment the hardness values, for 350 °C – 4.5 hrs, are higher and the coarsening minimum compared with nanoscaled conventional aluminum alloy Al-2017 after thermal exposure at 300 °C for 1 hour as shown in **Figure 42** [**66**]. $Al_{11}Ce_3$ is thermodynamically stable, and the near-zero solubility of Ce in Al creates a physical barrier that impedes coarsening.

Microhardness is related to particle size by the relation where larger particles will yield lower microhardness. The relation microhardness (HV) to particle size is described by the equation $H_v=H_0 + k_H d^{-1/2}$, where H_v is Vickers microhardness, d is particle size in μm, and H_0 and k_H are constants that are related to the material. The expectation when a material behaves following this relation, is for the slop in the Vickers hardness test vs $d^{-1/2}$ to be positive. **Figure 43** shows this plot of changes in microhardness (HV) in terms of particle size. There is a trend to follow the expected positive linear relation, using the intermetallic

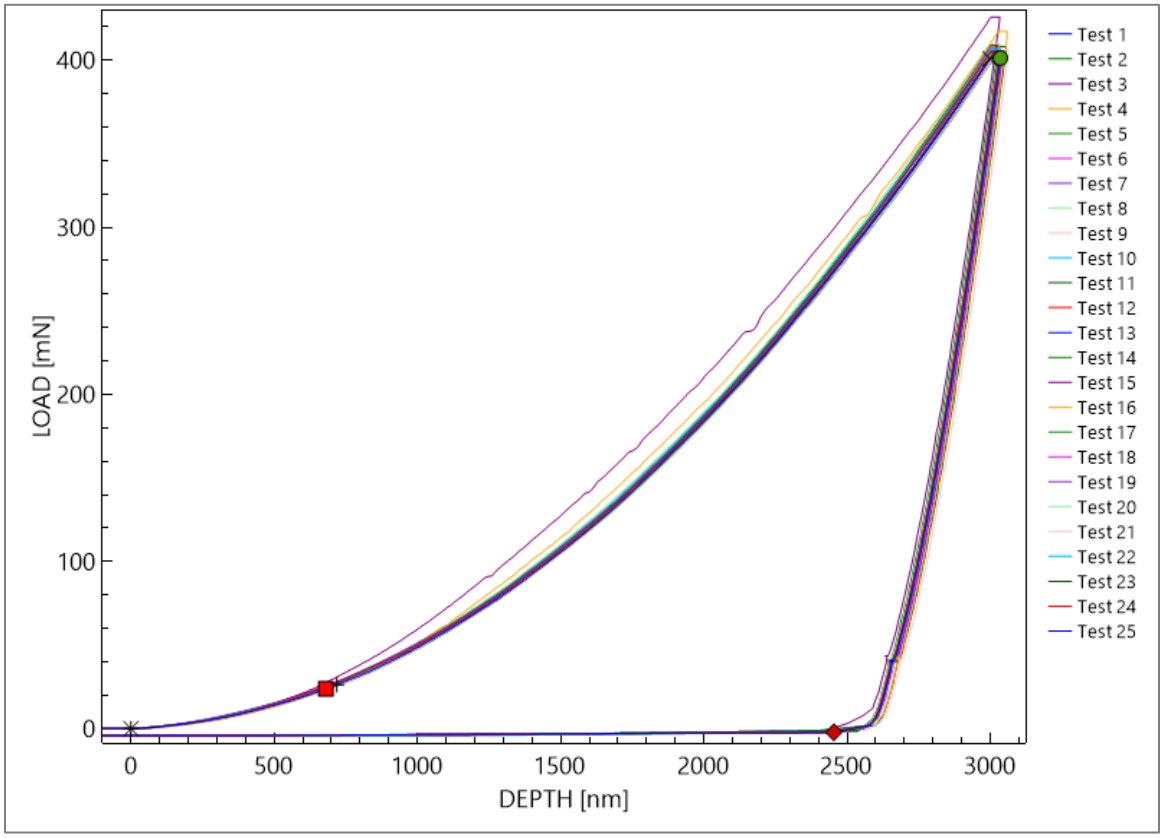

Figure 36. Microhardness test (load vs depth) 350 °C - 4.5 hrs.

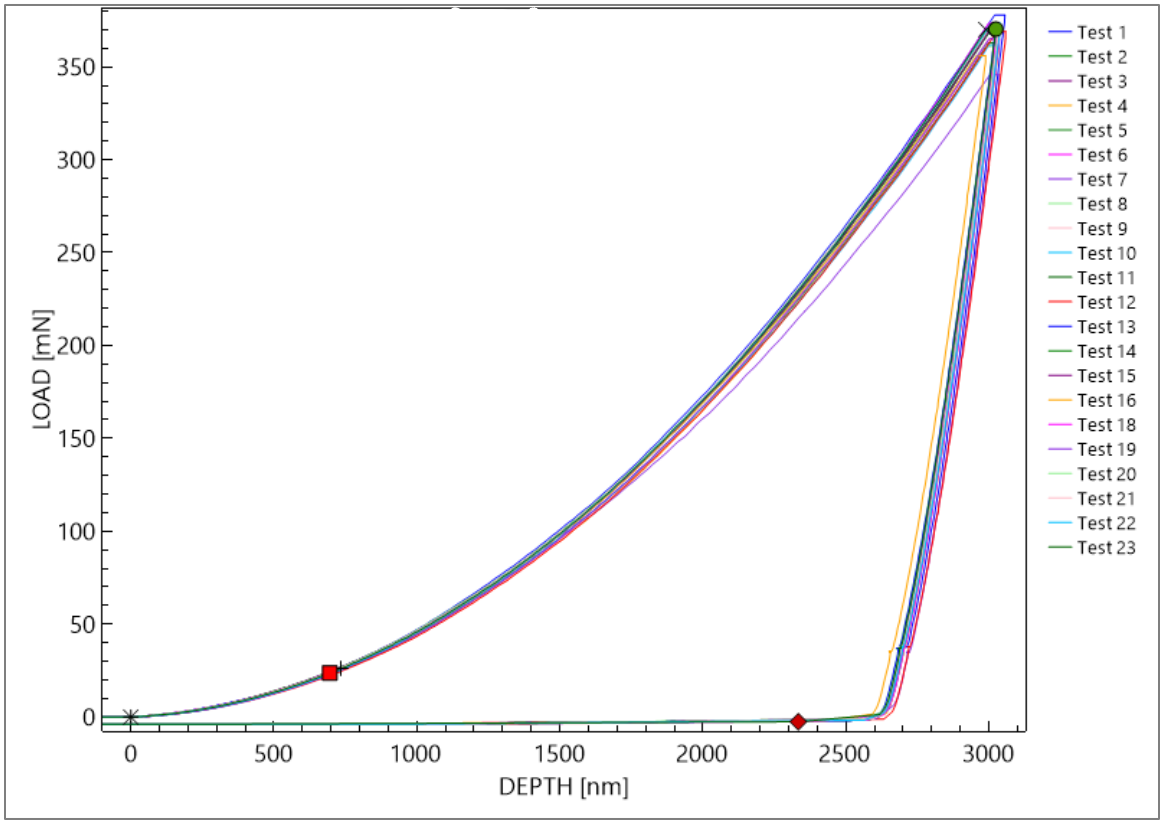

Figure 37. Microhardness test load vs depth 400 °C - 4.5 hrs.

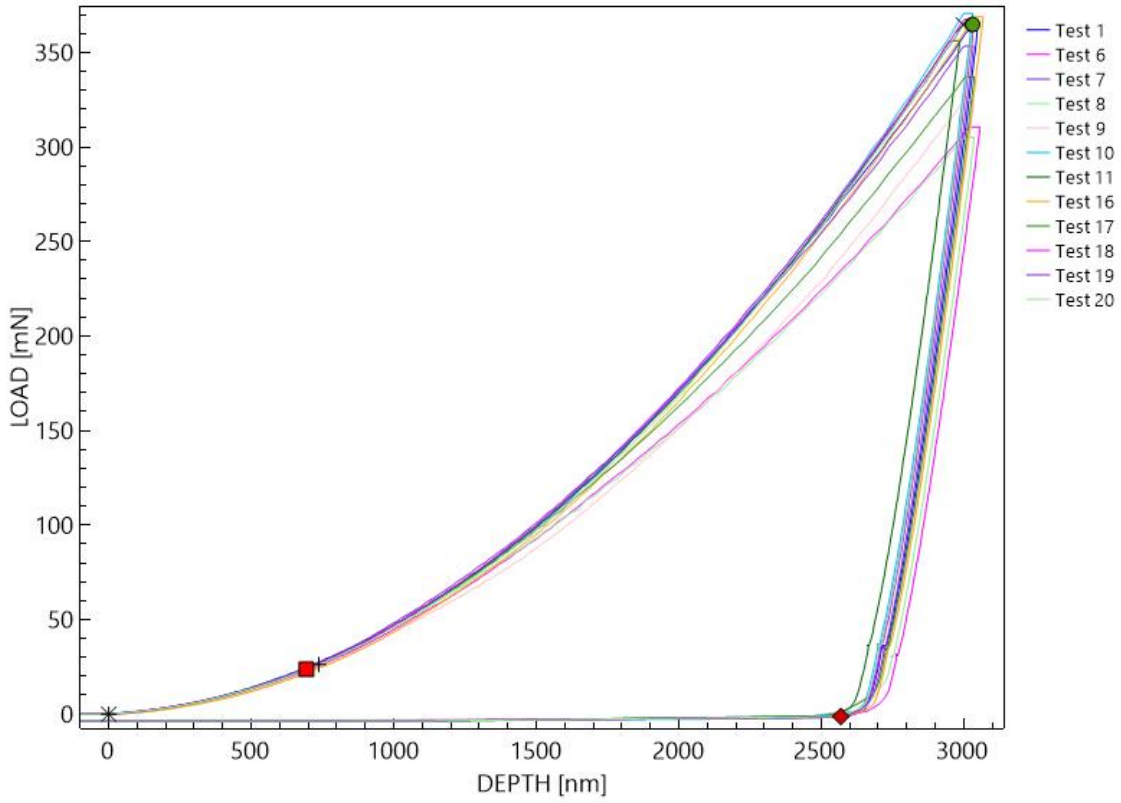

Figure 38. Microhardness 425 °C - 4.5 hrs.

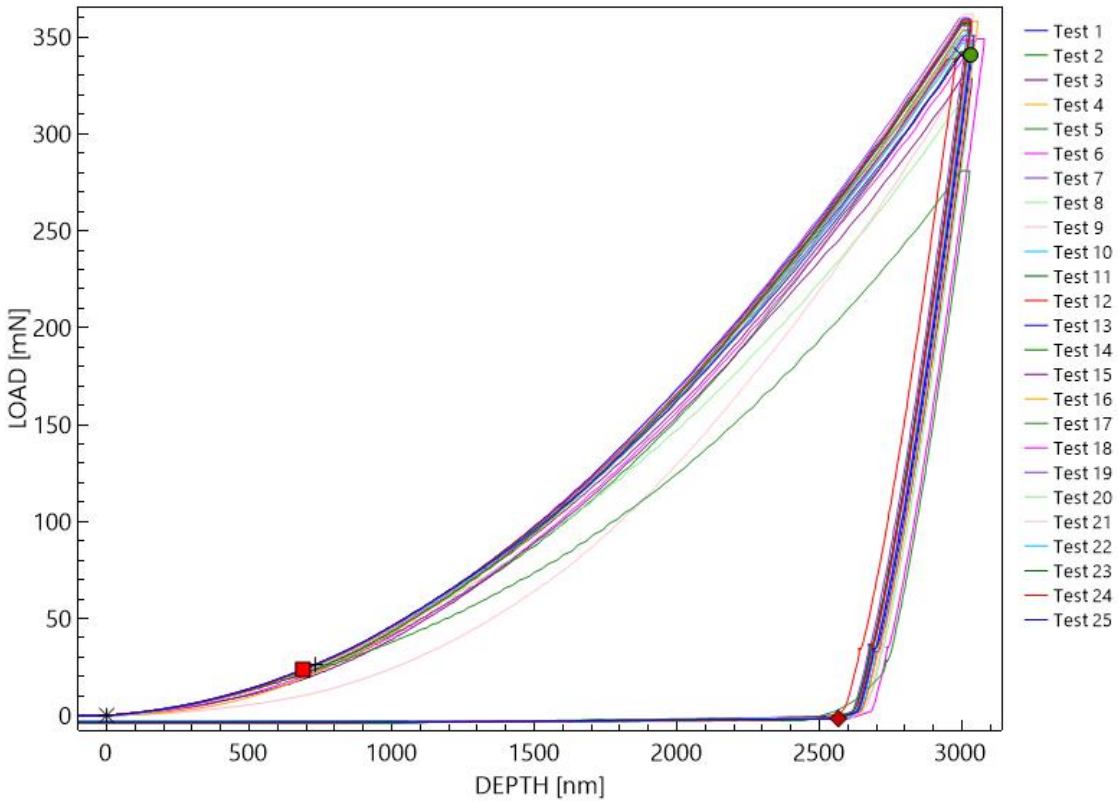

Figure 39. Microhardness test 432 °C - 4.5 hrs.

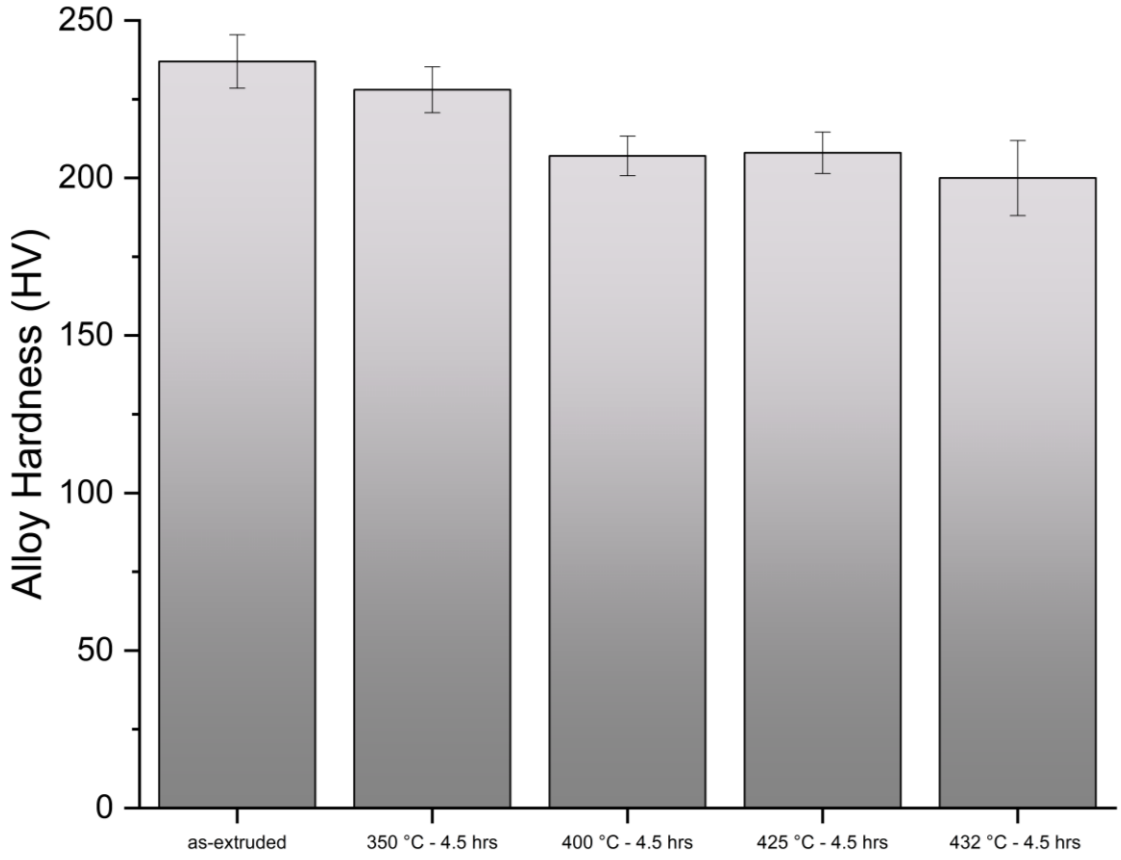

Figure 40. Average values of microhardness per heat treatment condition.

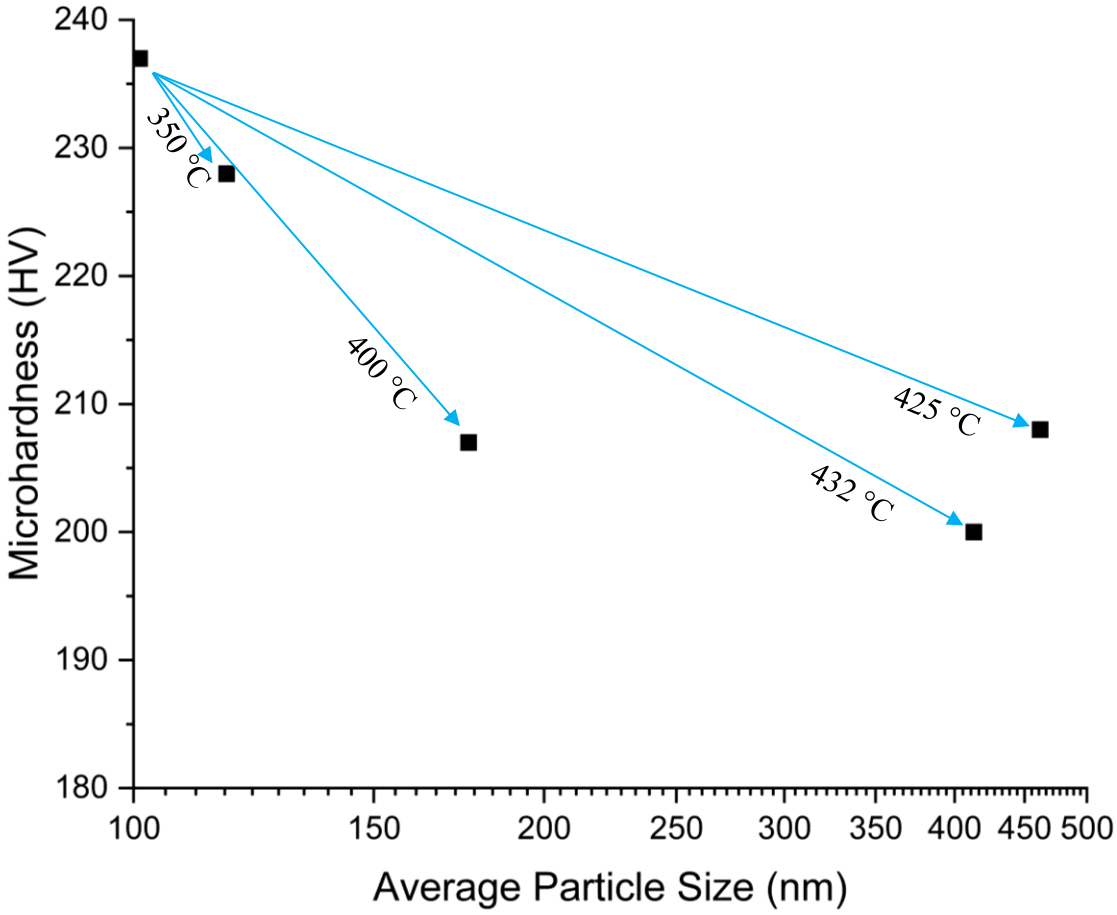

Figure 41. Effect of particle size (from USAXS) on microhardness.

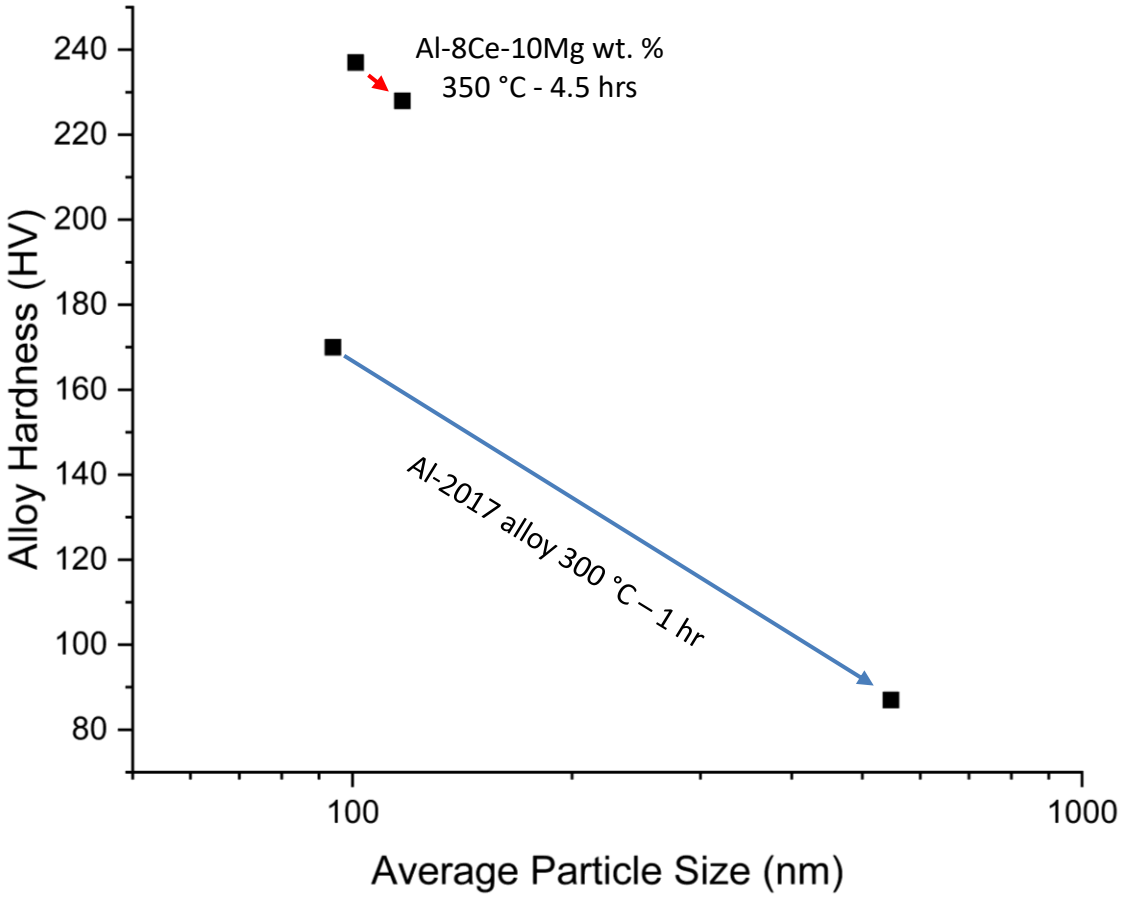

Figure 42. Vickers hardness (HV) vs particle size average (nm) [66].

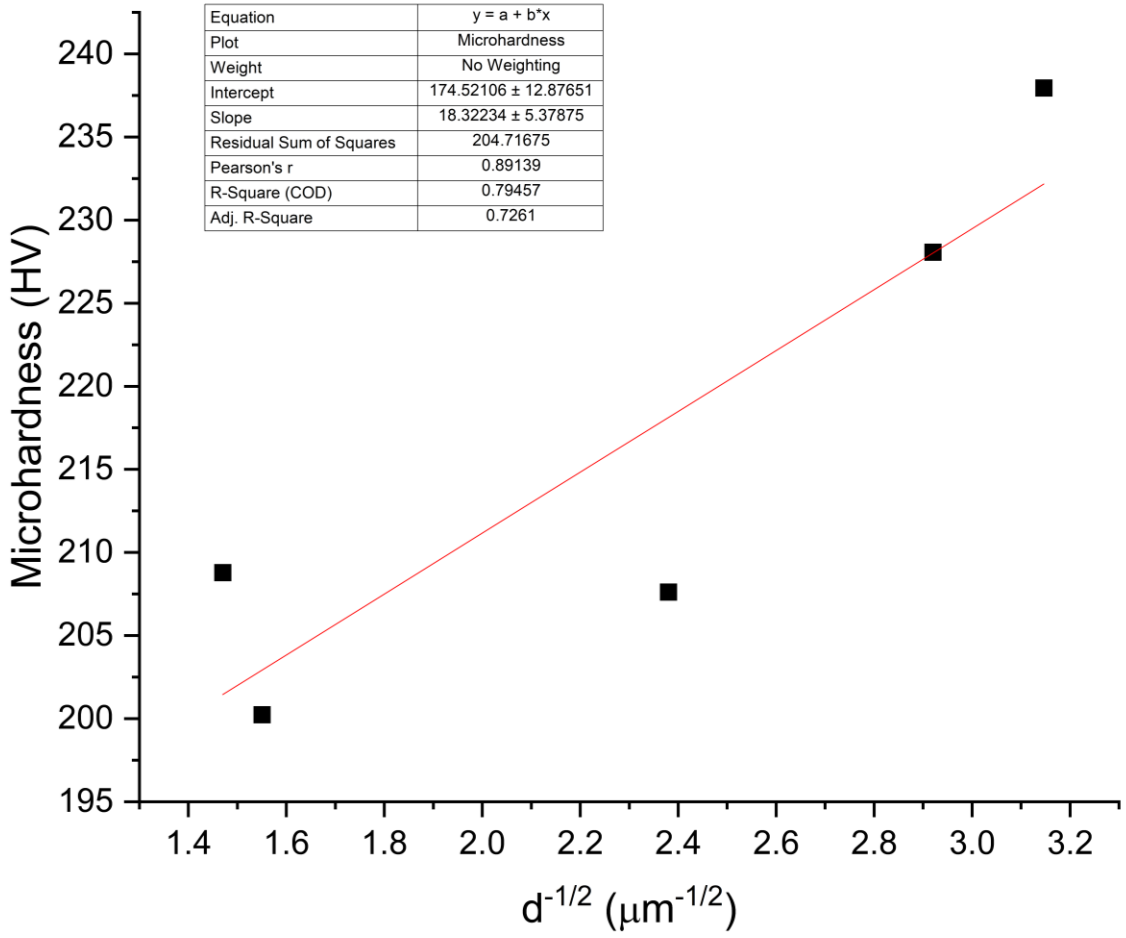

Figure 43. Vickers Hardness changes with intermetallic particle size.

particle size obtained from USAXS.

4.6.1 Tensile Test

Average UTS of the as-extruded is 687 (6.8) MPa. After heat treatment at 350 °C for 4.5 hours the UTS average is 607 (9.1) MPa. For the samples 400 °C – 4.5 hrs the average UTS 601 (16.5) MPa, this is a hardness retention of 87%. The average values of UTS for the samples heat treated at 425 and 432 °C are very similar at 544.65 (6.5) and 546 (7.5) MPa respectively.

Enhanced elongation is related to temperature exposure (**Figure 44**). These results strongly demonstrate that after heat treatment at 350 °C - 4.5 hrs the material becomes slightly more brittle (0.64 % elongation) and a small improvement in elongation at 400 °C - 4.5 hrs (2.82 %). Moreover, there is an even larger improvement in elongation at 425 °C - 4.5 hrs and 432 °C - 4.5 hrs of 9.71 % and 9.22 % respectively.

Ultimate tensile strength (UTS) of the as-extruded samples is significantly higher (687.22 MPa) compared to casted Al-8Ce-10Mg wt. % (228 MPa, %E = 1, density 2.49 g/cm^3) [**9**]. For visual comparison we plotted representative examples of each condition on **Figure 45**. Average tensile properties are detailed in **Figure 46**.

Al-8Ce-10Mg is proposed as a candite to replace commonly used structural alloys. Specific strength (using experimental density of 2.72 (0.00485) g/cm^3) vs elongation plot shows the material to have higher performance (UTS/density) than cast iron, Al alloys, Mg alloys, and Ti alloys (**Figure 47**). Also, after heat treatment the material recovered elongation at higher values than Al and some cast iron alloys.

4.6.2 Fractography

We used as-extruded and 432 °C - 4.5 hrs case to analyze the fracture surfaces of the tensile testing samples. In **Figure 48** as-extruded fracture tensile sample (labeled **a**) shows very little necking, and the fracture surface is perpendicular to the tensile loading direction. This brittle fracture surface is consistent with the low ductility observed. In contrast, 432 °C - 4.5 hrs sample (labeled **b**) shows necking and cup-and-cone fracture surface, which is characteristic of a ductile fracture. In **Figure 49-a** of the as-extruded condition, the crack

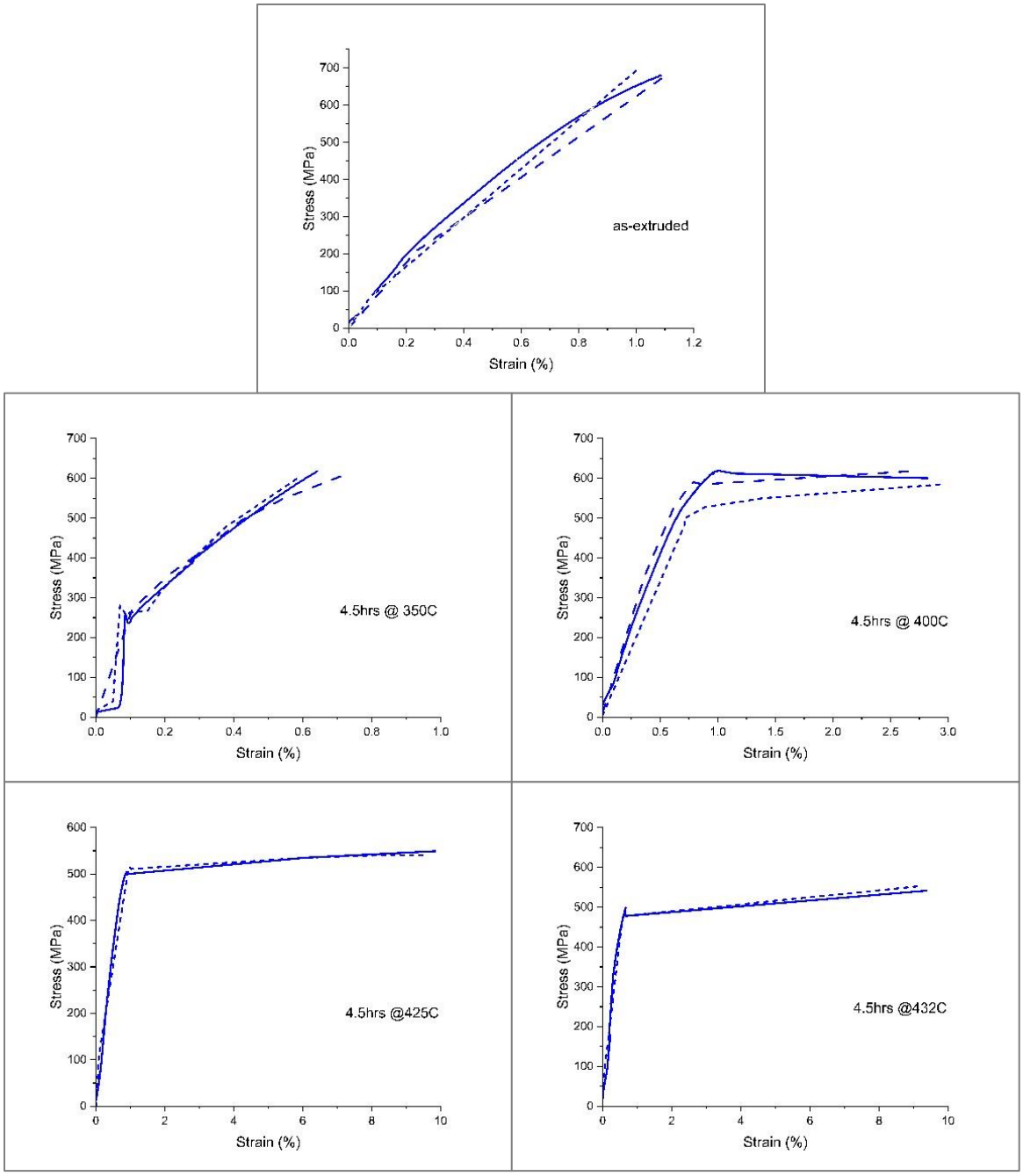

Figure 44. Tensile test plot of Stress vs. Strain.

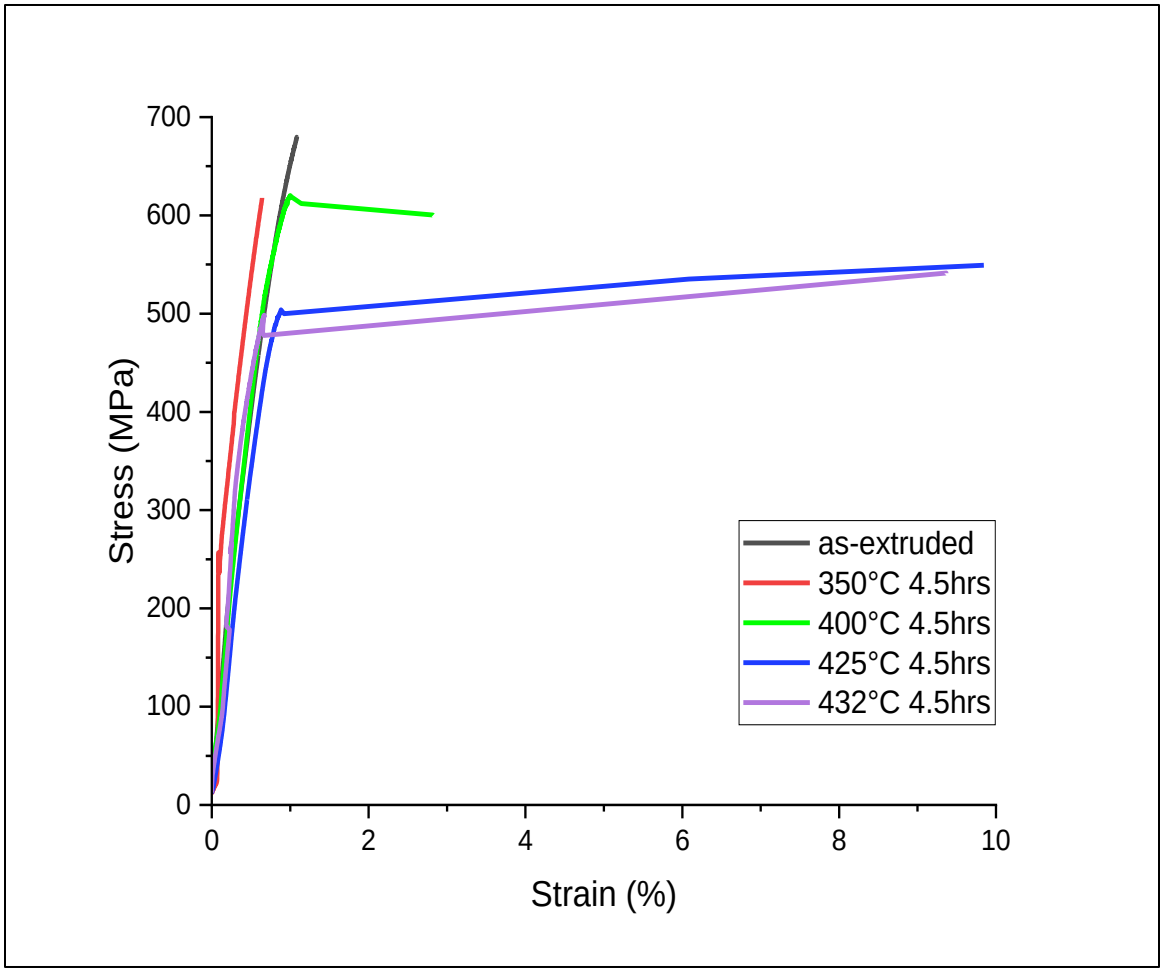

Figure 45. Tensile test results (stress vs strain) comparison after different heat treatment conditions.

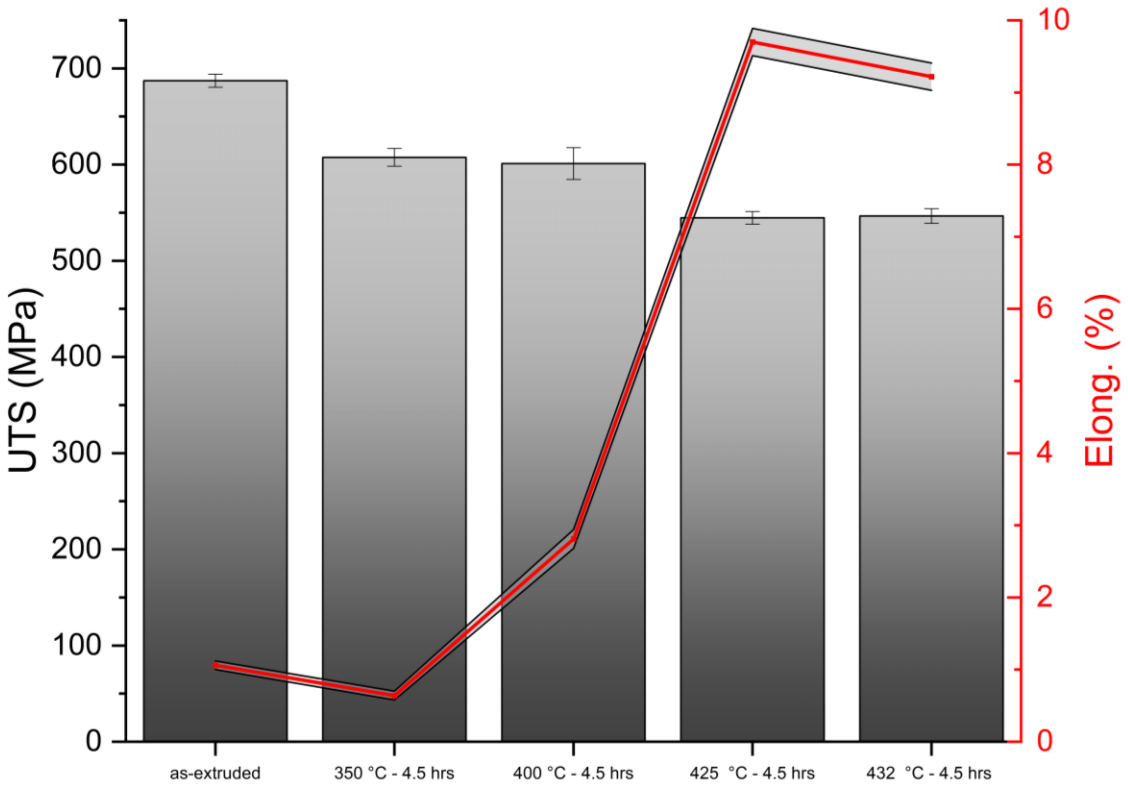

Figure 46. Tensile test average results for UTS (MPa) and elongation (%) of as-extruded and heat treatment conditions.

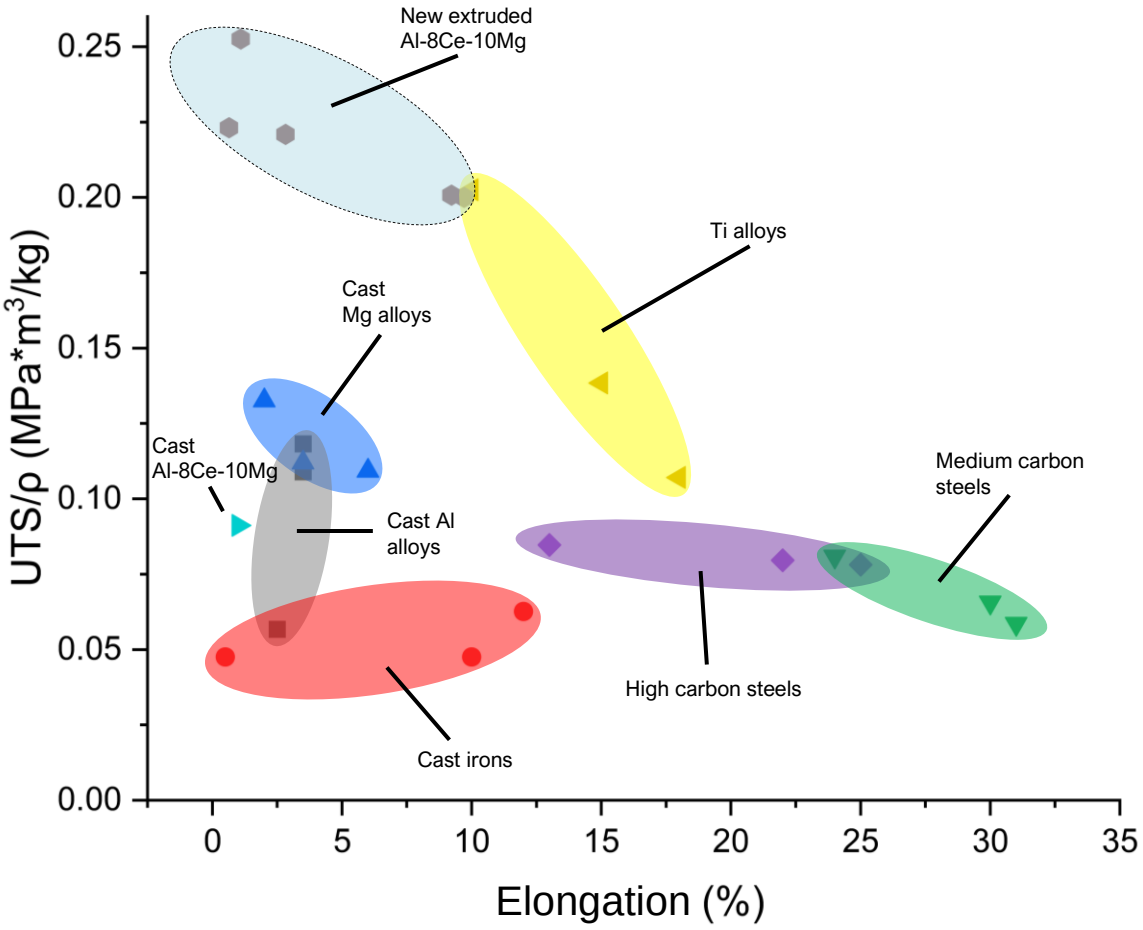

Figure 47. Specific strength vs elongation [1, 9, 67-72].

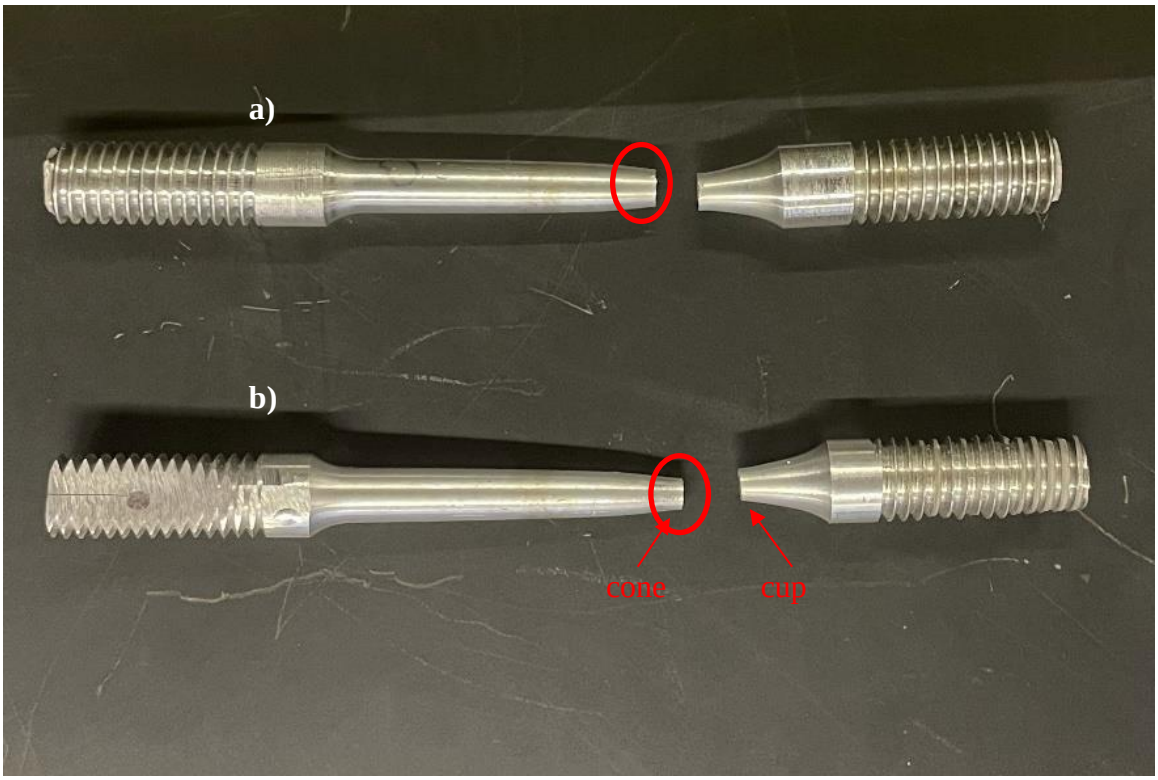

Figure 48. Fracture tensile samples a) as-extruded, b) 432 °C - 4.5 hrs.

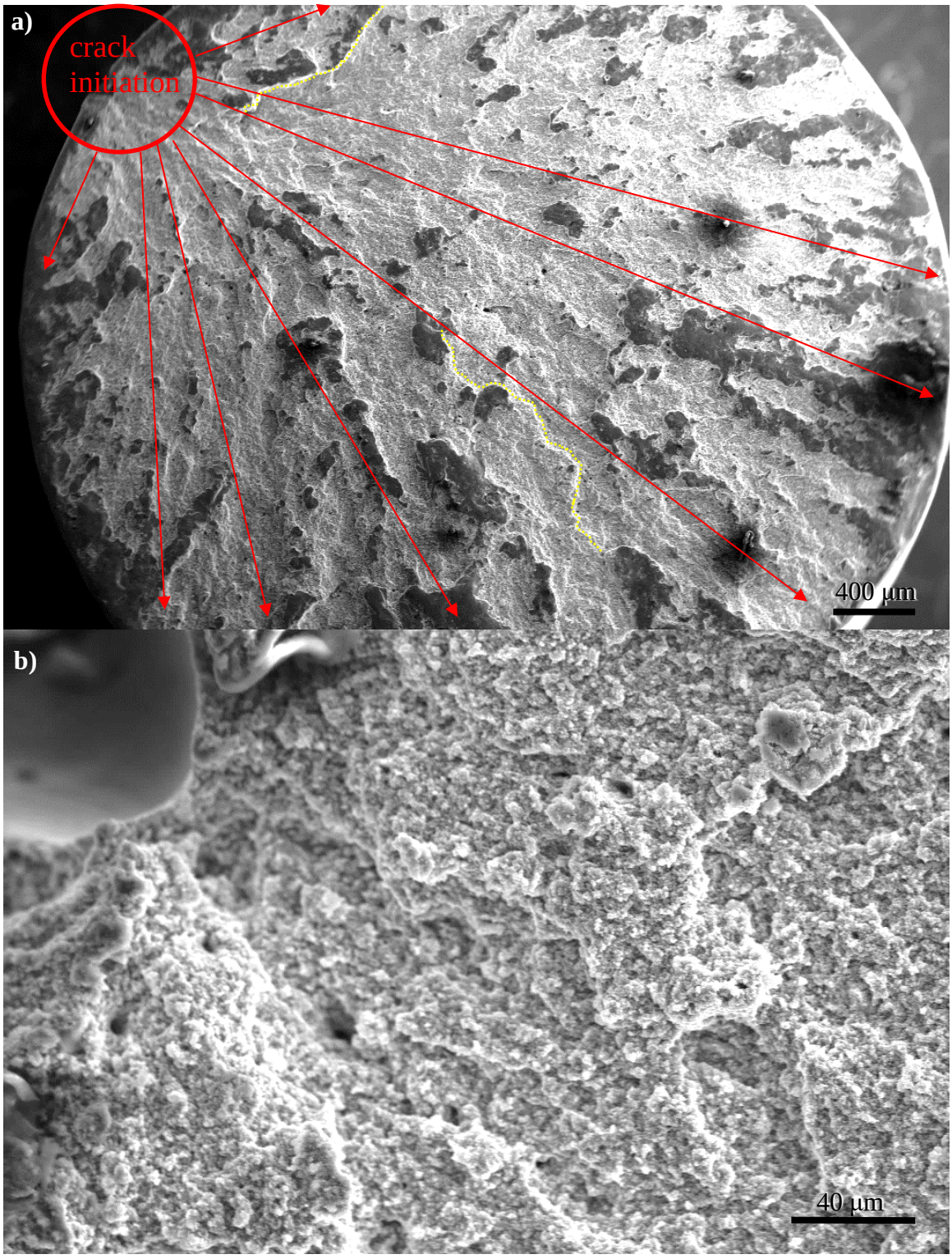

Figure 49. SEM image of fracture surface of as-extruded sample.

initiation area was identified by a red circle. The arrows indicate the general direction of the crack propagation. The yellow dotted lines show trans-granular crack propagation. These characteristics are consistent with the brittle fracture and rapid crack propagation. **Figure 49-b** is a more detailed view of inter-granular cracking.

On the other hand, the SEM image on the cone side of the 432 °C - 4.5 hrs sample (**Figure 50-a**) shows the void nucleation at the center of the tensile sample, where the crack propagation starts, propagates radially, and eventually fractures in a brittle manner (yellow dotted lines) in the outward direction (red arrows) creating the cone and cup shape. **Figure 50-b** shows an area at the center of the specimen, where void nucleation occurred. This type of fracture, during the tensile uniaxial load testing, is consistent with the behavior of a moderately ductile material where void initiation occurs at the center, and void propagation and crack initiation occur perpendicular to the applied force. The cracks propagate in a shear plane creating a cup and cone shape at fracture.

Multiple fractographic observations have been recorded during tensile tests on Al-Ce alloys, considering variations in Ce content and manufacturing techniques. Notably, when conducting tensile tests on as-cast Al-Ce alloys, the fracture surface of Al-9Ce (wt. %) exhibited a flat appearance with noticeable dimpling, which suggests the presence of ductile damage. Interestingly, the orientation of these dimples was found to align with the initial dendritic growth pattern (**Figure 51**) [**46**].

In our samples the fine microstructure cannot allow us to determine dendritic grow direction, as seen in the powder before extrusion dendritic grow is confined to each powder particle. Also, the brittle nature of as-extruded condition can be related to the powder extrusion process and is typical and expected. The gained ductility of 432 °C - 4.5 hrs is due to the release of internal stress after heat treatment, and in response gives the fracture surface the characteristic ductile mechanism of dimpling and debonding of powder particles.

4.6.1 Summary of Mechanical Properties

There is a correlation between the decrease in microhardness with the heat treatment temperature. Also, microhardness can be correlated to the coarsening of intermetallic particles. The loss of hardness is not significant after the heat treatments. the hardness values

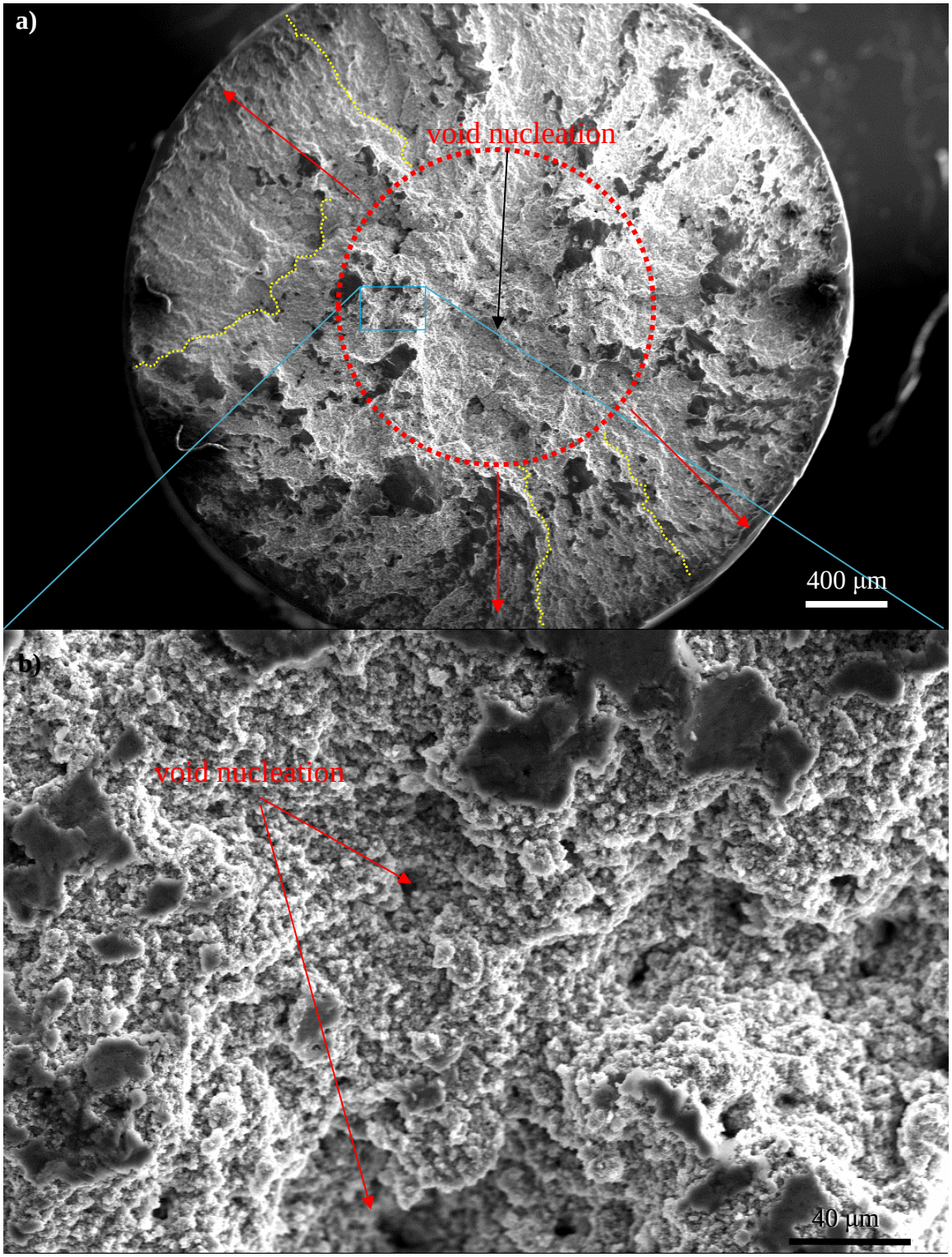

Figure 50. SEM fractography 432 °C - 4.5 hrs sample.

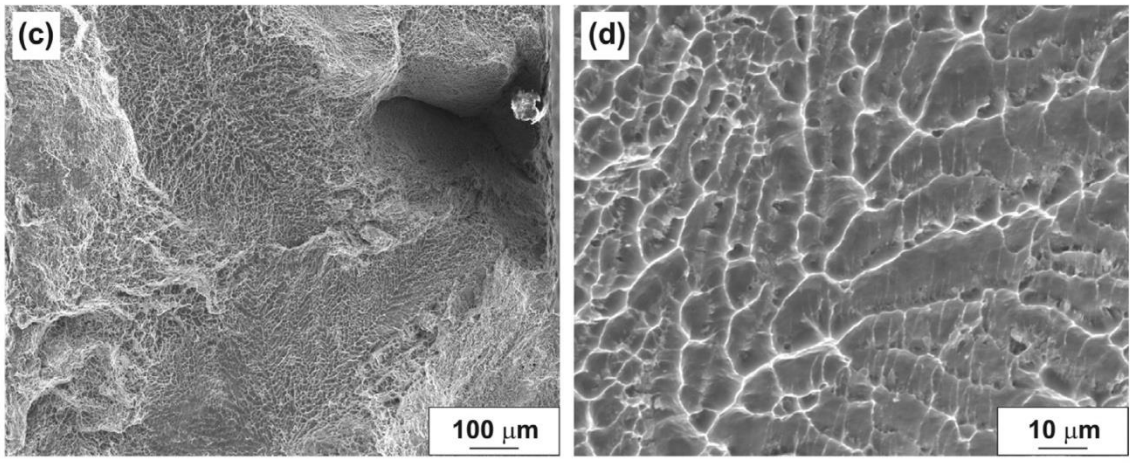

Figure 51. Fracture surface of casted Al-9Ce wt. % [46].

remain high, and the particle coarsening is minimal compared with other conventional nanostructured aluminum alloys.

After the heat treatments, the ultimate tensile strength decreases with the increase in the heat treatment temperature. However, the UTS of the heat-treated samples are still impressive. The gain of ductility is significant without losing the tensile strength excessively. Because of this, Al-8Ce-10Mg can be a potential candidate to replace commonly used structural alloys. Specific strength vs. elongation plot shows that the current alloy has higher specific strength (UTS/density) than the cast iron, Al alloys, Mg alloys, and Ti alloys.

The loss of strength and microhardness have similar values in terms of strength and hardness retention. The following is a list of strength retention and hardness retention values for each heat treatment condition: 350 °C (88 % and 96 %), 400 °C (87% and 87 %), 425 °C (79 % and 87 %), and 432 °C (79 % and 84 %).

After the tensile test, fractography analysis showed brittle fracture behavior of the as-extruded samples. However, ductile fracture surface was observed on the heat-treated sample, specifically at 432 °C - 4.5 hrs condition.

CHAPTER 5 CONCLUSIONS

Various heat treatment conditions were employed to generate distinct microstructures, enabling a comprehensive investigation of their impact on tensile performance. Before the extrusion the alloy powders had a nanoscale intermetallic network. Post-consolidation heat treatments did not significantly affect the phase morphology and distribution. This was expected as $Al_{11}Ce_3$ has been reported to be a thermodynamically stable phase, maintaining its morphology due to the extremely limited solubility of Ce in Al.

There is a trend of increased intermetallic particle size with the increase in the heat treatment temperatures, which was clearly observed on the SEM images. The nanoscaled intermetallic particles assessed with USAXS also demonstrated intermetallic particle coarsening after the heat treatments. During the heat treatment, more pores were generated and observed on the surface microstructure when heat treated at a temperature of 432 °C for 4.5 hrs.

The as-extruded samples have exceptionally high tensile strength compared to conventional Al-based alloys. After the heat treatment, the ductility of the alloy increased markedly without losing strength significantly. A few other specific outcomes are as follows.

- A full consolidation was achieved using warm powder extrusion without a post-consolidation heat treatment.
- The nanoscale microstructure in the gas-atomized powder generated during the rapid cooling resulted in a fine microstructure in the as-extruded samples.
- XRD results showed that the phases present in the as-extruded samples were Al_{α}, $Al_{11}Ce_3$, and $Al_{13}CeMg_6$, whereas the β phase was not present. This agrees with

thermodynamic calculations and since the alloy powder was formed through a rapid solidification during the gas atomization process.

- Based on the thermodynamic calculations, we designed a series of heat treatment experiments to lower the amount of τ phase and increase the amount of Al_{α} and $Al_{11}Ce_3$ phases.
- XRD confirmed that the heat treatment temperatures chosen for this study indeed lowered the amount of τ phase with the increase in the heat treatment temperature, also producing higher amounts of $Al_{11}Ce_3$ and Al_{α} phases.
- After the heat treatment, the limited solubility of Ce in Al and the thermally stable $Al_{11}Ce_3$ phase prevented significant particle coarsening, allowing us to preserve the nanostructured material.
- The measurements of intermetallic particle size and distribution are comparable between the ImageJ analysis of the micrographs and the USAXS results.
- Heat treatments did not have a significant effect in the growth of the intermetallic particles.
- The microhardness decreased with the increase in the particle size. However, the loss of hardness was not significant. Generally, the particle coarsening is minimal, and the hardness remained relatively high under the current heat treatment conditions, compared with other conventional nanostructured aluminum alloys.
- Specific strength vs. elongation plot shows that the current Al alloy is a good candidate for replacing cast Mg alloys, Al alloys, and Fe alloys.

Finally, we successfully consolidated al-8Ce-10Mg powder at an extrusion ratio 25:1 at a working temperature of 300 °C, without additional sintering. A series of heat treatments demonstrated that at the temperature range between 400 °C to 425 °C we can produce a high-strength aluminum alloy with good ductility. In this range the mechanical properties of the material can be tailored depending on the application needs.

Broader Impact

Designing new Al-Ce-based alloys will have an impact on the availability of Al alloys with enhanced corrosion, thermal, and tensile properties. Finding a bulk application for Ce

will impact the economics of the rare earth industry, aiding the production, mining, and securing local supply chains. Al-Ce-Mg alloys possess high strength and the capabilities of substituting Fe alloys when a lighter material is needed, and Ti alloys when a more inexpensive material is requested. Ultimately, research on Al-Ce-Mg based alloys opens new opportunities for developing new processing methods. Combinations of Al-Ce based alloys with other elements could produce alloys with more improved mechanical performances. Insights gained from this research can potentially lead to the production of high-strength aluminum-based alloys that outperform conventional Al-based alloys and some iron and titanium-based alloys, potentially impacting various manufacturing applications.

Future work

Al-Ce alloys have generated interests in basic research and industry applications as a good alternative to replace conventional structural alloys, for its corrosion resistance, light weight, and thermal stability. Powder extruded Al-Ce-Mg alloys are an excellent candidate with nanoscale structure and resistance to coarsening. As an option for high performance, high temperature application material, it is important to evaluate high temperature behavior. Currently, there is limited information about recrystallization temperature of the powder extruded Al-8Ce-Mg wt. % alloy. Therefore, it is important to evaluate high-temperature mechanical performance and the deformation mechanisms. Specifically, tensile and microhardness tests at elevated temperatures are imperative. In addition, the measurement of coefficient of thermal expansion would be useful for high temperature applications. The evaluation of texture would be useful to understand the development of preferred crystal orientation during the extrusion process and post-consolidation heat treatments in relation to the studies of the deformation and recrystallization. Future research on Al-Ce-Mg alloy should explore working on other powder metallurgy manufacturing techniques that can take advantage of the nanoscaled microstructure created during the gas atomization of the alloy powder.

REFERENCES

1. Bauccio, M., *ASM metals reference book*. 1993: ASM international.
2. Polmear, I., *Magnesium alloys and applications.* Materials science and technology, 1994. **10**(1): p. 1-16.
3. Cardarelli, F., *Materials handbook: a concise desktop reference.* 2008.
4. Peters, M., et al., *Titanium alloys for aerospace applications.* Advanced engineering materials, 2003. **5**(6): p. 419-427.
5. Yun, J., et al., *Development of heat-treatable Al-5Mg alloy sheets with the addition of Zn.* Materials Science and Engineering: A, 2019. **744**: p. 21-27.
6. Ye, J., et al., *Beneficial effects of Sc/Zr addition on hypereutectic Al–Ce alloys: Modification of primary phases and precipitation hardening.* Materials Science and Engineering: A, 2022. **835**: p. 142611.
7. Sims, Z.C., et al., *How Cerium and Lanthanum as Coproducts Promote Stable Rare Earth Production and New Alloys.* Journal of Sustainable Metallurgy, 2022. **8**(3): p. 1225-1234.
8. Sims, Z.C., et al., *High performance aluminum–cerium alloys for high-temperature applications.* Materials Horizons, 2017. **4**(6): p. 1070-1078.
9. Weiss, D., *Improved High-Temperature Aluminum Alloys Containing Cerium.* Journal of Materials Engineering and Performance, 2019. **28**(4): p. 1903-1908.
10. Weiss, D., et al., *Casting characteristics of high cerium content aluminum alloys*, in *Light Metals 2017*. 2017, Springer. p. 205-211.
11. Kusoglu, I.M., B. Gökce, and S. Barcikowski, *Research trends in laser powder bed fusion of Al alloys within the last decade.* Additive Manufacturing, 2020. **36**: p. 101489.
12. Vimal, K., M.N. Srinivas, and S. Rajak, *Wire arc additive manufacturing of aluminium alloys: a review.* Materials Today: Proceedings, 2021. **41**: p. 1139-1145.
13. Li, F., et al., *Evaluation and optimization of a hybrid manufacturing process combining wire arc additive manufacturing with milling for the fabrication of stiffened panels.* Applied Sciences, 2017. **7**(12): p. 1233.
14. Hehr, A. and M.J. Dapino, *Interfacial shear strength estimates of NiTi–Al matrix composites fabricated via ultrasonic additive manufacturing.* Composites Part B: Engineering, 2015. **77**: p. 199-208.
15. Ekaputra, C.N., et al., *Eutectic, precipitation-strengthened alloy via laser fusion of blends of Al-7Ce-10Mg (wt.%), Zr, and Sc powders.* Acta Materialia, 2023. **246**: p. 118676.
16. Zhou, L., et al., *Laser powder bed fusion of Al–10 wt% Ce alloys: microstructure and tensile property.* Journal of Materials Science, 2020. **55**(29): p. 14611-14625.
17. Lv, H., et al., *High-performance co-continuous Al-Ce-Mg alloy with in-situ nano-network structure fabricated by laser powder bed fusion.* Additive Manufacturing, 2022. **60**: p. 103218.
18. Martin, A.A., et al., *Enhanced mechanical performance via laser induced nanostructure formation in an additively manufactured lightweight aluminum alloy.* Applied Materials Today, 2021. **22**: p. 100972.

19. Plotkowski, A., et al., *Evaluation of an Al-Ce alloy for laser additive manufacturing.* Acta Materialia, 2017. **126**: p. 507-519.
20. Altıparmak, S.C., et al., *Challenges in additive manufacturing of high-strength aluminium alloys and current developments in hybrid additive manufacturing.* International Journal of Lightweight Materials and Manufacture, 2021. **4**(2): p. 246-261.
21. Fahad, Z., et al., *Additively Manufactured High-Strength Aluminum Alloys: A Review*, in *Recent Advancements in Aluminum Alloys*, R. Dr. Shashanka, Editor. 2023, IntechOpen: Rijeka. p. Ch. 2.
22. Sims, Z.C., et al., *Cerium-based, intermetallic-strengthened aluminum casting alloy: high-volume co-product development.* Jom, 2016. **68**: p. 1940-1947.
23. Zhao, X., et al., *A novel method for improving the microstructure and the properties of Al-Si-Cu alloys prepared using rapid solidification/powder metallurgy.* Materials Today Communications, 2023. **35**: p. 105802.
24. Shamsudin, S., M. Lajis, and Z. Zhong, *Evolutionary in solid state recycling techniques of aluminium: a review.* Procedia CIRP, 2016. **40**: p. 256-261.
25. Shahani, R.A. and T.W. Clyne, *Recrystallization in fibrous and particulate metal matrix composites.* Materials Science and Engineering: A, 1991. **135**: p. 281-285.
26. Belov, N.A., A.A. Aksenov, and D.G. Eskin, *Iron in aluminium alloys: impurity and alloying element*. 2002: CRC Press.
27. Su, M.-N. and B. Young, *Material properties of normal and high strength aluminium alloys at elevated temperatures.* Thin-Walled Structures, 2019. **137**: p. 463-471.
28. Benedetti, M., et al., *Multiaxial fatigue resistance of shot peened high-strength aluminum alloys.* International Journal of Fatigue, 2014. **61**: p. 271-282.
29. Maximov, J., et al., *Effect of slide burnishing basic parameters on fatigue performance of 2024-T3 high-strength aluminium alloy.* Fatigue & Fracture of Engineering Materials & Structures, 2017. **40**(11): p. 1893-1904.
30. Børvik, T., M.J. Forrestal, and T.L. Warren, *Perforation of 5083-H116 Aluminum Armor Plates with Ogive-Nose Rods and 7.62 mm APM2 Bullets.* Experimental Mechanics, 2010. **50**(7): p. 969-978.
31. *2022 Final List of Critical Minerals*, D.O.T. INTERIOR, Editor. 2022, Federal Register. p. 10381-10382.
32. Fishman, T., et al., *Implications of Emerging Vehicle Technologies on Rare Earth Supply and Demand in the United States.* Resources, 2018. **7**(1): p. 9.
33. Gschneidner Jr, K. and M.E. Verkade, *Selected cerium phase diagrams*. 1974, Iowa State Univ. of Science and Technology.
34. Okamoto, H., *Al-Ce (aluminum-cerium).* Journal of phase equilibria, 1998. **19**(4): p. 395.
35. Okamoto, H., *Al-Ce (Aluminum-Cerium).* Journal of Phase Equilibria and Diffusion, 2011. **32**(4): p. 392-393.
36. Umarova, T. *Influence of microalloying (including rare-earth metals) on the phase composition and properties of aluminum alloys*. in *Materials Science Forum*. 2017. Trans Tech Publ.

37. Weiss, D., et al., *Casting Characteristics of High Cerium Content Aluminum Alloys*. 2016, Lawrence Livermore National Lab.(LLNL), Livermore, CA (United States).
38. Stromme, E.T., et al., *Ageless aluminum-cerium-based alloys in high-volume die casting for improved energy efficiency.* Jom, 2018. **70**(6): p. 866-871.
39. Ryen, Ø., et al., *Strengthening mechanisms in solid solution aluminum alloys.* Metallurgical and Materials Transactions A, 2006. **37**: p. 1999-2006.
40. Cheng, J., et al., *Experiment and non-local crystal plasticity finite element study of nanoindentation on Al-8Ce-10Mg alloy.* International Journal of Solids and Structures, 2021. **233**: p. 111233.
41. Rakhmonov, J.U., D. Weiss, and D.C. Dunand, *Solidification microstructure, aging evolution and creep resistance of laser powder-bed fused Al-7Ce-8Mg (wt%).* Additive Manufacturing, 2022. **55**: p. 102862.
42. Lu, Z. and L. Zhang, *Thermal stability and crystal structure of high-temperature compound Al13CeMg6.* Intermetallics, 2017. **88**: p. 73-76.
43. Ekaputra, C.N., et al., *Eutectic, Precipitation-Strengthened Alloy Via Laser Fusion of Blends Al-7Ce-10mg (Wt.%) and Zr+ Sc Elemental or Prealloyed Powders.* Available at SSRN 4128728.
44. Lane, R.J., et al., *Developing an experimental-computational framework to investigate the deformation mechanisms and mechanical properties of Al-8Ce-10Mg alloys at micro and macroscales.* Materials Today Communications, 2021. **28**: p. 102674.
45. Murarka, S. and R. Agarwala, *DIFFUSION OF RARE EARTH ELEMENTS IN ALUMINUM*. 1968, Bhabha Atomic Research Centre, Bombay (India).
46. Rogachev, S.O., et al., *High strength al–la, al–ce, and al–ni eutectic aluminum alloys obtained by high-pressure torsion.* Materials, 2021. **14**(21): p. 6404.
47. Pan, H., et al., *Size-dependent microstructure evolution and formation mechanisms during the gas atomization process of FGH4113A Ni-based superalloy powder*. Vacuum, 2023. **209**: p. 111751.
48. Weiss, D., et al. *Casting characteristics of high cerium content aluminum alloys*. in *Light Metals 2017*. 2017. Springer.
49. Vázquez, M., *Effects of processing on the properties of aluminum-cerium-based alloys*. 2020.
50. Henderson, H.B., et al. *Ternary interactions and implications for third element alloying potency in Al–Ce-based alloys*. in *Light Metals 2020*. 2020. Springer.
51. Moore, E.E., et al., *Thermodynamic Modeling of the Al-Ce-Cu-Mg-Si System and Its Application to Aluminum-Cerium Alloy Design.* Journal of Phase Equilibria and Diffusion, 2020. **41**(6): p. 764-783.
52. Didier, C., et al., *Phase evolution and intermittent disorder in electrochemically lithiated graphite determined using in operando neutron diffraction.* Chemistry of Materials, 2020. **32**(6): p. 2518-2531.
53. Ilavsky, J. and P. Jemian, *Irena: Tool Suite for Modeling and Analysis of Small Angle Scattering.* Journal of Applied Crystallography - J APPL CRYST, 2009. **42**: p. 347-353.

54. Zhang, F., et al., *Glassy Carbon as an Absolute Intensity Calibration Standard for Small-Angle Scattering.* Metallurgical and Materials Transactions A, 2009. **41**: p. 1151-1158.
55. Lixin, F., et al., *The Absolute Calibration of a Small-Angle Scattering Instrument with a Laboratory X-ray Source.* Journal of Physics: Conference Series, 2010. **247**(1): p. 012005.
56. ASTM, *E8/E8M-22 standard test methods for tension testing of metallic materials, Annu.* 2022.
57. Weiss, D., *Thermal Treatment of Al-Mg-Ce Alloys.* Transaction of the American Foundry Society, 2018: p. 18-101.
58. Sisco, K., et al., *Microstructure and properties of additively manufactured Al–Ce–Mg alloys.* Scientific Reports, 2021. **11**(1): p. 6953.
59. Murray, J.L., *The Al−Mg (Aluminum−Magnesium) system.* Journal of Phase Equilibria, 1982. **3**: p. 60-74.
60. Smeltzer, W.W., *Oxidation of An Aluminum-3 Per Cent Magnesium Alloy in the Temperature Range 200°–550°C.* Journal of The Electrochemical Society, 1958. **105**(2): p. 67.
61. Hidvegi, E. and E. Kovács-Csetényi, *Study of the loss of magnesium in an Al Mg Si alloy.* Materials Science and Engineering, 1977. **27**(1): p. 39-43.
62. Cochran, C.N. and W.C. Sleppy, *Oxidation of High-Purity Aluminum and 5052 Aluminum-Magnesium Alloy at Elevated Temperatures.* Journal of The Electrochemical Society, 1961. **108**(4): p. 322.
63. Kovács, I., J. Lendvai, and T. Ungár, *Investigation of Mg loss during heat treatments in an Al Mg Si alloy.* Materials Science and Engineering, 1975. **21**: p. 169-175.
64. Henderson, H.B., et al., *Enhanced thermal coarsening resistance in a nanostructured aluminum-cerium alloy produced by additive manufacturing.* Materials & Design, 2021. **209**: p. 109988.
65. Furukawa, M., et al., *Microhardness measurements and the Hall-Petch relationship in an Al Mg alloy with submicrometer grain size.* Acta Materialia, 1996. **44**(11): p. 4619-4629.
66. Lewandowska, M. and K.J. Kurzydłowski, *Thermal stability of a nanostructured aluminium alloy.* Materials Characterization, 2005. **55**(4): p. 395-401.
67. ASTM, *A48/A48M-22 Standard Specification for Gray Iron Castings*. 2022.
68. ASTM, *A595/A595M-22 Standard specification for steel tubes, low-carbon or high-strength low-alloy, tapered for structural use*. 2022. p. 5.
69. ASTM, *B80-23 Standard Specification for Magnesium-Alloy Sand Castings*. 2023. p. 12.
70. ASTM, *B265-20a Standard Specification for Titanium and Titanium Alloy Strip, Sheet, and Plate*. 2020.
71. Committee, A.I.H., *Metals Handbook Vol 2: Properties and Selection: Nonferrous Alloys and Special-Purpose Materials.* ASM Int, 1990. **3**(5).
72. Nath, J., *Engineering of Malleable Iron Castings.* 2022.

VITA

Mairym Vázquez was raised in Yauco, Puerto Rico. For high school she graduated from CROEM. This is the top specialized school, with a focus in sciences and math, where only the top students of Puerto Rico are selected to study. She graduated Magna Cum Laude from Caribbean University in Bayamón, Puerto Rico, with a bachelor in science of engineering (B.S.E.) degree in Industrial Engineering. Later, she earned a master in science (M.S.) degree in Materials Science & Engineering from the University of Puerto Rico at Mayagüez. She joined the Oak Ridge National laboratory as a Post-Bachelor's Research Associate through ORAU/ORISE. There she worked with at the Deposition Science and Technology Group within the Materials Science & Technology Division (MSDT) with Dr. Orlando Rios. Later, Mairym applied for graduate school at The University of Tennessee, where she will earn a Ph.D. in Materials Science & Engineering.